Study of Rheological Behaviour of Spherocylindrical Particle Suspension via CFD-DEM

Formulation of Stress-Closure for Industrial Fluidized Bed Simulation

Master's Thesis
Junaid Mehmood

Faculty of Applied Sciences
Chemical Engineering

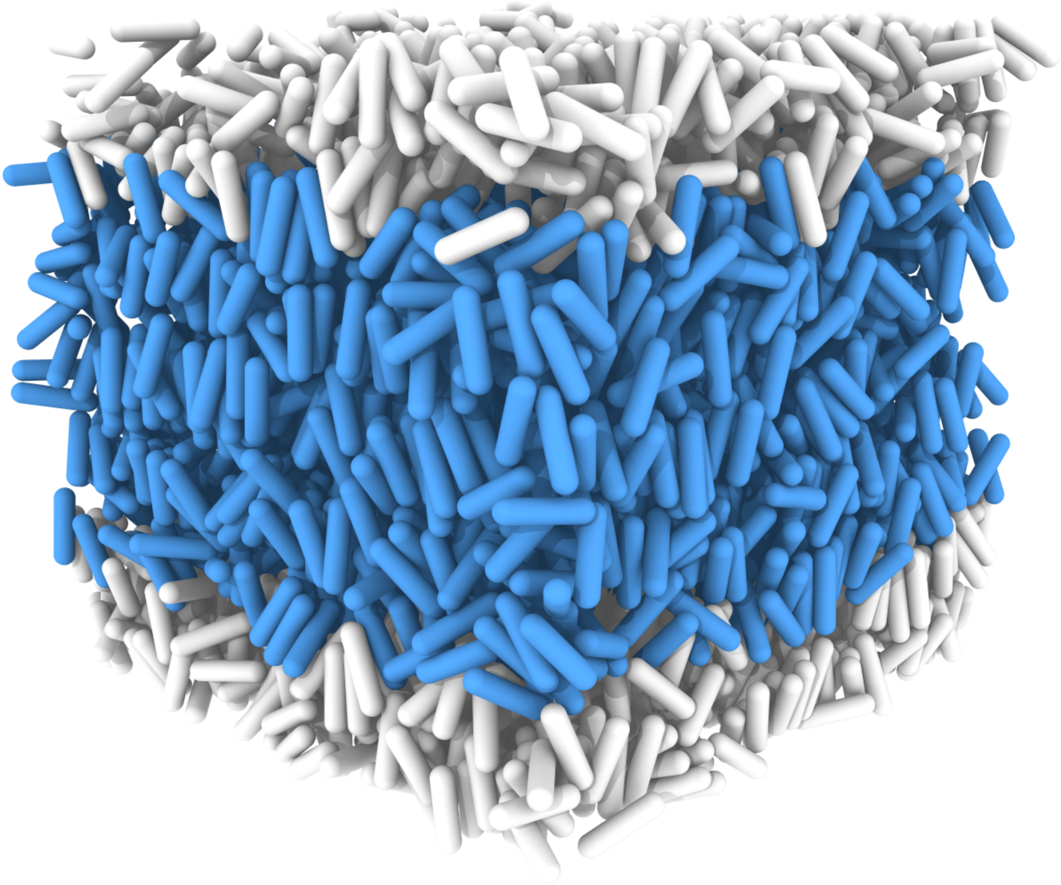

Delft
University of
Technology

Challenge the future

Study of Rheological Behaviour of Spherocylindrical Particle Suspension via CFD-DEM

Formulation of Stress-Closure for Industrial Fluidized Bed Simulation

Master's Thesis
Junaid Mehmood
March 2018

Faculty of Applied Sciences
Chemical Engineering
Department: Process & Energy, Faculty 3mE
Section: Intensified reaction & separation systems

Graduation Committee
prof. dr. ir. J. Ruud van Ommen
dr. H.B. Eral
dr. ir. Johan T. Padding

Abstract

While colloidal suspensions of non-spherical particles have been studied relatively extensively, granular suspensions of non-spherical particles are rarely studied. The rheological behaviour of elongated granular particles is therefore not well known. This thesis deals with suspensions of rod-like particles of aspect ratio 4 subjected to shear flow in a low-density, highly viscous Newtonian fluid. CFD-DEM simulations for a periodic shear box have been performed for a pre-estimated range of shear rates and volume fractions. Dependence of rheological properties like shear stresses, relative viscosity, granular temperature, pressure and normal stress differences on the shear rate and volume fraction have been studied. These granular rods show shear thickening behaviour. The spherocylindrical particle suspensions experience less collisional stresses than spherical particles due to preferred particle alignment in the shear direction. Herschel and Bulkley [1] model is used to fit the collisional stress data. Two different regimes have been identified for granular suspension based on the flow index. Interestingly, a relatively large range of shear rates and associated stress can be expressed in the form of a simple equation based on Broughton and Squires [2] model. This stress closure will further be used in more coarse grid models like MP-PIC which can simulate an industrial fluidized bed reactors of non-spherical particles.

Contents

1

Introduction

Dispersions (systems that are a mixture of two or more phases i.e. gas/liquid/solid) are present everywhere in nature (milk, blood, clouds, rivers, sandstorms, landslides) and industry (cosmetics, paints, detergents, oil mineral industries). ”Suspension” type dispersions particularly, monodispersed solids in a continuous fluid phase (liquid or gas), have critical importance for the chemical industry. Better understanding of fundamental physics behind particle suspensions is necessary to control industrial processes like gas-solid fluidization and fluid catalytic cracking.

Gas-solid fluidization is industrially recognized process for many decades because of its advantages like mixing, uniform temperature distribution and good gas-solid contact for heat and mass transfer [3]. These advantages make fluidized bed reactors a favourable choice for many applications ranging from combustion & gasification to drying & powder coating [4]. After 2001, due to rising oil prices interest in biomass gasification has increased to reduce the dependence on fossil fuels [5]. Biomass gasification produces syn-gas ((a mixture of CO and H_2) which can be utilized in manufacturing fertilizer or upgraded to higher hydrocarbons through Fischer- Tropsch reaction. Bubbling fluidized bed (BFB) and Circulating fluidized bed (CFB) reactors can be used for biomass gasification [4]. These reactors use raw material that are pre-dominantly non-spherical in nature. It has already been established that particle size and shape affects the fluidization behaviour such as pressure drop and minimum fluidization velocity [6–8]. Biomass, mainly wood pellets and rice husk, possess an elongated shape and show poor agreement with spherical particle models. This require the development of a specialized models to better understand their distinct shape effects to devise the optimum design of biomass gasifiers.

A detailed computer simulation of an industrial sized fluidization reactor can require very high computational cost. During past few years, several simulations techniques such as multiphase particle in cell method (MP-PIC) [9] have been developed to perform industrial scale simulations. Instead of calculating the computationally intensive particle interactions, a stress closure can be incorporated in the model. Particle stresses are usually calculated from the basic system parameters such as volume fraction, shear rate and system pressure. Stress closures for spherical particles are available in literature [10]. These stress closures are based on the kinetic theory of granular fluids (KTGF). KTGF is based on the basic assumption that all particles are spherical and collisions between particles are of binary nature. For elongated particles, even these assumptions break down especially at higher solid volume fraction.

The purpose of this work is twofold: first, to develop an understanding of the rheological behaviour of spherocylindrical particles and secondly, to obtain a collisional stress closure for these particles to be used in industrial fluidized bed simulation. In this work, a numerical model is used to describe the behaviour of particle-particle interactions. Discrete element method (DEM) and computational fluid dynamics (CFD) are coupled to solve particle movement and gas flow through the control box. DEM has been modified to incorporate the spherocylindrical particle. Equation given by Hölzer and Sommerfeld [11] is used to calculate the drag force on the particles.

2

Literature review

Fluids experience several kinds of deformation under the influence of forces. To describe their behaviour, Newton postulated his famous law of viscosity that related the shear stress to the strain ($\sigma = \eta_o \dot{\gamma}$). However, its applicability was limited to fluids that exhibit close to ideal behaviour. To explain the non-Newtonian aspect of fluid behaviour several models have been proposed by Einstein [12], Bingham [13] and Herschel and Bulkley [1]. The term "Rheology" was coined in 1929, to establish a separate field to explicitly study these phenomena.

Rheology of particles that are suspended in fluid undergoes two types of interactions, particle-particle & particle-fluid. Based on these interactions granular systems can be classified into two types.

1. Granular flows: If particles are much denser than fluid, particle-fluid interactions can be ignored and only particle-particle interactions are responsible for the momentum transfer [14]. This is usually the case for granular flows.
2. Granular suspension: If fluid density is very close to solid density particle-fluid interactions become important which is usually the case of granular suspensions.

Experiments have not been proven to be very useful to study particle suspensions [15]. Rheometer is used to study the rheology of suspensions. It only offers the measurement of shear stresses and total pressure in the system. This is a great barrier to improve our understanding for the rheology of particle suspensions. On the other hand, in past 30 years, discrete element method (DEM) has been developed and used to study granular systems in depth. DEM[1] was developed by Stark and Cundall [16]. This method offers many advantages over the experimentation like measurements of volume fraction, complete stress tensor and residual kinetic energy of the system. After its birth, this method has been used extensively for the number of granular suspensions behaviours like shear flow, hopper flow and fluidized bed [15, 17–19]. DEM is a useful tool to study granular flows and if coupled with computational fluid dynamics (CFD) this framework can be extended to study granular suspensions.

Present work is based on CFD-DEM coupled simulation of spherocylindrical particles of aspect ratio 4. It is important to take a look at past studies for granular systems to find out which theories or system are closely related to present work. In the following section, each of the these theories are discussed with main focus on the developed particle stresses.

2.1. Granular flows

Granular material is formed by discrete particles. These materials behave like solid if forces acting from all sides are equal. There exists two types of deformation in granular material i.e. plastic deformation (particle-particle bonds break down) and elastic deformation (frictional bonds break down but material return to original state). For the particular amount of stresses, a material can deform plastically and behave like a fluid. Granular flows exist in nature in form of sand and landslides. These flows share

---

[1] Detailed discussion in chapter 3

similarity with gases because momentum transfer between particles is solely due to particle-particle collisions.

For granular flows, velocity of each particle can be decomposed in to the sum of the mean velocity of flow and random fluctuation of velocity from the mean bulk value. In 1978, Ogawa [20] introduced the concept of granular temperature to characterize this velocity fluctuation in granular media. The granular kinetic theory was developed at that time to define the phenomenon of dilute and dense granular flow based on the kinetic theory of dense gases by Chapman and Cowling [21]. Jenkins and Savage [22] extended the kinetic gas theory but were only able to predict the collisional stresses in the granular flow. Lun et al. [23] improved on the theory presented by Jenkins and Savage by using perturbed Maxwellian distribution velocity function. Their theory is the most detailed and comprehensive work to date which predicts not only collisions stresses but also kinetic stresses produced due to particle motion. According to their theory, shear stress for smooth, hard inelastic spheres in the plane shear flow is as follows:

$$\sigma_{zx} = \sigma_{xz} = -\frac{5}{96} J(\phi, e) \rho_p (\pi T)^{0.5} d_p \dot{\gamma} \tag{2.1}$$

Granular temperature (T) can be defined as follows:

$$T = \frac{5\pi}{4608} \frac{J(\phi, e)}{\alpha\,(1-\alpha)\,\phi^2 g_o} d_p^2 \dot{\gamma}^2 \tag{2.2}$$

and $J(\phi, e)$ is of the following form:

$$J(\phi, e) = \frac{1}{\alpha\,(2-\alpha)\,g_o}\left(1 + \frac{8}{5}\alpha\phi g_0\right)\left[1 + \frac{8}{5}\alpha\phi g_0\,(3\alpha - 2)\right] + \frac{768}{25\pi}\alpha\phi^2 g_0 \tag{2.3}$$

α is a function of coefficient of restitution while g_o is radial distribution function for spherical binary contact which only depends on the volume fraction (ϕ) [24].

$$\alpha = \frac{1}{2}\,(1 + e) \tag{2.4}$$

$$g_0 = \frac{1}{1-\phi} + \frac{3\phi}{2\,(1-\phi)^2} + \frac{\phi^2}{2\,(1-\phi)^3} \tag{2.5}$$

Campbell and Gong [17] performed the 2-D numerical simulations which were in good agreement with the predictions from Lun et al. Jenkins and Richman [25] performed the same analysis also for the disks and improved on the theory by including dissipation induced second moment stress tensor.

Goldshtein and Shapiro [26] extended the granular kinetic theory for the rough inelastic spherical particle. The presence of frictional forces results in energy loss due to heat and also results in conversion between translational and rotational energy. Jenkins and Zhang [27] showed that energy loss due to frictional forces can be described by use of the effective coefficient of restitution which is a function of normal coefficient of restitution and frictional coefficient.

$$e_{eff} = e - \frac{\pi}{2}\mu + \frac{9}{2}\mu^2 \tag{2.6}$$

For dense granular flows, the assumption of instantaneous collisions does not hold true and long lasting collisions becomes dominant [28]. Kinetic theory needs to be modified to incorporate this phenomenon. Jenkins [29] implemented a length scale in the expression of the rate of collision dissipation for the dense flows of frictionless, inelastic disks. Berzi et al. [30] considered the role of particle contact stiffness for the frictional component of the stress tensor. Campbell [28, 31, 32] observed that in dense granular flows stresses are generated by particle elasticity. He distinguished two dense granular flow regime. In the *elastic inertial regime,* stresses increase linearly with shear rate and scale with the elasticity while in *elastic quasi-static regime* although stresses scale with the elasticity but they have no dependence on the shear rate.

Granular kinetic theory (GKT) is not the only theory in literature to describe granular flows. $\mu_{eff}(\mathrm{I})$ rheology [33, 34] is comparatively new field than GKT which was developed in mid 2000's. Constitutive equation which describes the conservation laws of granular flows can be defined by *Inertial Number,*

$I = \dot{\gamma}D/\sqrt{\frac{P}{\rho_p}}$. Volume fraction and effective friction (μ_{eff}) which is ratio of shear stress to the pressure are functions of I. These functions have been determined by simulations [35–37] as wells as by experiments[38, 39]. Pressure is an important parameter for this theory which is usually an external influencing factor. For this study, pressure is an internal property of the system and directly depends on the normal stresses. For this reason $\mu_{eff}(\mathrm{I})$ rheology has not been explored further. Detailed discussion is in section 5.4.

Most of the studies discussed above only deals with the circular disks or spheres. Recently researchers have performed experiments [40, 41] and simulations with the different particle shapes. Simulations performed by Pena et al. [42] for polygonal disks and Cleary and Sawley [43] for different shapes of disks shows that particle shape has strong effects on the granular temperature and volume fraction in the core of the flow, both of these values are smaller compared to spherical particles. Moreover, particles with non-regular shape (higher aspect ratio or more angular geometry) are hard to shear due to interlocking of the particles. One of the main attributes of non-spherical particles is that the elongated particles have preferred alignment towards main flow stream as shown by Pena et al. [42], Reddy et al. [44, 45] and Campbell [46]. Campbell [46] performed 3D simulations for ellipsoid particles. He observed that friction forces have a strong influence on the stresses for elongated particles than for spheres. For smooth ellipsoid particles, smaller stresses were observed when compared to the spheres. While large surface friction can lead to particle rotation which can block the flow so stress values were higher. Guo et al. [47] performed 3D DEM simulations for particles with different aspect ratio. Three different regimes (dilute, dense and intermediate) discussed by Campbell and Gong [17] were observed also for elongated particles. Stress values are smaller compared to the spherical particles which were attributed to the smooth surface and alignment of the elongated particles. Nagy et al. [48] have also performed a 3D simulation with the spherocylindrical particles up-to aspect ratio of 2.5. In their study, they have demonstrated that $\mu_{eff}(\mathrm{I})$ rheology can be extended to non-spherical particles.

2.2. Granular suspensions

Rheology of liquid-solid suspension not only depends on the particle-particle interactions but also on the particle-fluid interaction. Fluid properties like density and viscosity play a significant role. Most prominent work so far on the rheology of the granular suspension was performed by Bagnold [49] which led to the birth of Bagnold theory. Bagnold performed experiments with spherical particles made of wax suspended in Newtonian fluids (water and water-glycerine mixture). He observed two limiting type of behaviour. In *micro-viscous region*, suspension stresses both normal and shear have a linear relationship with the shear rate and also depend on the fluid viscosity. In the *grain inertia region* stresses are proportional to the square of the shear rate with a minor effect of fluid properties. He distinguished both of these regimes with a so-called *Bagnold number* which is the ratio of grain collisional stresses to viscous fluid stresses. For $Ba < 40$ system is in micro-viscous regime while for $Ba > 450$ it is in grain inertia regime.

$$Ba = \frac{\rho_p d_p^2 \lambda^{0.5} \dot{\gamma}}{\eta_f} \tag{2.7}$$

λ is the linear concentration based on the volume fraction (ϕ).

$$\lambda = \frac{1}{\left[\left(\frac{\phi}{\phi_m}\right)^{\frac{1}{3}} - 1\right]} \tag{2.8}$$

Many authors have used Bagnold approach to form a constitutive relationship between shear rate and stress [50–52]. All of these studies have shown the similar behaviour. Recently Hunt et al. [53] revisited the Bagnold experiment and they have shown that in the *grain inertia region* stress do not vary quadricitally to the shear rate but shear stresses depend on the shear rate to the 1.5 power. Results in present work have been compared with Bagnold theory.

It is also very common to study suspension rheology in terms of apparent viscosity (η_a) which is equal to ($\frac{\sigma}{\dot{\gamma}}$). For Newtonian fluid $\eta_a = \eta_o$, while for non-Newtonian fluids it is dependent on shear rate. For suspensions η_a is the ratio of suspension viscosity and fluid viscosity. Rutgers [54, 55] and Thomas [56] summarized early research separately. Most of the summarized research was related to relationship between apparent viscosity (η_a) and volume fraction(ϕ). Both have distinguished three regimes for $\eta_a(\phi)$ as follows,

1. Dilute regime ($\phi < 0.01$ (Rutgers [54]), $\phi < 0.02$ (Thomas [56]))
2. Semi-dilute regime ($\phi < 0.25$)
3. Concentrated or dense regime ($\phi > 0.25$)

For dilute regime, $\eta_a(\phi)$ is linear and rheology is Newtonian. For semi dilute regime, η_a shows higher order dependence to ϕ while behaviour remains Newtonian. For concentrated regime, η_a increases rapidly and rheological behaviour becomes non-Newtonian. Einstein [57] studied the suspension in the dilute limit and derived a η_a relationship for an isolated sphere which is given as:

$$\eta_a = 1 + B\phi \tag{2.9}$$

B is referred as "Einstein coefficient" and its value is 2.5. There have been lots of efforts to determine right value for *B* for dilute regime but this value changes significantly from 1.5 to 5 depending upon the experiments [58–60].

For semi-dilute regime, most of the work has been done to find the higher order coefficients for the following equation:

$$\eta_a = 1 + B\phi + B_1\phi^2 + ... \tag{2.10}$$

while $B = 2.5$ and $7.35 \leq B_1 \leq 14.1$ derived by particle particle interactions [61–63].

Equation 2.10 predicts viscosity value even for the case where solid volume fraction approaches to 1. This is physically not possible because for spheres maximum possible packing (ϕ_m) is 0.74. For this volume fraction value, viscosity must be infinite because there is no space for the particles to move. Due to this, polynomial expressions for $\eta_a(\phi)$ cannot fit the experimental data for the concentrated regime and required a modification in terms of ϕ_m. Krieger and Dougherty [64] obtained the following correlation for concentrated regime,

$$\eta_a = \left(1 - \frac{\phi}{\phi_m}\right)^{-B\phi_m} \tag{2.11}$$

B is Einstein constant. Above expression has been used extensively throughout the years to fit the experimental data for concentrated regime [59, 60].

All of above relations shows power law dependence on the volume fraction. Richardson [65] first proposed a very simple power law in terms of volume fraction for apparent viscosity.

$$\eta_a = exp(k\phi) \tag{2.12}$$

where k is a constant. Broughton and Squires [2] improved on the Richardson [65] relationship by including a system depending parameter A.

$$ln(\eta_a) = A + k\phi \tag{2.13}$$

Equation 2.13 can be used for semi-dilute and concentrated regime. This equation has been modified for the present study in terms of maximum volume fraction to fit the simulation data.

Rutgers [54, 55] reported non-Newtonian behaviour for 75% of reviewed experiments. Stickel and Powell [66] have summarized research on non-Newtonian behaviour for concentrated regime. They considered Brownian motion and inertia to be the governing phenomenon for Newtonian or non-Newtonian behaviour. Peclet (Pe) and Reynolds (Re) number are used to quantify the brownian and inertial effects respectively. Stickel and Powell [66] reported that for $Pe \geq 10^3$ viscosity becomes independent of Peclet number. For $Re \geq 10^{-3}$ inertial effects plays a significant role in suspension rheology. They have shown that system rheological behaviour depends significantly on the Peclet and Reynolds number.

There is a very limited research available on the non-spherical particle suspensions in the literature. Jeffery [67] presented an analytical solution for the motion of ellipsoidal particles in the shear flow. Jeffery determines Einstein coefficient (B) by integrating the work that is done by the fluid to rotate the particle. Jeffery work has been validated numerically [68, 69] and experimentally [70, 71]. Brenner [72] noted the equivalence between spherical particles and particles which have the axis of rotational symmetry in terms of aspect ratio. Doi and Edwards [73] defines three regimes for particles with axis of rotational symmetry based on particle number (N), particle length (L_p) and particle diameter(d_p) in unit volume.

1. Dilute regime ($N << \frac{1}{L_p^3}$)
2. Semi dilute regime ($\frac{1}{L_p^3} < N < \frac{1}{L_p^2 d_p}$)
3. Concentrated or dense regime ($N > \frac{1}{L_p^2 d_p}$)

For spheroid particles with aspect ratio of 10 regime boundaries in term of volume fraction are 0.005 and 0.05. Anczurow [74] confirmed the Jeffrey approach to calculate Einstein coefficient (B) for dilute regime via experiment. Stover et al. [75] performed experiments to study semi dilute regime. Most of the time particles rotated around the major axis and very less time in the shear direction. Jeffrey equation to calculate B was modified with anisotropic weak rotary diffusivity, which provided very good fit for the semi dilute regime.

For concentrated regime, studied have shown that $\eta_a(\phi)$ is only linear for low concentration so Einstein equation (equation 2.9) is not valid [60, 76, 77]. $\eta_a(\phi)$ is also dependent on the aspect ratio of the particles. Pabst et al. [60] fit their experimental data by using equation 2.11. This fit provides higher value for the Einstein coefficient (B) than Jeffrey's. This is because Jeffrey equation of particle does not consider collisional interactions which are very dominant for higher volume fractions.

Mueller et al. [78] studied the suspension of prolate and oblate particles. They observed shear-thinning behaviour which is according to the Stickel and Powell [66] discussion. Herschel and Bulkley [1] equation was used to fit the experimental data. Happel [58] defined the relationship between the rate of work that is required to shear the specific volume of fluid and apparent viscosity. This relationship was used by Mueller et al. [78] to find the apparent viscosity of the suspension. The final equation is as follows:

$$\eta_a = 1 + \frac{\dot{W}_p}{\eta_o \dot{\gamma}^2 V_p}\phi \tag{2.14}$$

Most of the work discussed in this literature review only deals with spherical particle granular systems. Even though there is some literature available for non-spherical particles, it only deals with rheological behaviour of friction-less, elastic particle in the granular flow domain. There is no literature available on the rheological study of non-spherical granular suspension via simulations. Present study focuses on exploring this topic. Not only rheological properties of non-spherical particles have been investigated but theories discussed in above sections have also been used to understand this behaviour. Finally Broughton and Squires [2] model has been used to propose a stress closure which can further be used for industrial fluidized bed simulations.

3

Model description

CFD-DEM is used to perform the simulation in this study. Particle-particle and particle-wall interaction are resolved by Discrete Element Method (DEM) based on LIGGGHTS® [79]. Meanwhile, the Computational Fluid Dynamics (CFD) code based on openFOAM®[80] and CFDEM®coupling [81] solves the gas flow in an Eulerian way and couples this flow to the particles. A schematic overview of this model structure is shown in Figure 3.1. Gas flow is solved on a grid which is larger than the particle size. A description for both of these methods has been provided in the following section.

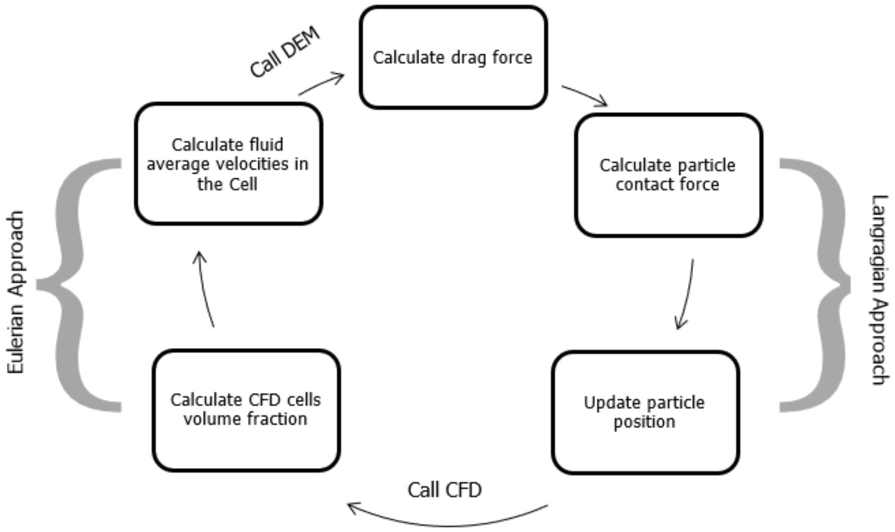

Figure 3.1: Schematic overview of the CFD-DEM model structure.

3.1. Discrete element method

DEM is based on molecular dynamics (MD) method which was developed by Alder and Wainwright [82] in 1950s. DEM can further be divided into two modelling technique either as ”hard-spheres” or as ”soft-spheres” based on particle-particle interaction mechanism.

In hard sphere model, particle motion is determined by binary collisions. In the simulation, particle collisions are solved one by one according to the order in which events takes place. Campbell and Brennen [83] used this model for the first time to study granular media. Goldschmidt et al. [84] have used hard sphere approach to study dense gas fluidized bed in connection with kinetic theory of granular media. Most recently Zhou et al. [85] have incorporated the effect of gas turbulence in this model. Hard sphere model is limited when it comes to dense systems or multiple contacts. It is best suited for simple systems where particle number density is not very high. In more complex systems, the soft-sphere model is the best option and it is also being used in this study.

3.1.1. Soft-sphere model

In complex situations, particles can interact for short and long time depending on the forces. Particle movement can be tracked by solving Newton equation of motion. Stark and Cundall [16] developed the soft-sphere approach for granular dynamics simulations. In this approach particles are treated as hollow spheres which can overlap with each other and contact forces are calculated by a contact-force scheme which depends on deformation history of the particle. This model is a time-driven model where time step to calculate the particle collision must be chosen very carefully. This model can be used to study a number of systems such as gas-fluidized bed [86], cohesive particulate systems [87] and gas-particle heat transfer [88]. Recently, Zhu et al. [89] discussed the theoretical developments in this model.

In the following, the soft-sphere approach has been discussed extensively to give the reader an overview of how simulation via this approach proceeds.

Equation of motion

Particle motion of a single spherical particle of mass M_i and coordinate r_i can be described by Newton law of motion as follows:

$$M_i \frac{\mathrm{d}^2 \vec{r}_i}{\mathrm{d}t^2} = \vec{F}_{c,i} + \vec{F}_{ext,i} \tag{3.1}$$

Three forces acting on the particle are:

1. Total contact force $(\vec{F_c}, i)$ which is the sum of all contact forces exerted by other particles on particle *i*. These forces are the sum of tangential and normal components.

$$\vec{F}_{c,i} = \sum_{j \in \textit{neighbour list}} \left(\vec{F}_{ij,n} + \vec{F}_{ij,t} \right) \tag{3.2}$$

2. External forces $(\vec{F}_{ext,i})$ which are sum of external forces like gravity($M_i g$), fluid forces on the particle and forces due to pressure gradient.

Rotational motion of the particle is calculated by:

$$\vec{I}_i^m \frac{\mathrm{d}\vec{\omega}_i}{\mathrm{d}t} = \vec{\tau}_i \tag{3.3}$$

Equation 3.1 and 3.3 are basic two equation to fully describe motion of the particles.

Contact force

There are number of models in the literature to calculate contact force between particles. One which is mostly used and simplest one is described by Stark and Cundall [16], where normal contact force between particle *i* and *j* is calculated by linear spring model (Figure 3.2) as follows:

$$\vec{F}_{ij,n} = -k_n |\delta_{ij,n}| \vec{n}_{ij} + \zeta_n \vec{v}_{ij,n} \tag{3.4}$$

$\vec{v}_{ij,n}$ is the relative velocity at point of contact between sphere i and j. $\delta_{ij,n}$ is the normal overlap calculated by following formula:

$$\delta_{ij,n} = (R_j + R_i) - |r_j - r_i| \tag{3.5}$$

Coulomb friction law is used to calculate tangential contact force via a split function.

$$\vec{F}_{ij,t} = \begin{cases} -k_t |\delta_{ij,t}| \vec{t}_{ij} + \zeta_t \vec{v}_{ij,t} & \text{for } |\vec{F}_{ij,t}| \leq \mu |\vec{F}_{ij,n}| \\ -\mu |\vec{F}_{ij,n}| \vec{t}_{ij} & \text{for } |\vec{F}_{ij,t}| > \mu |\vec{F}_{ij,n}| \end{cases} \tag{3.6}$$

Tangential displacement $(\delta_{ij,t})$ is calculated by integrating tangential velocity with respect to time for contact duration.

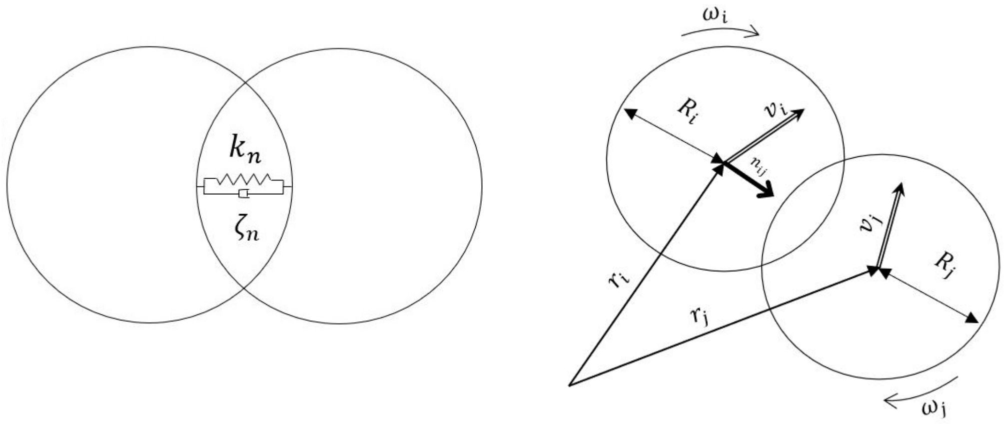

(a) Representation of spring model for sphere contact.

(b) Parameters used for soft-sphere model.

Figure 3.2: Sphere Contact Model.

Contact Parameters ζ_n, ζ_t depends on coefficient of restitution (e_n & e_t) and spring constants (k_n & k_t). Usually for simulations e_t and e_n are assumed to be equal. Although spring constants depend on material properties like young modulus and poison ratio, their values strongly influence the contact time so needs to be chosen really carefully, this requires a number of test simulations. In practice DEM time step should be small enough to resolve one particle collision in 10-20 time steps. This heuristic rule helps to determine values of spring constants and time step.

Once contact force have been calculated new particle positions and velocities are determined by integrating equation of motion as follows:

$$\begin{aligned} \vec{v_i} &= \vec{v_i}|_{t_1} + \vec{a_i}|_{t_1}\Delta t \\ \vec{r_i} &= \vec{r_i}|_{t_1} + \vec{v_i}|_{t_1}\Delta t \end{aligned} \tag{3.7}$$

For integration of rotational motion, generally same type of scheme is used as shown in equation 3.7. This scheme introduces a numerical propagation error which is not system generated. This requires more complicated integration schemes like Gear algorithm & Verlet algorithm [90]. These integration methods reduce the numerical error propagation but increase the complexity of the simulation.

Neighbour list

Neighbour lists are used to speed up the simulation process. This concept has originated from MD simulations [91]. In this algorithm, a cut-off distance is defined around the particle *i*. Particle-particle interaction is only calculated for the particles whose centre is in the cutoff radius as shown in figure 3.3. Cutoff distance needs to be decided very carefully. Higher cutoff distance means more particle interaction will be solved which will increase the simulation time while lower cutoff distance can result in poor simulation results.

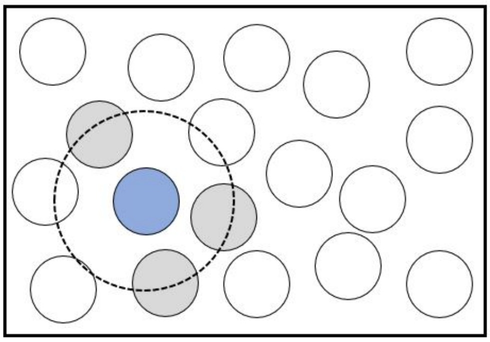

Figure 3.3: Neighbour list, Dotted line represents the cut-off distance. Grey particles are part of neighbour list for particle under observation.

In this study particle type is not a spherical but spherocylindrical, which requires a change in conventional DEM scheme to incorporate different particle type. An in-house code is built to incorporate these changes which are discussed in the following section.

3.1.2. Spherocylindrical particle contact model

Figure 3.4 shows a spherocylindrical particle. Cylinder length (L_{rod}) determine the aspect ratio which is L_p/D. Particle shape is spherical for $L_{rod} \approx 0$. This is the approach that has been used in this study to also simulate spherical particles?

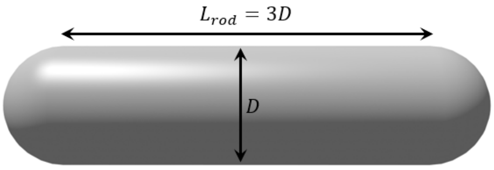

Figure 3.4: spherocylindrical particle with AR = 4.

Correlation discussed in section 3.1.1 are equally valid for all particles types. But calculation of overlap distance (δ) is not the same as of spherical particles. For spherocylindrical particles it is strongly dependent on the geometry of the particle thus other parameters like minimum distance between the particles ($\vec{r_{min}}$) and contact distance from centre of hemisphere ($\vec{s_i}$) comes into play. Particle length also plays a significant role in rotational motion because spherical particle are symmetric in all direction so I^m_{xx} and I^m_{yy} both depend just on the diameter. There are two approaches to simulate these particles:

1. Glued-sphere approach
2. True particle geometry approach

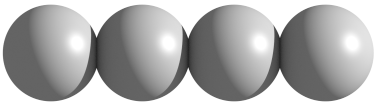

Figure 3.5: Particle Representation: Glued-sphere.

In glued sphere approach (see figure 3.5) spherical particles are connected without overlaps and each glued sphere particle act as one particle. While true particle geometry approach considers a true geometrical representation of the particle under observation. Guo et al. [47] has shown that results of simulation differs depending upon the approach. Although glued-sphere approach is easy to implement, it introduces a bumpy particle surface which not only result in interlocking between particles but also increases the particle stresses due to multiple overlaps for single particle. True particle geometry approach have been used in this study. Changes haven been made in LIGGGHTS-PUBLIC® to simulate the spherocylindrical particles.

The equations describing the contact model are given in Table 3.1. Points of the shortest distance $\vec{s}$ are found using a modified version of the algorithm described by Vega and Lago [92].

Table 3.1: Expressions describing the contact model.

#	Parameter	Expression(s)
1	Total contact force	$\vec{F}_{contact,i} = \sum_{j \neq i} (\vec{F}_{ij,n} + \vec{F}_{ij,t})$
2	Normal contact force	$\vec{F}_{ij,n} = -k_n \lvert\delta_{ij,n}\rvert \vec{n}_{ij} + \zeta_n \vec{v}_{ij,n}$
3	Tangential contact force	$\vec{F}_{ij,t} = \begin{cases} -k_t \lvert\delta_{ij,t}\rvert \vec{t}_{ij} + \zeta_t \vec{v}_{ij,t} & \text{for } \lvert\vec{F}_{ij,t}\rvert \leq \mu \lvert\vec{F}_{ij,n}\rvert \\ -\mu \lvert\vec{F}_{ij,n}\rvert \vec{t}_{ij} & \text{for } \lvert\vec{F}_{ij,t}\rvert > \mu \lvert\vec{F}_{ij,n}\rvert \end{cases}$
4	Point of contact	$\vec{r}_{c,ij} = \frac{\vec{s}_i + \vec{s}_j}{2}$
5	Normal overlap	$\delta_{ij,n} = d_p - \lvert\vec{s}_i - \vec{s}_j\rvert$
6	Tangential overlap	$\delta_{ij,t}(t) = \int_{t_c}^{t} \vec{v}_{ij,t} dt$
7	Relative velocity	$\vec{v}_{ij} = \vec{v}_j - \vec{v}_i + \vec{\omega}_j \times (\vec{r}_{c,ij} - \vec{r}_j) - \vec{\omega}_i \times (\vec{r}_{c,ij} - \vec{r}_i)$
8	Effective mass	$M_{eff,ij} = \frac{M_i M_j}{M_i + M_j}$
9	Contact time [93]	$t_c = \frac{M_{eff}}{k_n} \left(\pi^2 \ln(e_n)^2\right)$
10	Normal damping coefficient [93]	$\zeta_n = -\frac{2M_{eff}}{t_c} \ln e_n$
11	Tangential spring constant [93]	$k_t = t_c^{-2} \left(\frac{1}{M_{eff}} + 2 \frac{(\vec{r}_c - \vec{r}_i)^2}{\langle I \rangle} \right)^{-1} \left(\pi^2 + \ln(e_t)^2\right)$
12	Tangential damping coefficient [93]	$\zeta_t = -2t_c^{-1} \left(\frac{1}{M_{eff}} + 2 \frac{(\vec{r}_c - \vec{r}_i)^2}{\langle I \rangle} \right)^{-1} \ln e_t$
13	Total torque	$\vec{\tau}_i = \sum_{j \neq i} ((\vec{r}_{c,ij} - \vec{r}_i) \times (\vec{F}_{ij,t} + \vec{F}_{ij,n}) + \vec{\tau}_{ij,roll})$
14	Rolling friction [94]	$\vec{\tau}_{ij,roll} = -\mu_{roll} \lvert\vec{r}_i - \vec{r}_{c,ij}\rvert \lvert\vec{F}_{ij,n}\rvert \frac{\vec{\omega}_{ij}}{\lvert\vec{\omega}_{ij}\rvert}$
15	Moment of inertia [95]	$I_{yy}^m = \pi \rho_p \left(\frac{1}{2} R_p^4 L_{rod} + \frac{8}{15} R_p^5 \right)$ $I_{xx}^m = I_{zz}^m = \pi \rho_p \left(\frac{1}{12} R_p^2 L_{rod}^3 + \frac{83}{240} R_p^5 + \frac{4}{3} R_p^3 L_{rod}^2 + \frac{3}{4} R_p^5 + 2 R_p^4 L_{rod} \right)$

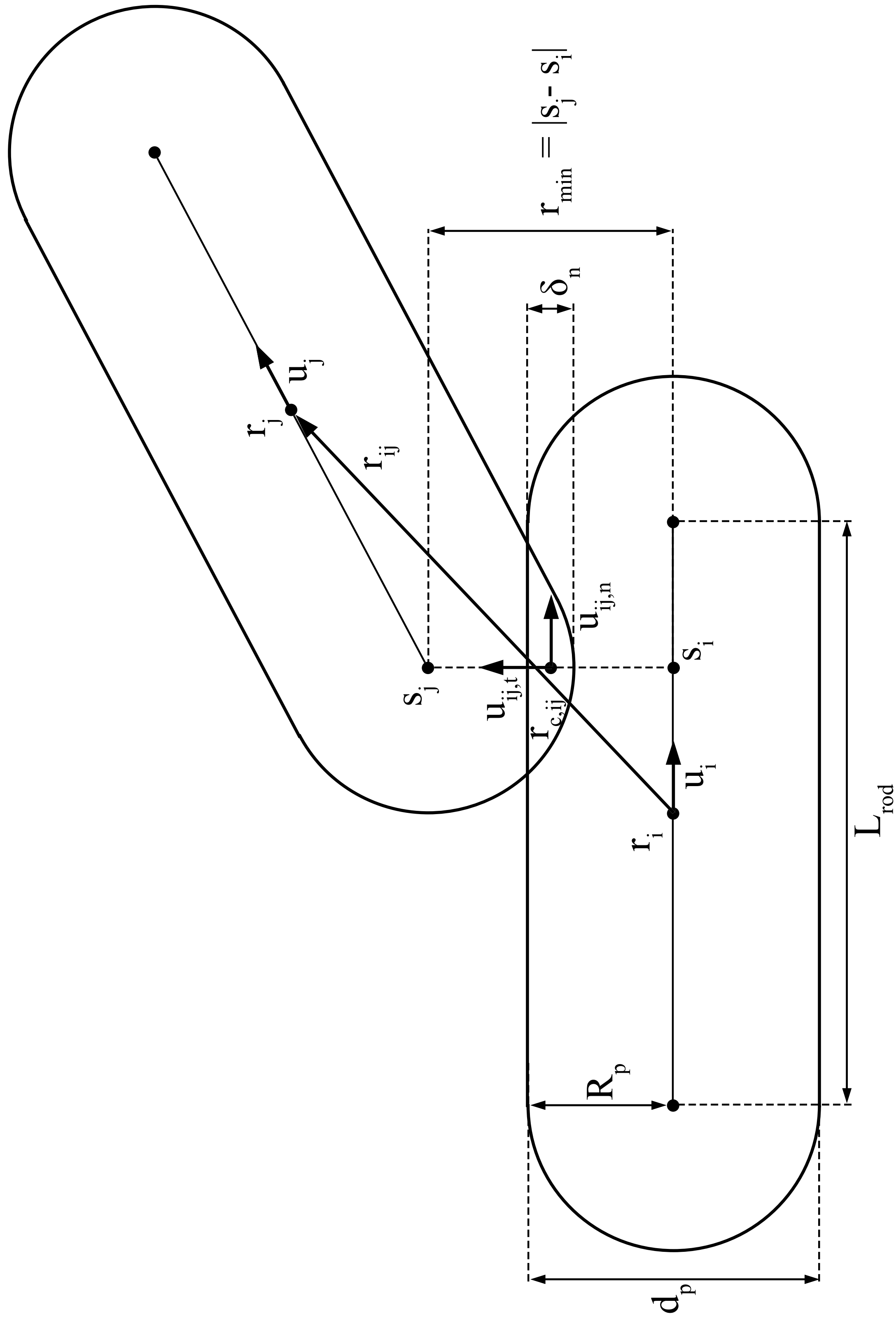

Figure 3.6: Particle-Particle contact scheme for spherocylindrical particles

Neighbour list

In this study, a multi-sphere shaped bounding volume is applied. As shown in Figure 3.7a, a compound shape consisting of 3 spheres tightly surrounds the spherocylinder. The distance between the satellite points and the centre of mass (COM) x_{sat} is given by Eq. 3.8, which was derived from geometry. In addition to the sphere radius (Eq. 3.9), a skin of radius R_{skin} is used to guarantee the neighbour list can be used for multiple time steps. When the maximum particle displacement since the last neighbour list build surpasses $R_{skin}/2$, a new list is created. A similar approach is used to build the particle-wall neighbour list, shown in Figure 3.7b. Since the closest distance between a particle and a wall is always located at one of the tips of the particle, the spheres are only centred around the ends of the rod.

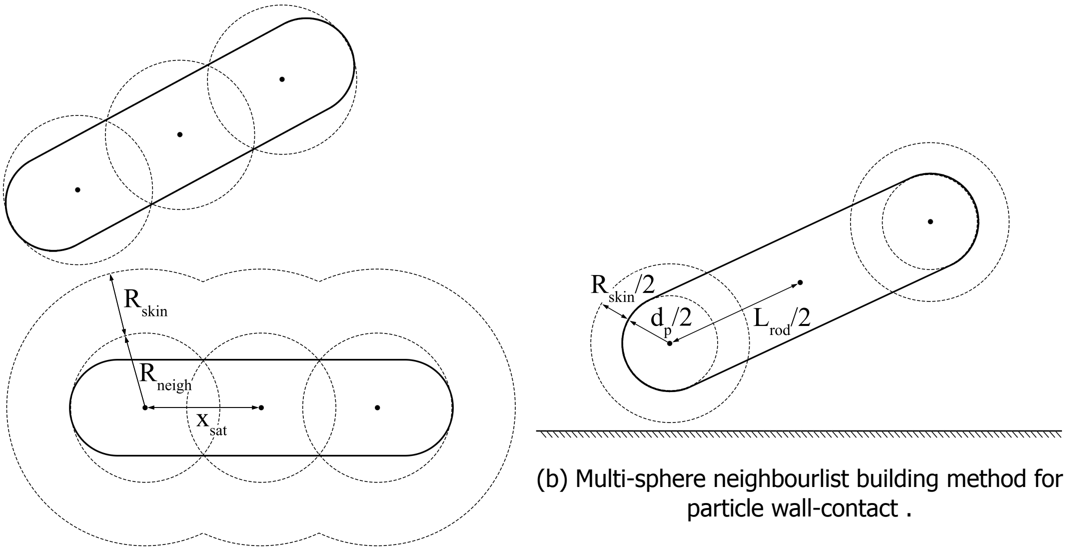

(a) Multi-sphere neighbourlist building method for particle-particle contact. x_{sat} and R_{neigh} are given by Eqs. 3.8 and 3.9

(b) Multi-sphere neighbourlist building method for particle wall-contact .

Figure 3.7: Neighbour List: Spherocylindrical Particle [96]

$$x_{sat} = \frac{1}{3}\left(-\sqrt{4d_p^2 + 2dL_{rod} + L_{rod}^2} + 2(d_p + L_{rod})\right) \tag{3.8}$$

$$R_{neigh} = \sqrt{\left(\frac{x_{sat}}{2}\right)^2 + \left(\frac{d_p}{2}\right)^2} \tag{3.9}$$

3.2. Computational fluid dynamics

3.2.1. Flow solver

CFDEM®coupling depends upon OpenFOAM®, an open source CFD toolbox, to solve the gas flow. OpenFOAM uses the PISO and SIMPLE [97] algorithms to solve the phase continuity and momentum transport equation for incompressible (gas density is assumed constant), Newtonian, laminar flow [98]. These equations are given in Eq. 3.10 and 3.11 respectively, also known as Model A in literature. Here, $\vec{u}$ is the gas phase velocity, and $\vec{S}_{f,p}$ is the momentum exchange between fluid and particles, ϕ_f is the fluid volume fraction and σ_f is fluid stress tensor. This model was recommended by Zhou et al. [98] for use in CFD-DEM modelling. Further details on algorithms used in the CFD model will not be shared here, as they are outside of the scope of this report.

$$\frac{\partial \phi_f \rho_f}{\partial t} + \nabla \cdot (\phi_f \rho_f \vec{u}) = 0 \tag{3.10}$$

$$\frac{\partial \phi_f \rho_f \vec{u}}{\partial t} + \nabla \cdot (\phi_f \rho_f \vec{u}\vec{u}) = -\phi_f \nabla P + \nabla \cdot (\phi_f \sigma_f) + \phi_f \rho_f \vec{g} + \vec{S}_{f,p} \tag{3.11}$$

3.2.2. Void fraction calculation

The gas flow field depends on the local void fraction in each point in the bed. To calculate this local void fraction, the volume of a particle is assigned to not one, but multiple cells when it surpasses cell boundaries. Instead of assigning the particle volume to the cell in which its centre of mass lies, a distributed void fraction calculation is used. Each particle possesses 16 satellite points, placed evenly in the particle volume as shown in Figure 3.8. Each cell containing such a satellite point is assigned a fraction of the particle volume, creating a more continuous void fraction field and preventing sudden jumps in local porosity.

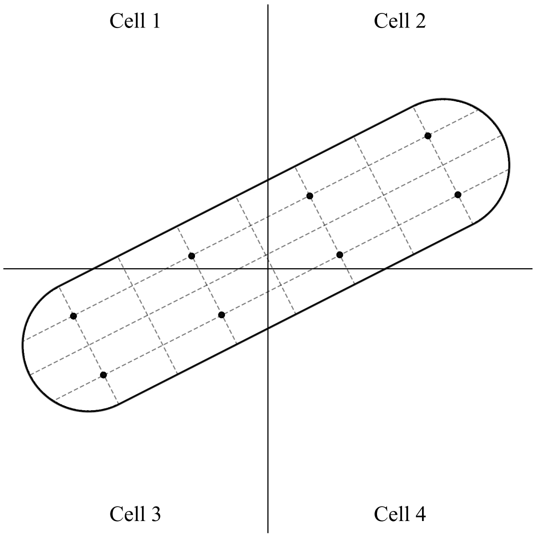

Figure 3.8: The particle volume is distributed among the cells according to the location of the 16 satellite points. Eight more points are located in the plane perpendicular to the shown cross-section. [96]

3.3. Gas-particle coupling

3.3.1. Dilute regime

Holzer and Sommerfeld drag

Hölzer and Sommerfeld [11] derived an equation describing the drag coefficient for a single non-spherical particle in a gas flow (Eq. 3.12). Here $\vec{v}_r$ is the relative velocity between the particle and the gas. This equation incorporates the orientation of the particle in the crosswise ($\phi_\perp$) and lengthwise sphericity ($\phi_\parallel$), given by Eqs. 3.14 and 3.15 respectively. These are calculated based on θ, the angle between the particle orientation vector and the gas velocity vector.

$$C_{D0} = \frac{8}{\mathrm{Re}}\frac{1}{\sqrt{\phi_\parallel}} + \frac{16}{\mathrm{Re}}\frac{1}{\sqrt{\phi}} + \frac{3}{\sqrt{\mathrm{Re}}}\frac{1}{\phi^{\frac{3}{4}}} + 0.4210^{0.4(-\ln\phi)^{0.2}}\frac{1}{\phi_\perp} \tag{3.12}$$

$$\mathrm{Re} = \frac{\phi|\vec{v}_r|d_e\rho_g}{\mu_g} \tag{3.13}$$

$$\phi_\perp = \frac{A_e}{A_{p,\perp}} \text{ where: } A_{p,\perp} = \pi d_p^2 + d_p L_{rod}\sin(\theta) \tag{3.14}$$

$$\phi_\parallel = \frac{2A_e}{A_{p,tot} - 2A_{p,\parallel}} \text{ where: } A_{p,\parallel} = \pi d_p^2 + d_p L_{rod}\cos(\theta) \tag{3.15}$$

Figure 3.9 (left) shows the single-particle drag coefficient as a function of Reynolds, compared with single-particle Direct Numerical Simulation (DNS) results; the Zastawny model [99] extended for spherocylinders [100] and the Krishnan model [101]. It can be seen that the correlation by Holzer and Sommerfeld is in good correspondence with DNS results.

Voidage correction

The drag force acting on a single particle in a gas flow is given by Eq. 3.16. Di Felice [102] developed a correlation describing the effect of local void fraction on the drag force (Eq. 3.17 and Eq. 3.18). Here ϕ is the local void fraction around the particle.

$$\vec{F}_{D0} = \vec{v}_r|\vec{v}_r|C_{D0}\frac{1}{2}\rho_g\frac{\pi}{4}d_e^2 \tag{3.16}$$

$$\vec{F}_D = \vec{F}_{D0}\phi^{2-\beta} \tag{3.17}$$

$$\beta = 3.7 - 0.65\exp\left(-\frac{(1.5-\ln \mathrm{Re})^2}{2}\right) \tag{3.18}$$

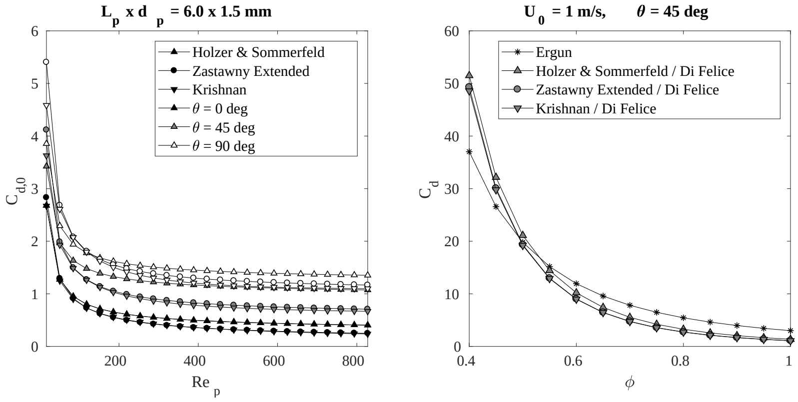

Figure 3.9: Left: single particle drag coefficient as a function of Reynolds number. Right: Drag coefficient with voidage correction as a function of void fraction.

As the drag model derived by Holzer and Sommerfeld was derived for single particles, it does not fully describe the drag force in dense regions. Gidaspow [103] recommends the use of the Ergun equation [104] in dense regions, as it is derived for a dense, packed bed. Despite the fact that it was derived from spherical particles, this equation also accurately describes the pressure drop over a bed of non-spherical particles [96]. The drag force on a particle derived from the Ergun equation is given by Eq. 3.19. The smallest of the Holzer-Sommerfeld and Ergun drag forces are used. Figure 3.9 (right) shows the drag coefficient with voidage correction by Di Felice as a function of void fraction, alongside the drag coefficient predicted by the Ergun equation.

$$\vec{F}_D = \frac{\Delta P_{cell}}{L_{cell}}A_{cell}L_{cell}\frac{V_p}{V_{cell}}\frac{\phi}{1-\phi} = V_p\frac{\vec{v}_r\rho_g}{\phi d_e}\left(150\frac{\nu_g}{\phi d_e}\frac{1-\phi}{\phi} + 1.75|\vec{v}_r|\right) \tag{3.19}$$

3.4. Measurements

3.4.1. Stress tensor

Stress $\vec{\sigma}$ at any point in the material can be completely defined by 9 components, σ_{ab}. Each component can be specified by two subscripts,

1. *a* specifies the orientation of the plane on which stress is acting
2. *b* specifies the direction in which stress is acting

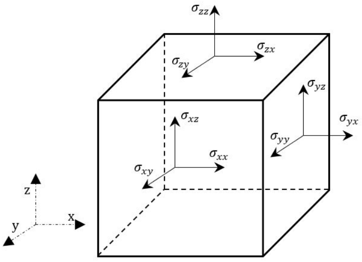

Figure 3.10: Components of Stress in three Dimensions

All of these nine components are arranged in a matrix as follows:

$$\vec{\sigma} = \begin{bmatrix} \sigma_{xx} & \sigma_{xy} & \sigma_{xz} \\ \sigma_{yx} & \sigma_{yy} & \sigma_{yz} \\ \sigma_{zx} & \sigma_{zy} & \sigma_{zz} \end{bmatrix} \tag{3.20}$$

$\vec{\sigma}$ can be determined by calculation of forces per unit area. For particle-particle contact, stresses are combination of two independent contributions i.e streaming stress tensor ($\vec{\sigma}_s$) due to particle momentum flux & collisional stress tensor ($\vec{\sigma}_c$) due to particle collisions. In simulations both of these stress tensors are calculated as follows [105]:

$$\vec{\sigma}_t = \vec{\sigma}_s + \vec{\sigma}_c \tag{3.21}$$

$$\vec{\sigma}_s = \frac{1}{V_{cb}} \sum_{i} \left(M_i \vec{v_i}' \vec{v_i}' \right) \tag{3.22}$$

$$\vec{\sigma}_c = \frac{1}{V_{cb}} \sum_{i \neq j} \left(\vec{F_{ij}} \vec{r_{ij}} \right) \tag{3.23}$$

$$\vec{v_i}' = \vec{v_i} - \vec{v_{avg}} \tag{3.24}$$

$\vec{v_i}'$ is the velocity fluctuations for particle *i* which is calculated from average velocity of the particles in the domain.

3.4.2. Granular temperature

Granular temperature (T) is a measurement of residual kinetic energy in the system. It can be calculated by velocity fluctuations of the particles as follows:

$$T = \frac{1}{3} \left[v_x'^2 + v_y'^2 + v_z'^2 \right] \tag{3.25}$$

Detailed discussion on the granular temperature measurement is in chapter 4 (section 4.4.4).

3.4.3. Particle orientation

Particle orientation is an important parameter when it comes to spherocylindrical particles which can be defined by a unit vector along the rod major axis. In the LIGGGHTS-PUBLIC rotation of the particle is represented by quaternions with z-axis as the rotational axis. Quaternions are an extension of the complex number but in 4-D to define an object rotation around an axis. They are generally represented in the following form:

$$Q = w + q\vec{i} + q\vec{j} + q\vec{k} \tag{3.26}$$

Unit vector can be easily calculated from quaternion by following algorithm:

$$\vec{RM} = \begin{bmatrix} 1 - 2q_j^2 - 2q_k^2 & 2q_i q_j - 2q_k w & 2q_i q_k + 2q_j w \\ 2q_i q_j + 2q_k w & 1 - 2q_i^2 - 2q_k^2 & 2q_j q_k - 2q_i w \\ 2q_i q_k - 2q_j w & 2q_j q_k + 2q_i w & 1 - 2q_i^2 - 2q_k^2 \end{bmatrix} \tag{3.27}$$

$$\vec{U} = \vec{R} x \vec{k} \tag{3.28}$$

In the simulation unit vector of all the particles were averaged to find a unit vector for whole assembly. This unit vector was further used to defined the angle between rod orientation and shear direction.

4

Simulation setup

Simulations in this study are performed in a control box for different volume fraction and shear rates. Control box used in these simulations is periodic in *x* & *y* direction. Boundary condition to shear the system is different than Lees-Edwards boundary condition [106] used in previous similar studies. In Less-Edward boundary condition a periodic box, which is exact replica of the system under observation, is used to shear the domain while in this study shear rate is applied in the *z* direction with the moving z-wall and the fluid simultaneously (figure 4.1). Fluid velocity is maintained at constant value throughout the simulation near the z-walls. Height of the domain is the important parameter of the control box because system is periodic in other directions which is taken as "8 x particle length". Depending upon the particle type (spherocylinder or spheres) domain height is changed accordingly. Rest of the parameters are listed in table 4.1. Domain Independence analysis (Appendix A) was performed before finalizing the domain boundaries. Contact parameters are taken from single particle experiments performed by Nijssen [96].

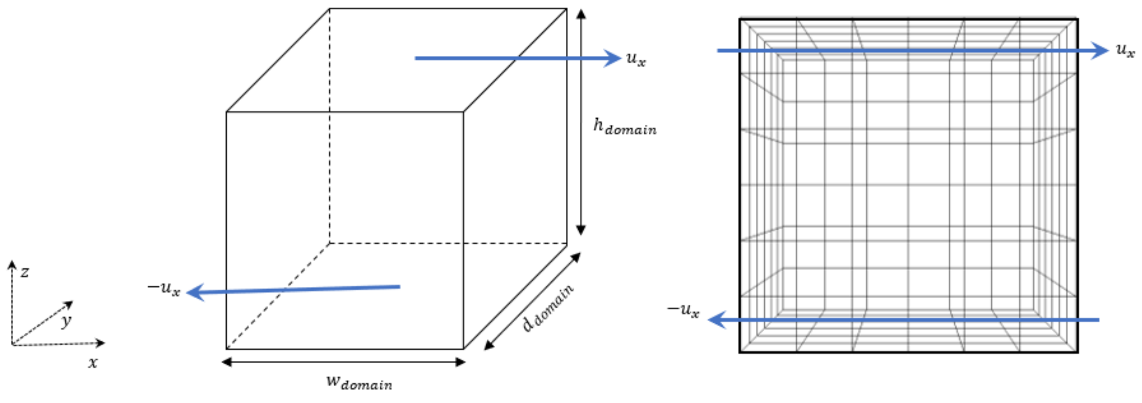

DEM Domain

CFD Mesh Grid

Figure 4.1: Simulation Setup.

Table 4.1: Parameters of the simulation.

Parameters		Spherocylinders	Spheres	
Domain height	h_{domain}	0.096	0.044	m
Domain width	w_{domain}	0.1	0.05	m
Domain depth	d_{domain}	0.1	0.05	m
Rod length	L_r	$9 \cdot 10^{-3}$	$5.30 \cdot 10^{-5}$	m
Particle diameter	d_p	$3 \cdot 10^{-3}$	$5.30 \cdot 10^{-3}$	m
Particle density	ρ_p	1395	1395	kg/m³
Coefficient of friction	μ	0.46		-
Coefficient of rolling friction	μ_{roll}	0.025		-
Coefficient of restitution	e	0.43		-
Normal spring constant	k_n	6000		N/m
fluid density	ρ_f	1.2		kg/m³
fluid viscosity	η_f	$1 \cdot 10^{-3}$		Pa···s
Number of CFD cells (width)	$N_{cells,x}$	6		-
Number of CFD cells (depth)	$N_{cells,y}$	6		-
Number of CFD cells (height)	$N_{cells,z}$	6		-

4.1. Variable space

Prior to preforming controlled simulation for stress measurements, it needs to be determined what is typical shear rate and volume fraction experienced in fluidized bed simulation. A full fluidized bed is simulated for superficial velocity of 3.0 ms^{-1} and 7820 particles as shown in figure 4.2 to find out the probability density function (PDF) of these parameters. PDF is calculated based on shear rate and volume fraction values in the CFD cells of the simulation.

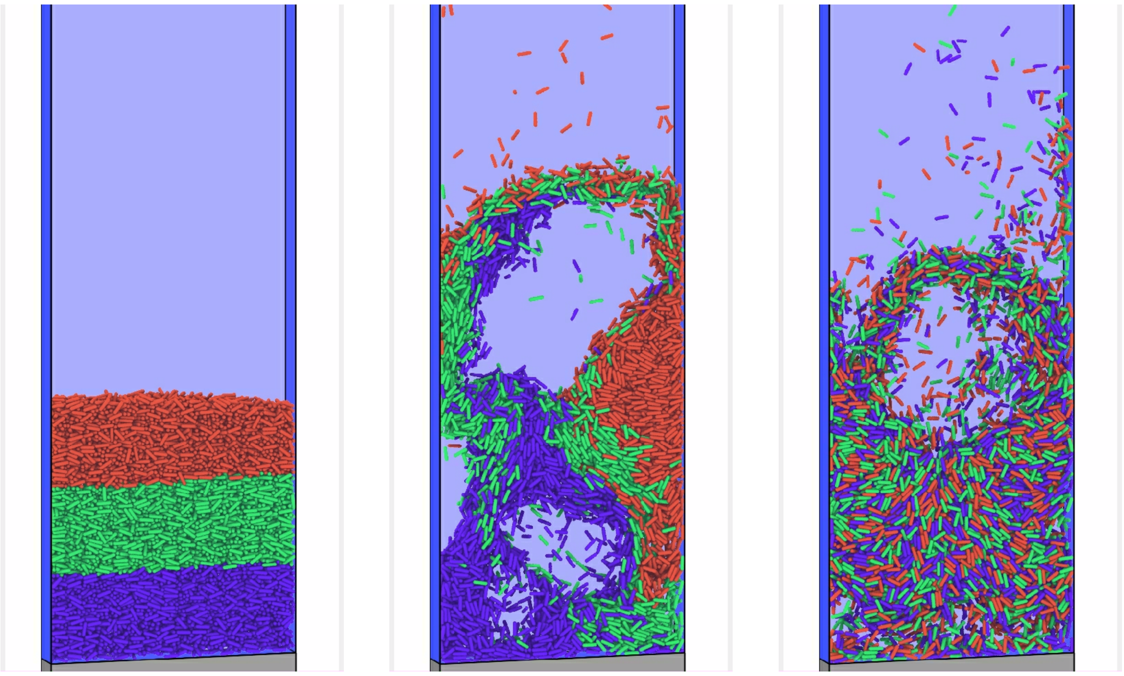

(a) t = 0s (b) t = 1s (c) t = 10 s

Figure 4.2: Snapshot of fluidized bed simulation at different time steps

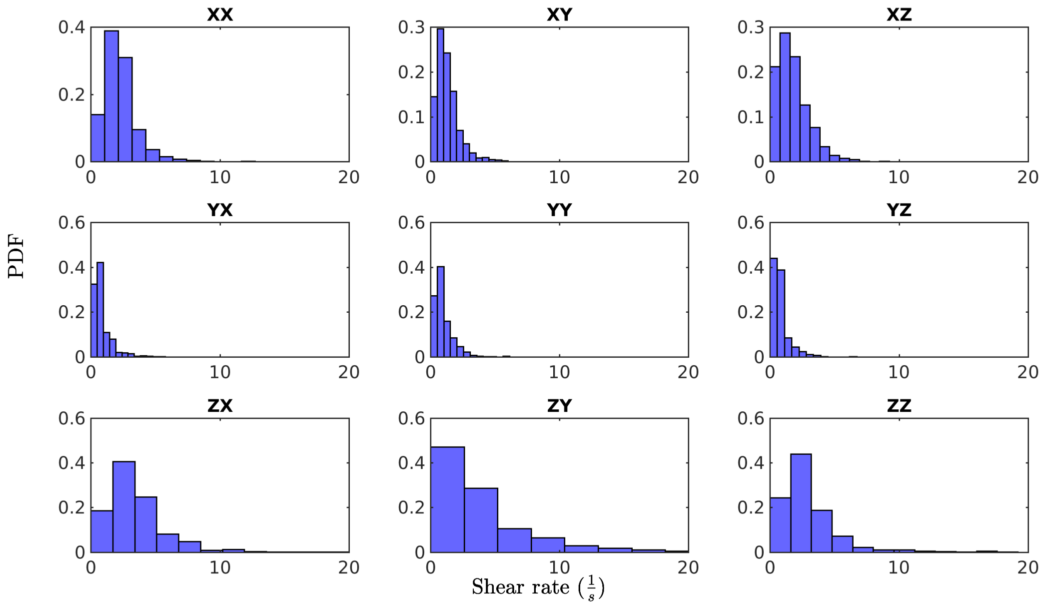

Figure 4.3: PDF of Shear rate components for fluidized bed simulation.

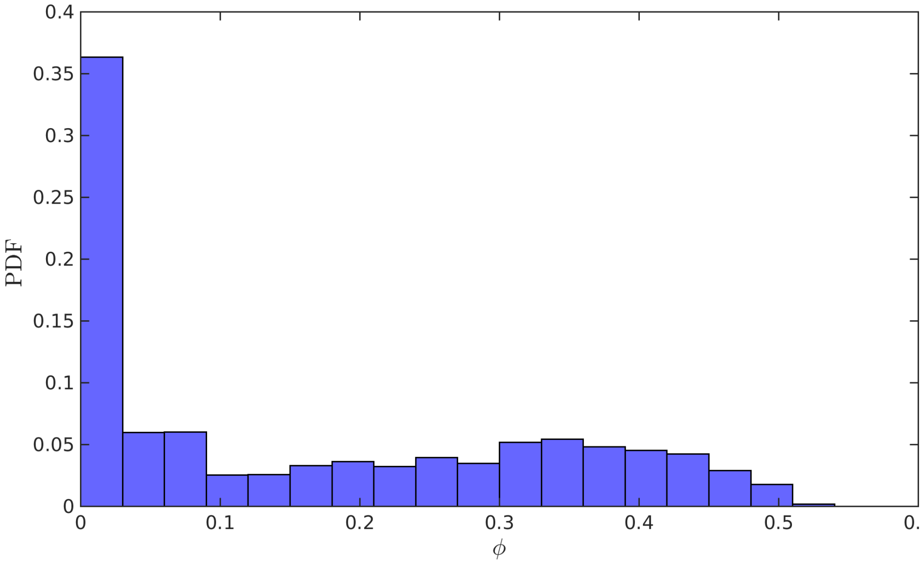

Figure 4.4: PDF of volume fraction for fluidized bed simulation.

In this simulation gas velocity is applied in z-direction so most important shear rate which governs the particle behaviour is $\dot{\gamma}_{xz}$ (shear on the x-plane in z-direction). It is evident from the figure 4.3 that this shear rate varies from 0 to 10/s. Volume fraction in a fluidized bed varies from 0.1 to 0.5 as shown in figure 4.4. Based on above variable space is listed in the table 4.2. Although maximum shear rate encountered in the fluidized bed is 10/s, values up till 100/s are simulated to study the rheology of spherocylindrical particles.

Table 4.2: Variable space for control box simulations.

Shear rate ($\frac{1}{s}$)	0.1-0.5	0.8	1	2	3	5	10	20	30	40	50	75	100
Volume fraction				0.1	0.2	0.3	0.4	0.5					

4.2. Initialization

For each volume fraction, number of particles used are listed in table 4.3. Simulations are initialized by arranging particles in z-direction as shown in figure 4.5. Afterwards each of the particle is given random linear and angular velocities at t=0. Only DEM is used to simulate the particles motion un-till all particles achieved zero velocity again. In this manner a system is generated with total random particle orientation and position in the control box (figure 4.6). It is not possible to achieve a total random system for volume fraction 0.4 & 0.5 because there is not much space available for the particles to move.

Table 4.3: Number of Particles for different volume fractions

Volume fraction	No. of Particles	
	Spherocylinders	Spheres
0.1	1235	139
0.2	2469	279
0.3	3764	418
0.4	4939	558
0.5	6173	697

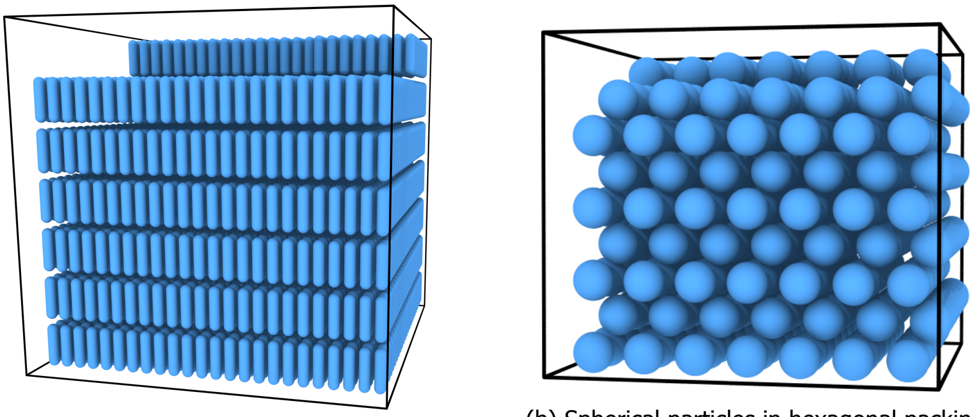

(a) spherocylindrical particles

(b) Spherical particles in hexagonal packing

Figure 4.5: Initialisation scheme for volume fraction = 0.3.

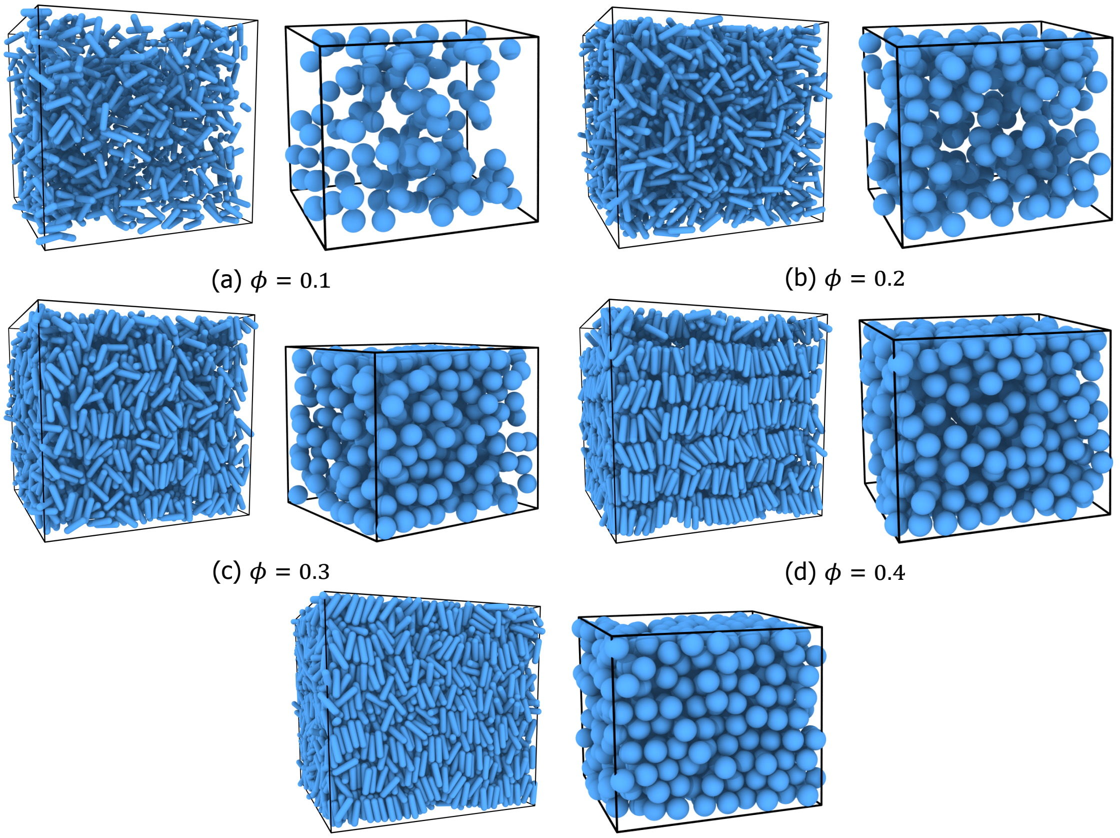

(a) $\phi = 0.1$ (b) $\phi = 0.2$

(c) $\phi = 0.3$ (d) $\phi = 0.4$

(e) $\phi = 0.5$

Figure 4.6: System state at Initialization.

4.3. CFD-DEM coupled simulation

After the initialization, simulation time is set to zero again to start a CFD-DEM coupled simulation. Time parameters are listed in table 4.4. DEM time step is based on the guidelines discussed in section 3.1.1. Usually 10 DEM time steps are enough to resolve particle-particle interactions. CFD time scale is different than DEM time scale because for 10 DEM time steps fluid velocities does not change a lot in one CFD cell. That is why CFD time step is ten times larger than DEM time step. This means that during one CFD time step, DEM will be called 10 times.

Table 4.4: Time parameters for the CFD-DEM coupled simulations

Parameter	Value	
Start time	0	s
End time	120-400	s
DEM time step	1.10^{-5}	s
CFD time step	1.10^{-4}	s
Writing interval	0.01	s

Fluid & wall velocities are calculated based on the desired simulated shear rate as follows:

$$\pm u_x = \frac{\dot{\gamma} h_{domain}}{2} \tag{4.1}$$

Measurements for the stresses and other important quantities are performed two particle length away from the z-walls to ensure that there is no effect of wall interactions on the particle-particle stresses (figure 4.7). Writing interval for all the measurements is set to 1000 DEM time step (0.01 sec) to reduce the amount of raw data and also to make sure that two consecutive measurements are independent of each other.

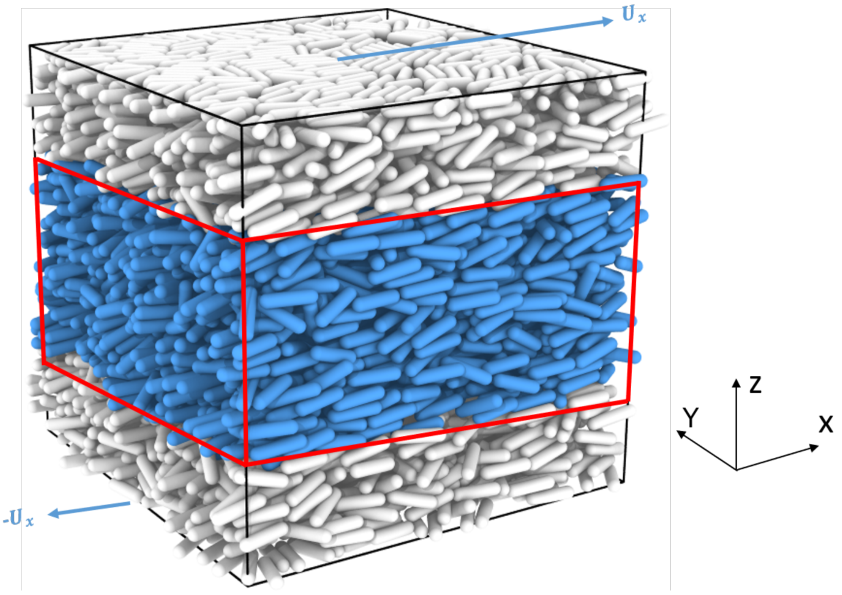

Figure 4.7: Snapshot of CFD-DEM coupled simulation setup. Red box indicates measurement domain.

4.4. Measurements

In the following sections, only spherocylindrical simulations have been discussed but same post-processing is applied to the spherical particle simulations.

4.4.1. Volume fraction

Particle number density in the measuring domain changes during the simulations. This phenomenon is used to estimate quasi-steady state of the system, a state in which volume fraction inside measuring domain remains constant. An algorithm is developed to find quasi-steady time. For each simulation, this time is highly dependent on the simulation parameters (volume fraction & shear rate, see figure 4.8).

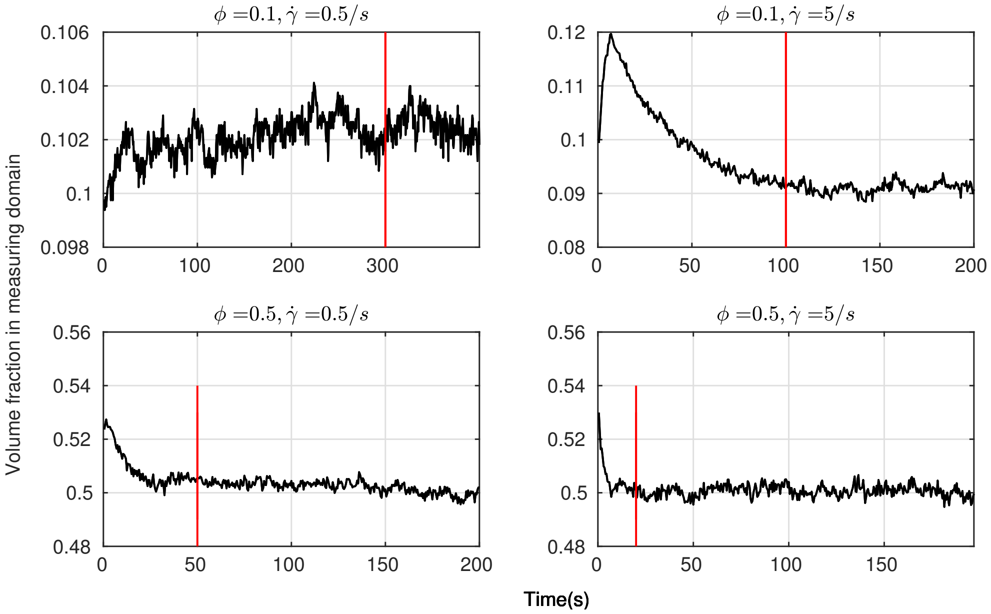

Figure 4.8: Change in particle number density for different input parameters. Red line represents the start of quasi-steady state.

Viscosity of the fluid phase for these simulation is $1 \cdot 10^{-3}(Pa.s)$ as opposed to viscosity of air $(1 \cdot 10^{-5}Pa.s)$ used in real fluidized bed simulations. Quasi steady state time of the simulation is the main factor behind this decision. Figure 4.9 shows the volume fraction change in the measuring domain for $\phi = 0.1$ and $\dot{\gamma} = 2/s$. For η_f of $1 \cdot 10^{-5}Pa.s$ system reaches at quasi steady state after 500 sec. Simulation for this system was completed in two weeks. Although viscosity of fluid phase does have effect on particle stresses (appendix B), $\eta_f = 1 \cdot 10^{-3}(Pa.s)$ is chosen to simulate the system to complete the simulations in less time and further analysis is based on this high viscous system.

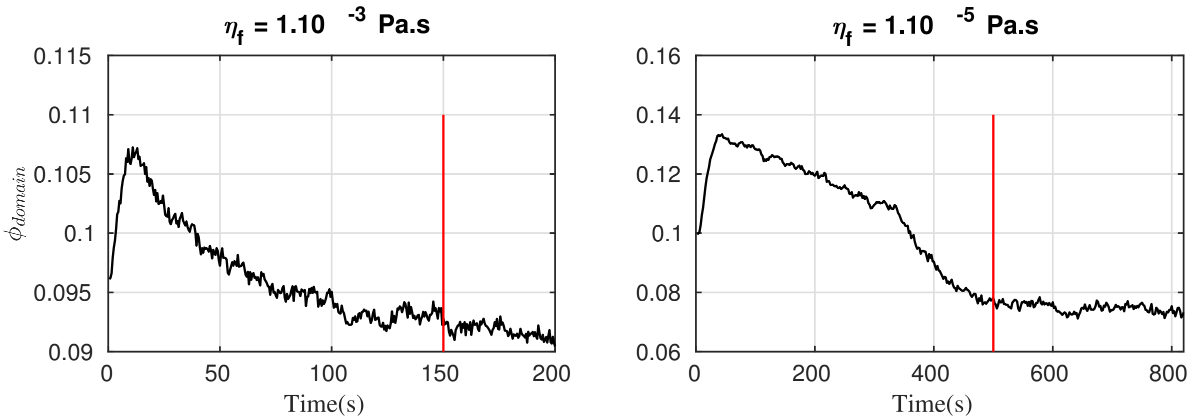

Figure 4.9: Change in particle number density for different fluid viscosities. Red line represents the start of quasi-steady state.

4.4.2. Shear rate

Just like volume fraction, the shear rate for the measuring domain is different than the shear rate applied at the z-walls. Particle velocities at the limit of measuring domain in the z-direction are used to find the actual shear rate[1] (see figure 4.10a). $\dot{\gamma}_{domain}$ is also highly dependent on the volume fraction of the system as shown in figure 4.10b. For higher volume fractions $\dot{\gamma}_{domain}$ is much lower than $\dot{\gamma}_{wall}$ because at higher volume fractions there are more particles present which causes the resistance to the flow.

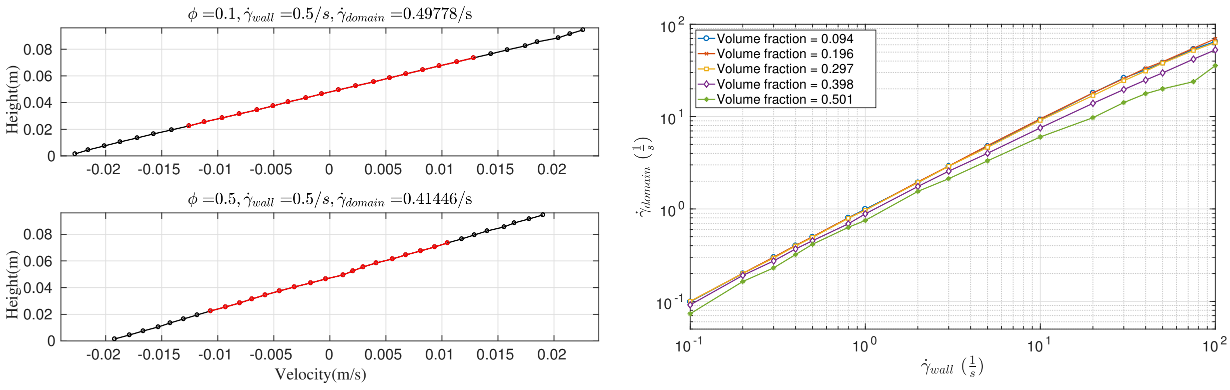

(a) Average particle velocities for different volume fraction at $\pm u_x = 0.024(\frac{m}{s})$. Red line represent the velocity distribution in the measurement box.

(b) Shear rate at measuring domain for different volume fractions. Volume fraction in legend is averaged volume fraction in the measuring domain for all shear rates.

Figure 4.10: Change in shear rate at measuring box for different volume fractions.

---

[1] In this report, $\dot{\gamma}$ represents actual shear rate for the measuring domain

4.4.3. Stress tensor

Streaming Stress tensor: Streaming stress tensor is calculated via correlation (equation 4.2) used also by Campbell and Gong [17].

$$\vec{\sigma}_s = \rho_p \phi \begin{bmatrix} < v_x'^2 > & < v_x' \cdot v_y' > & < v_x' \cdot v_z' > \\ < v_y' \cdot v_x' > & < v_y'^2 > & < v_y' \cdot v_z' > \\ < v_z' \cdot v_x' > & < v_z' \cdot v_y' > & < v_z'^2 > \end{bmatrix} \tag{4.2}$$

<> represent the particle averaging. Equation 4.2 and 3.22 are inherently the same equation, differences arises in estimation of the fluctuations. While equation 3.24 can be used to find the velocity fluctuations during the simulation, opposite velocities at z and $-z$ walls makes v_{avg} approximately zero for present system. Different approach is utilized to find the velocity fluctuations for equation 4.2 as mentioned in equation 4.3:

$$< a' b' >=< ab > - < a >< b > \tag{4.3}$$

Simulation domain is split into vertical bins. Fluctuation of velocities are calculated in each bins with equation 4.3 for every 0.01 sec. These fluctuations are averaged for measuring domain to find out the streaming stress tensor.

Collisional stress tensor: Colliosional stress tensor is measured during the simulation for every 0.01 sec via equation 3.23. Savitzky–Golay filter [107] is used to visualize the trend for collisional stress tensor over time. This filter fits a nth order polynomial to consecutive subsets of data via least-square method to smooth the data set (figure 4.11a).

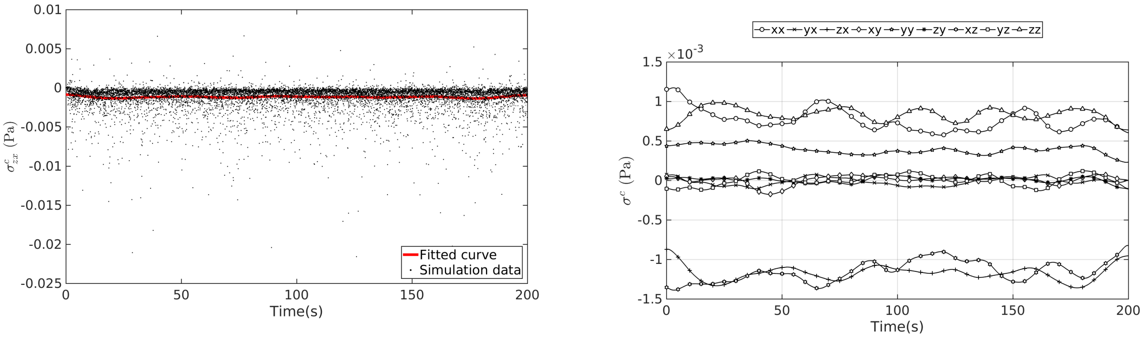

(a) Smoothing of the data via Savitzky-Golay filter for σ_{zx} .

(b) Behaviour of stress tensor components over time.

Figure 4.11: Collisional stress tensor for $\phi = 0.3$, $\dot{\gamma} = 4.80/s$.

4.4.4. Granular temperature

Granular temperature is calculated via equation 3.25. Velocity fluctuation are computed by the equation 4.3 just like for the streaming stress tensor. Test simulations are performed to find out the right number of bins so that results are independent of number of bins in the domain. It is found that for spherocylindrical system, granular temperature become independent of number of bins after 32 bins (figure 4.12). For spherical particle simulations this number is 16. Same number of bins are used to calculate the streaming stress tensor.

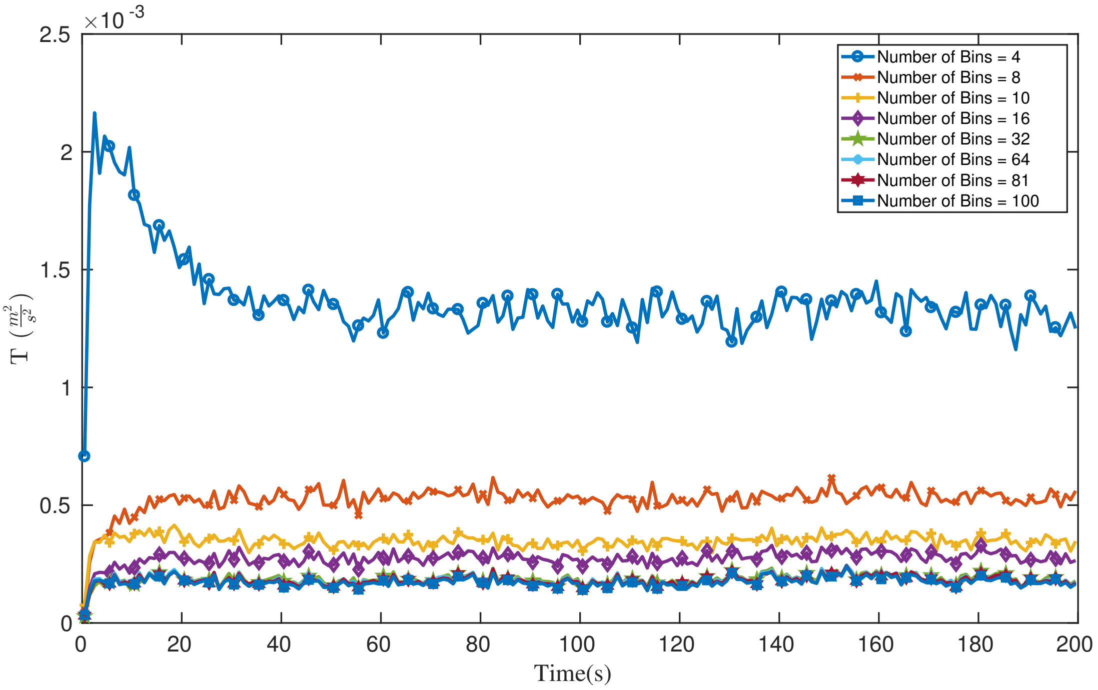

Figure 4.12: Bin independence analysis for granular temperature of sphero-cylindrical particles at $\phi = 0.2$, $\dot{\gamma} = 4.86/s$.

4.4.5. Particle orientation

Quantitative representation: Unit vector obtained from equation 3.28 is used to find the angle (θ) between particle and shear direction $\vec{x}$.

$$\vartheta = \arccos \frac{\vec{U} \cdot \vec{x}}{|\vec{U}||\vec{x}|} \tag{4.4}$$

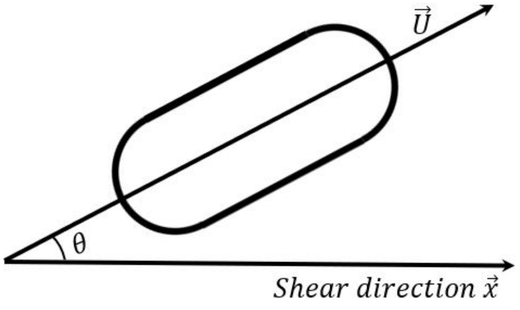

Figure 4.13: Angle between particle major axis and shear direction.

Qualitative representation: Super quadratic glyphs can be used to visualize the orientation of diffusion tensor from human brain scans [108]. This technique is used to visualize particle orientation in 3-D. With shape of super quadratic glyph it can be easily shown if particles are oriented uni-axially, bi-axially or randomly (figure 4.14). A MATLAB® graphic user interface(GUI) is developed to follow the particle orientation with time. Super quadratic framework is completely explained in Kindlmann [108]. MATLAB implementation of this framework is attached as appendix D.

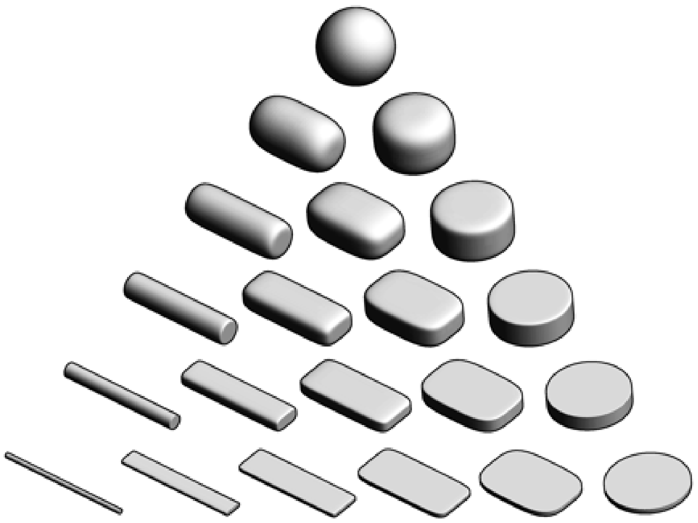

Figure 4.14: Super quadratic glyph representation [108] of orientation tensor. From left to right alignment changes from uni-axial to bi-axial. From bottom to top system is moving towards isotropy.

Figure 4.15 shows the particle orientation of initial state of the simulation. One can easily observe that for lower volume fractions system is totally isotropic at t=0, while for higher volume fractions particles are uni-axially aligned.

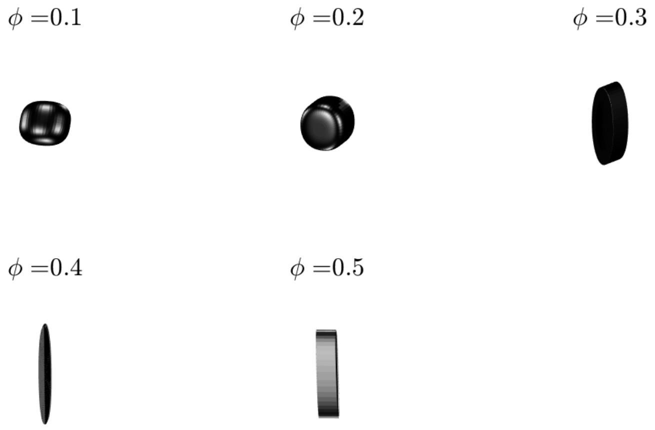

ϕ =0.1

ϕ =0.2

ϕ =0.3

ϕ =0.4

ϕ =0.5

Figure 4.15: Super quadratic glyphs for spherocylindrical particles initial setup as shown in figure 4.5.

4.5. Time averaging

For all measured quantities time averaging is performed for each simulation after quasi-steady state has been achieved. Quasi-steady state is estimated via volume fraction as mentioned in section 4.4.1. At-least 100 sec are considered after the quasi-steady state time is achieved to find out the time averaged measurement. In chapter 5 results are presented in terms of time averaged quantities for each simulation. Appendix C shows the procedure of time averaging.

5

Results and discussion

In the following sections, rheology of spherocylindrical particles has been discussed in terms of the stress tensor, granular temperature, particle orientation, pressure and stress differences. Simulation results of spherical particles[1] are used as the base case for stress tensor discussion only. Then, particle collisional stresses have been examined thoroughly to form a constitutive equation in terms of shear rate, volume fraction and system properties.

5.1. Stress tensor

Streaming component, collisional component and total stress of shear stresses are plotted as a function of shear rate in figure 5.1, 5.2 & 5.4 respectively.

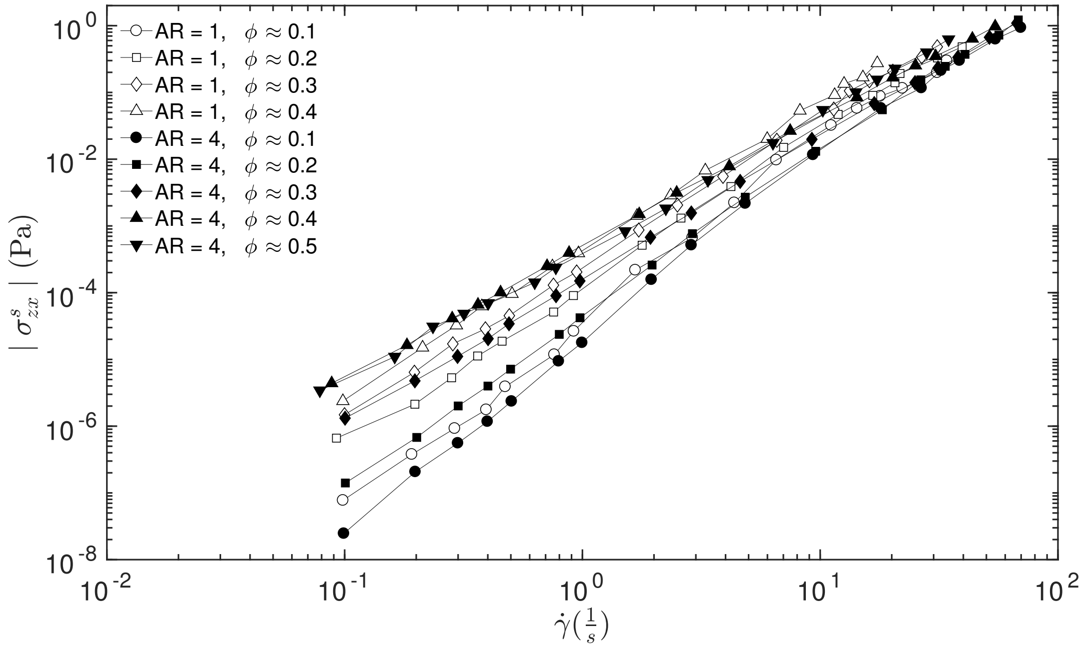

Figure 5.1: Streaming component of shear stresses.

As shown in figure 5.1 streaming stress tensor increases with shear rate and it follows the same trend for both aspect ratios. For spherocylindrical particles, streaming shear stresses are slightly lower than spherical particles. This is due to the fact that due to particle collisions elongated particles rotate. Contact vector ($\vec{s_i}$) does not pass through the centre of the particle most of the time and results in

---

[1] Spherical particle simulation of $\phi = 0.5$ are not included in the discussion due to presence of yield stress also reported by Campbell [28] and Mueller et al. [78] for high volume fractions.

torque moments. This rotation requires an energy conversion from translational to rotational part. Some of the energy is lost in this conversion and results in lower stress values. Streaming stress is basically a representation of the kinetic energy of the system. With increasing volume fraction there exist more particles. This should result in higher streaming stresses but that is only true for lower shear rates as shown in figure 5.1. For higher shear rate streaming stresses for all volume fractions are almost the same. This can be explained by considering collision time between particles. For $\dot{\gamma} > 1$, at lower volume fraction collision time starts to decrease but particle still has space to move around. For higher volume fractions there exist very little space for particles to move. Thus velocity fluctuations for higher volume fractions are lower. As streaming stress is a multiple of particles mass and velocity fluctuations (equation 3.22). Value remains fairly in the same range for all volume fractions at high shear rates.

For collisional shear stresses, as shown in figure 5.2, stresses increases gradually for spherocylindrical particles with shear rate and also with volume fraction. For spheres there is sudden increase in stress values at $\dot{\gamma} = 1$. Bagnold theory [49] can be used to explain this phenomenon.

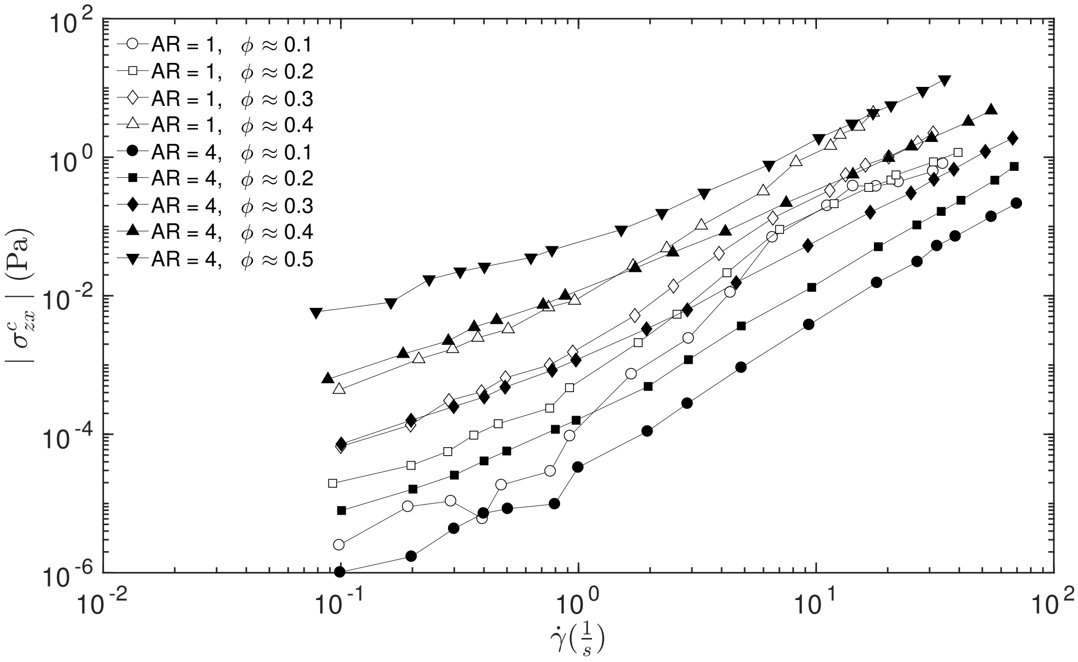

Figure 5.2: Collisional component of shear stresses.

Collisional stresses are plotted against Bagnold number for spherical particles in figure 5.3. It is very obvious that this sudden increase in particle stresses are due to the change in system regime. For $\dot{\gamma} > 1$ particle collision are occurring more frequently which results in higher collisional stresses. The volume fraction of 0.1 shows a strong dependence on the shear rate.

For spherocylindrical particles stress values do not show this sudden jump but increase gradually. Collisional stresses for spherocylindrical particles are also lower than spherical particles. This can be attributed to two different phenomena,

1. Surface area for spherocylindrical particle($2.29 \cdot 10^{-3} m^2$) is much higher than spherical particle ($8.82 \cdot 10^{-5}$) which contribute to more frictional losses in the system for lower volume fractions.

2. For higher volume fractions, elongated particles have a preferred orientation in the shear direction as reported by Reddy et al. [45] and Guo et al. [47]. Once the system reaches quasi-steady state particles are mostly aligned in the shear direction and stay out of the way of each other. This effect reduces the particle interactions.

Total shear stresses are shown in the figure 5.4 which are the sum of streaming and collisional component. Prediction from granular kinetic theory [23] are also included for the volume fraction of 0.4.

By comparing streaming and collisional component trends with total stress, it is clear that collisional effects are much more dominant than kinetic contributions such as $\sigma_t \approx \sigma_c$.

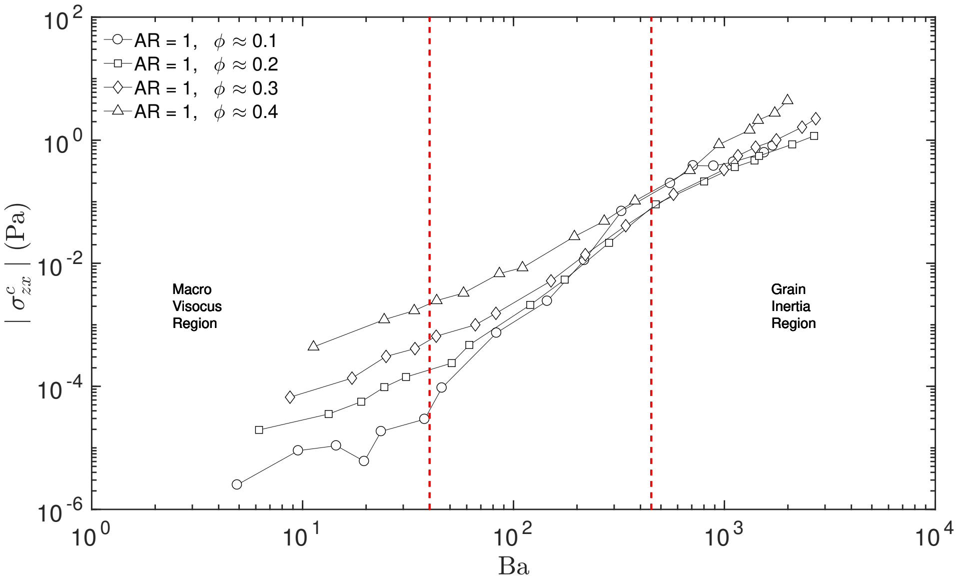

Figure 5.3: Collisional stresses vs Bagnold number.

Streaming stresses have a very low impact on the total stress because of the presence of fluid phase in the system which acts as momentum sink. Due to this fluid phase, particle velocities are much lower than the case of pure granular flows. This is also the reason that kinetic theory predictions are only included for the volume fraction of 0.4 because at higher volume fraction system resembles the granular flows as discussed in section 2.1. Kinetic theory prediction is in-line with the simulation results for spherical particles at higher shear rates.

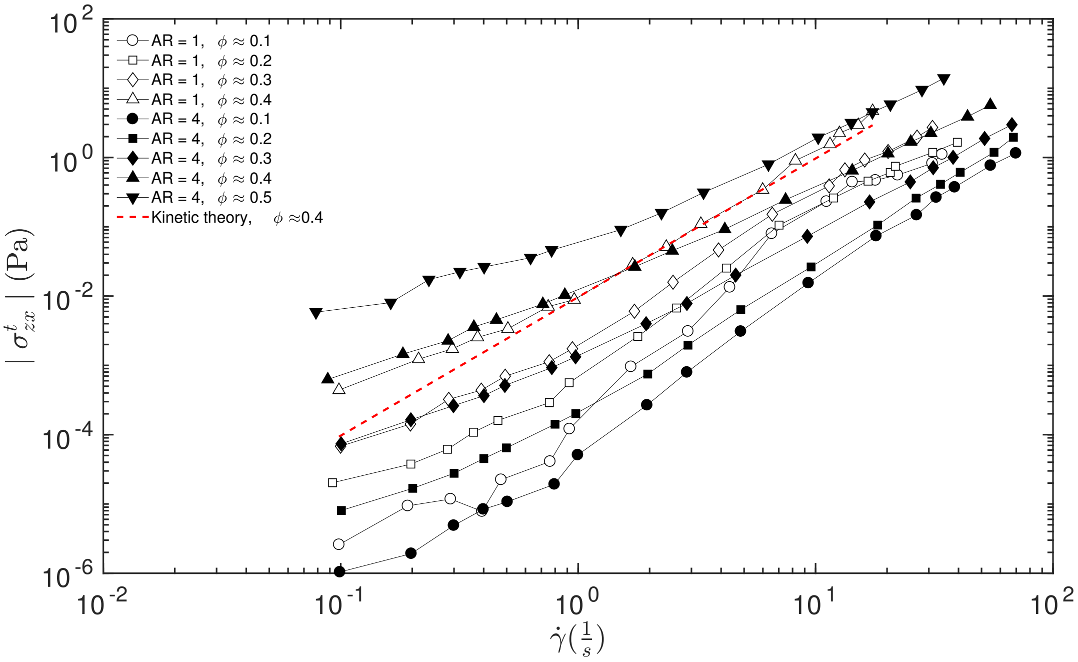

Figure 5.4: Total shear stress as a function of shear rate.

Three distant regimes discussed by Guo et al. [47] for elongated particles do not exist in present system. This is due to the difference in simulated systems. Guo et al. [47] used shear rate of 100/s for their simulations which is significantly higher and they performed simulations for pure granular flows. That is why no comparison has been presented with their results.

Regimes for present study can be identified on the basis of the Doi and Edwards [73] classification. Regime boundaries for spherocylindrical particles are 0.05 and 0.19 in terms of volume fraction. Based on this 0.1 and 0.2 volume fractions in the present study comes under semi-dilute regime while higher volume fractions are in concentrated regime. Doi and Edwards [73] classification is solely based on the Brownian motion of the particles. Also shear rate effect are not taken into the consideration. Total shear stress trends as shown in figure 5.4 for the volume fraction of 0.1 & 0.2 shows a collision dominant system which leads to the conclusion that present system lies in the concentrated regime for all volume fractions.

One can argue that if system lies in collisional regime then the kinetic theory can be used to predict the total stresses. As discussed before the presence of fluid phase requires a two way coupled kinetic theory which should be able to predict momentum exchange between both phases. Although these models are available in the literature for spherical particles [109] usually they are used to solve the particle interactions and no analytical solution is available to compare the results.

Stress tensor symmetry can be calculated by symmetry index as follows:

$$Symmetry\ Index = 2\frac{\mid \sigma_{zx} - \sigma_{xz} \mid}{(\sigma_{zx} + \sigma_{xz})} \tag{5.1}$$

Figure 5.5 shows this index for spherocylindrical particles as a function of shear rate for different volume fractions. spherocylindrical particles shows asymmetrical behaviour (Symmetry index > 5%) for $\phi = 0.1$ & 0.2. Asymmetric behaviour of these particles is due to mean particle angular velocity in the z-direction at lower volume fractions. Particle alignment with shear flow resist the particle motion in z-direction which explains the symmetric behaviour for higher volume fractions. Appendix E shows collisional stress tensor behaviour for $\dot{\gamma} = 0.5/s$.

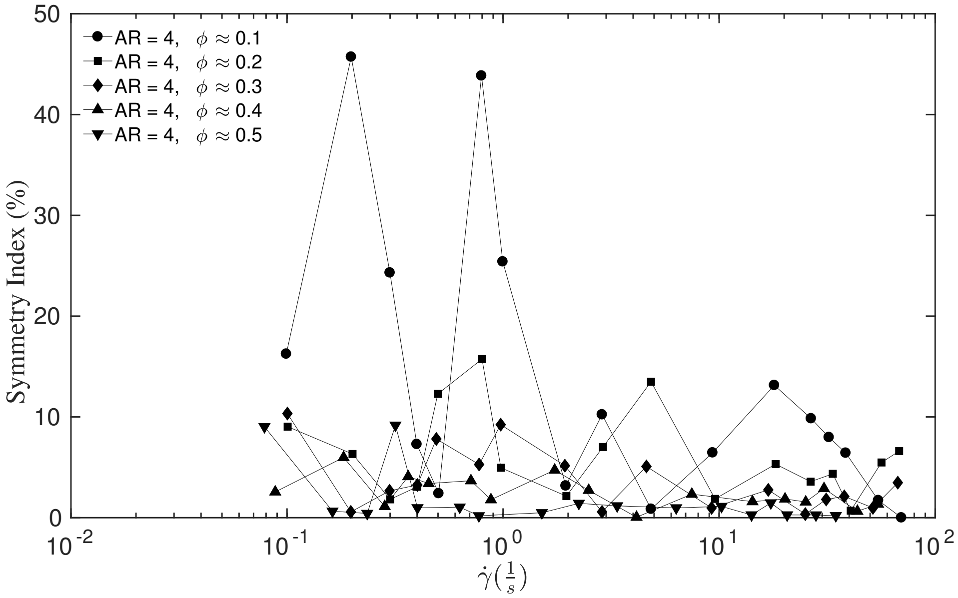

Figure 5.5: Symmetry index as a function of shear rate.

5.2. Granular temperature

Granular temperature is a measurement of residual kinetic energy in the system which governs the motion of the particles. Granular temperature is calculated from velocity fluctuations of the particles in normal direction (equation 3.25).

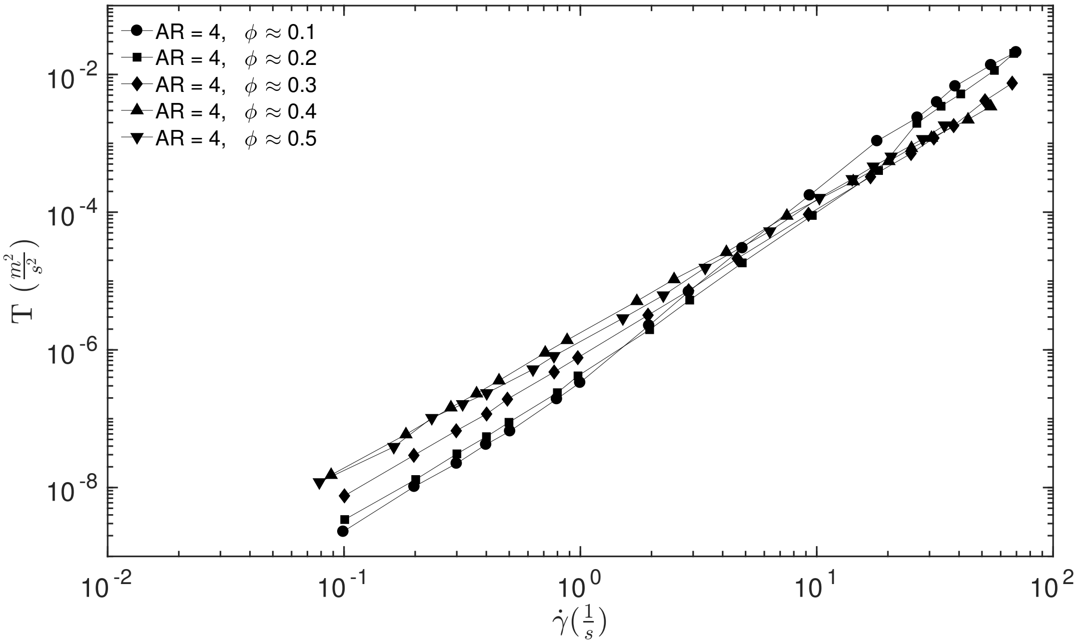

Figure 5.6: Granular temperature as a function of shear rate.

Figure 5.6 shows variation of granular temperature with the shear rate and volume fraction. Granular temperature increases with increasing shear rate which should be the case. It is interesting to notice that for higher shear rate granular temperature is lower for $\phi = 0.4$ & 0.5 than 0.2 and 0.3. Granular temperature is highest for $\phi = 0.1$ at very high shear rates. As discussed in section 5.1 for streaming tensor, at higher volume fractions particle interactions are occurring more frequently. Combined with high shear rate, these interactions result in more energy losses compared to the lower shear rates. These energy losses can be the reason of lower granular temperature for higher volume fractions.

5.3. Particle orientation

5.3.1. Quantitative representation

Figure 5.7 shows the quasi steady state particles orientation ϑ with the shear direction as a function of shear rates for all volume fractions. Shear rate has very little impact on the particle alignment. Once this quasi-steady state is achieved particles have already aligned themselves in the preferred direction. Afterwards particles starts to slide over each other especially for volume fractions higher than 0.3. Volume fraction of the particles plays an important role in this preferred direction. At lower volume fractions, there is more space available for the particles to rotate so particles have random orientation around 45^o. At high volume fractions presence of more particle in the system results in interlocking during transient state. Particle does not have enough space to rotate. That is why as volume fraction is increasing ϑ is decreasing. This phenomena has also been reported by Guo et al. [47],Campbell [46] and Reddy et al. [44]

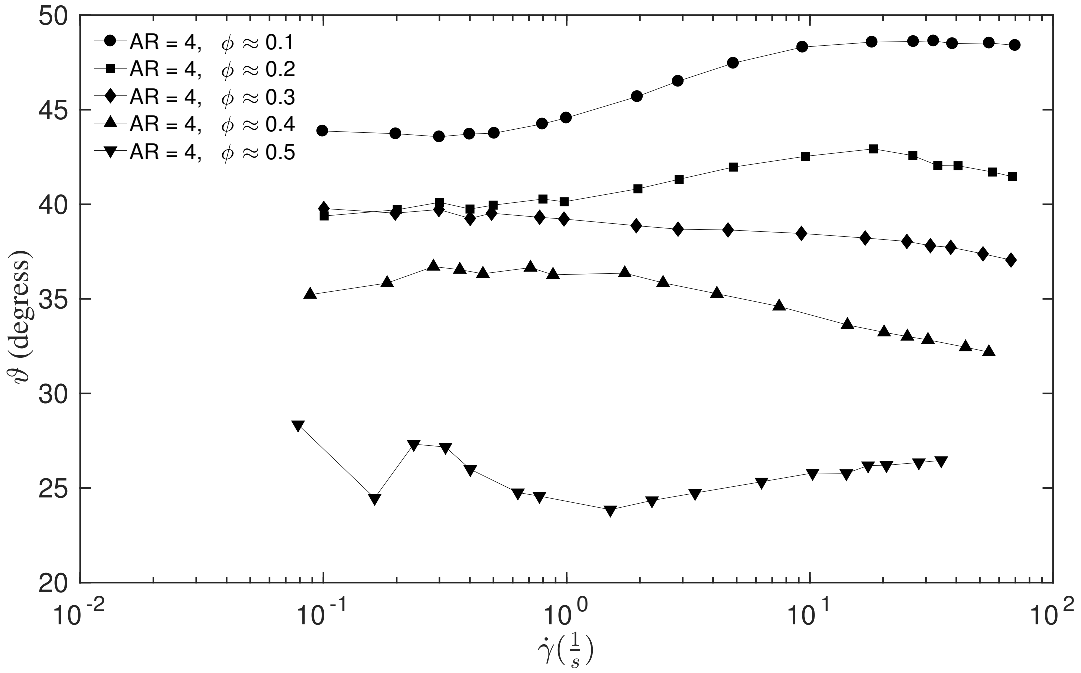

Figure 5.7: Quantitative representation of particle orientation as a function of shear rate.

5.3.2. Qualitative representation

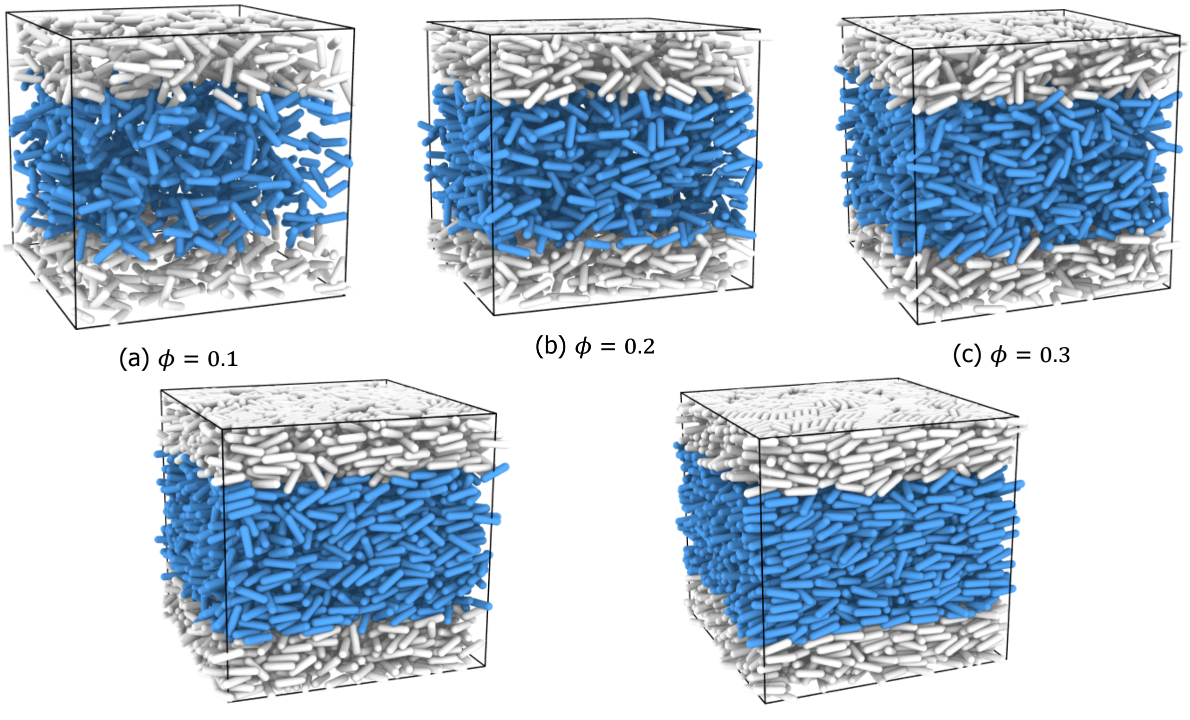

(a) ϕ = 0.1 (b) ϕ = 0.2 (c) ϕ = 0.3 (d) ϕ = 0.4 (e) ϕ = 0.5

Figure 5.8: Snapshot of simulation box for $\dot{\gamma} = 1/s$ at last time step. Blue rods are in the measurement domain.

Figure 5.8 shows snapshot of simulation stat at last time step. It provides a very good visualization of particle alignment but for very large amount of simulations it is not possible to compare snapshots altogether. Super quadratic glyphs as explained in section 4.4.5 are used to visualise and compare particle orientations in 3-D. Figure 5.9 shows these glyphs at different time steps. For ϕ = 0.1 & 0.2

particles shows fairly isotropic behaviour. Particles are equally aligned in all directions. Above $\phi = 0.3$ particles move towards bi-axial alignment. For higher volume fraction particles have aligned themselves in the shear direction which can be visualised in terms of cylindrical glyph from figure 5.9. For almost all volume fractions particle achieve a constant alignment in the first 50 seconds.

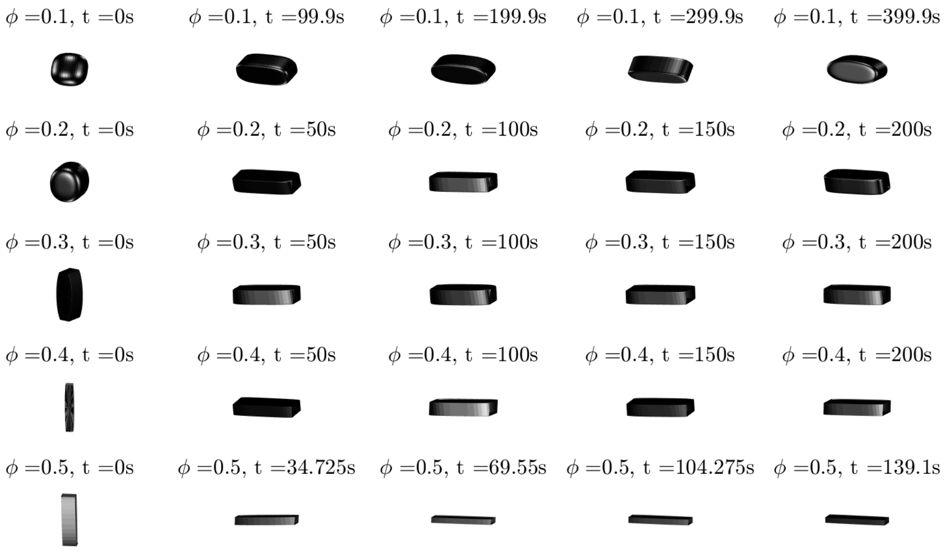

Figure 5.9: Glyph representation of particle orientation for $\dot{\gamma} = 1/s$. 5^{th} column represent the snapshot from figure 5.8.

5.4. Pressure

Pressure in the system is trace of the total stress tensor as shown in the equation 5.2. Pressure on the walls acting as a result of developed stresses can be seen in figure 5.10.

$$P = -\frac{1}{3}\left[\sigma_{xx}^{t} + \sigma_{yy}^{t} + \sigma_{zz}^{t}\right] \tag{5.2}$$

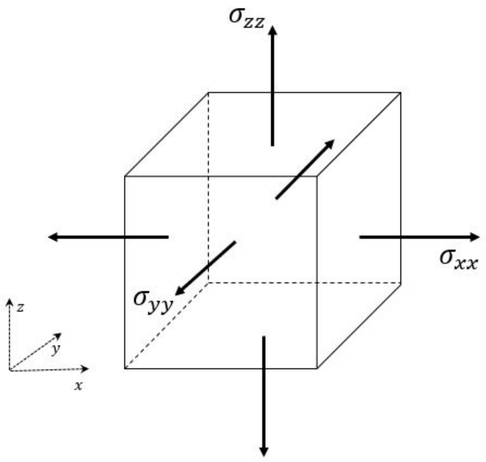

Figure 5.10: Pressure due to normal stress tensor components.

In this study, there is no external pressure applied on the system. So, pressure is an internal property which solely depends on the particle-particle interactions and particle movement. Pressure as a function of shear rate is shown in figure 5.11. Pressure trends show expected behaviour. It is increasing with the shear rate and volume fractions.

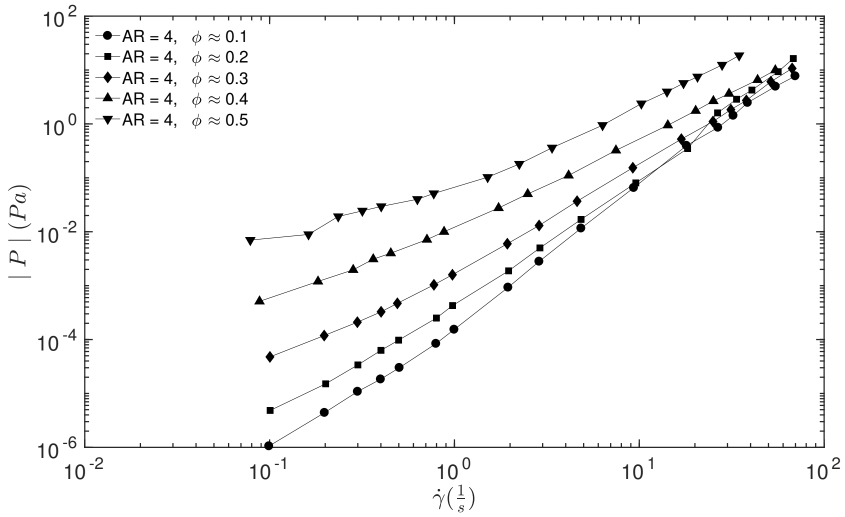

Figure 5.11: Pressure as a function of shear rate for different volume fractions.

$\mu(I)$ rheology as explained in section 2.2 directly relates pressure with shear stress in terms of μ_{eff} which is ratio of shear stress and pressure in the system. μ_{eff} can further be used to form a constitutive relation between shear stress and shear rate. Figure 5.12 shows the μ_{eff} as a function of inertial number (I). Inertial number is the ratio of two times macroscopic deformation ($\tau_{\dot{\gamma}}$) and microscopic rearrangements (τ_P). $\tau_{\dot{\gamma}}$ is the time for one layer of particle to move for one particle diameter (d_p). τ_P is the time for this layer to come back to its original position. In this case inertial number does not vary much for $\phi < 0.5$. This clearly shows that both of these time scales are of same order. MiDi [33] proposed a classification based on Inertial number. For inertial number greater than 0.1 system is totally in collisional regime. Inertial number for present system always remain well above 0.1. This confirms the conclusion made in section 5.1 that kinetic forces are not playing an active role for spherocylindrical rheology under present conditions.

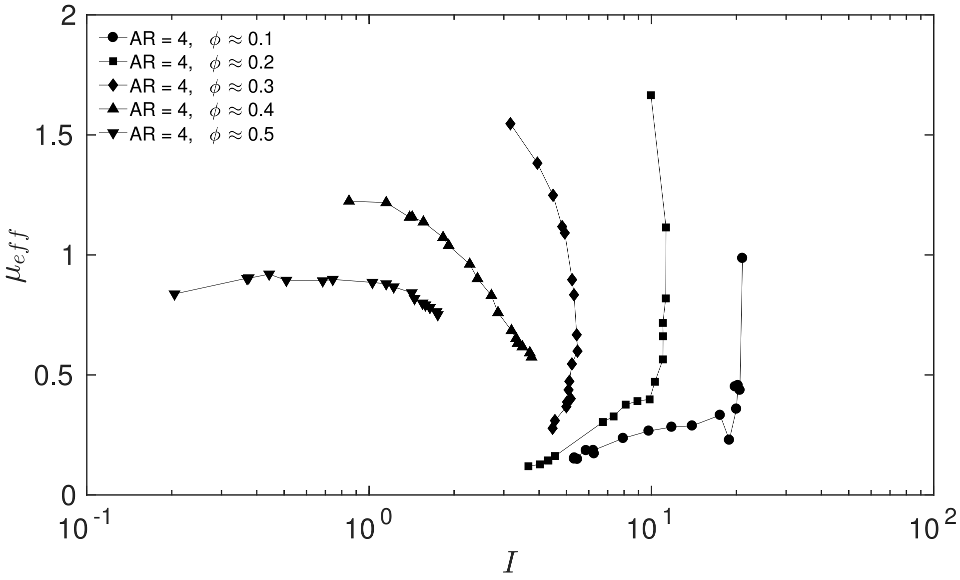

Figure 5.12: $\mu_{eff}(\frac{\sigma^t_{zx}}{|P|})$ as a function of Inertial number ($I = \dot{\gamma} d_p / \sqrt{\frac{P}{\rho_p}}$).

5.5. Normal stress difference

Normal stress difference is the property of the system which can be used to predict non-Newtonian behaviour. For present system normal stress difference are normalized with total pressure of the system to get a better overview.

$$N_1 = \frac{\sigma^t_{xx} - \sigma^t_{zz}}{\mid P \mid} \tag{5.3}$$

$$N_2 = \frac{\sigma^t_{zz} - \sigma^t_{yy}}{\mid P \mid} \tag{5.4}$$

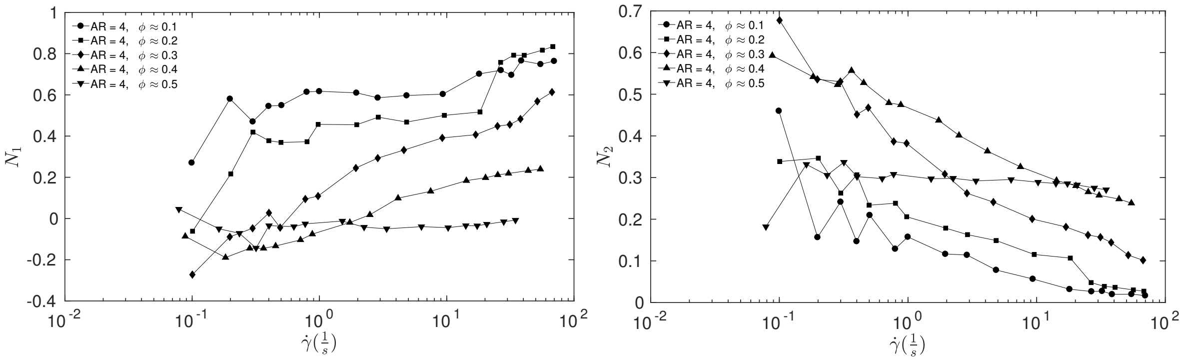

(a) Normalized first normal stress difference

(b) Normalized second normal stress difference

Figure 5.13: Normal stress differences as function of shear rate.

Figure 5.13 shows these differences as function of shear rate. For spherocylindrical particles stress differences are non-zero which was also reported by Somfai et al. [110]. This indicates the non-Newtonian behaviour. Normal stress differences need to be examined really carefully to understand the different regimes and their microscopic origin. Further investigation & discussion on these differences is out of the scope of this study.

5.6. Non-Newtonian behaviour

Figure 5.2 shows collisional stresses on a log-log scale. In figure 5.15 stresses are plotted on a normal scale. For all volume fractions, stress curves show shear thickening behaviour. This behaviour of the spherocylindrical particles is well in line with Stickel and Powell [66] dimensional analysis as shown in figure 5.14.

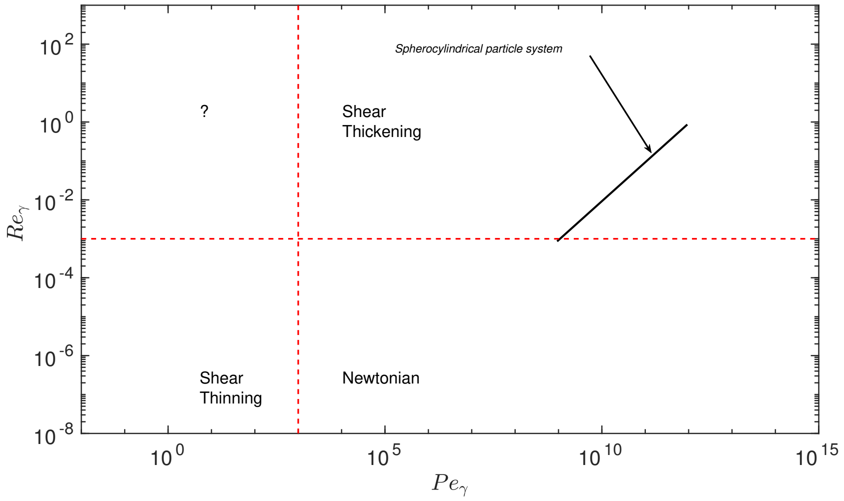

Figure 5.14: Suspension rheology phase plot based on dimensional analysis by Stickel and Powell [66].

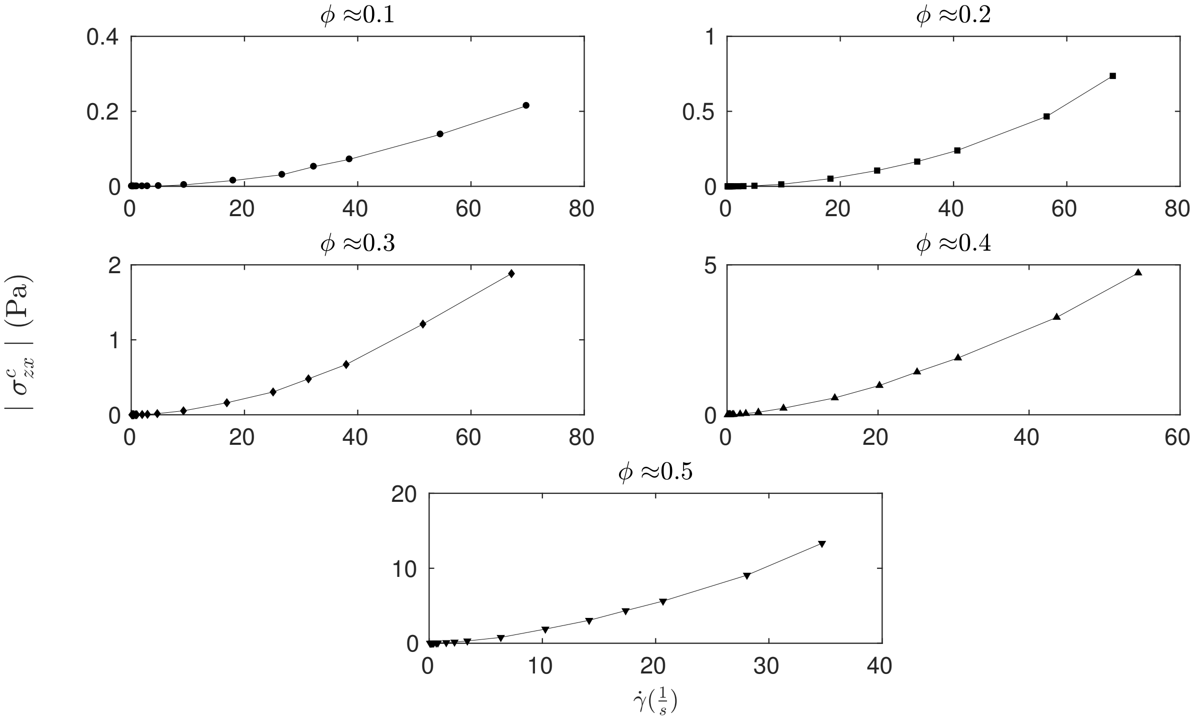

Figure 5.15: Collisional stresses as a function of shear rate on normal scale.

Total shear stresses of the particles are almost equal to collisional contribution as discussed in section 5.1. This suggests that suspension also shows shear thickening behaviour. Shear thickening behaviour can only be explained by considering particle sizes. Particle size used in this study are much higher than in past studies by Mueller et al. [78] and Guo et al. [47]. Mueller et al. [78] have demonstrated shear thinning behaviour via experiments for particle sizes of 100-200μm. They have attributed this behaviour to the localized viscous heating of the fluid. Micromechanics of the system may be the reason behind shear thickening behaviour observed in the present study but very large particle sizes can result in a so-called jamming effect. This effect is caused by collisions between the particles. More collisions will occur with increasing shear rate and comparatively larger particle size require more fluid energy to move the particles which will result in higher viscosity.

5.7. Formulation of stress closure

Hershel-Bulkley model [1] can be used to fit the simulation data for each volume fraction.

$$\sigma = C\dot{\gamma}^m \tag{5.5}$$

C is the consistency which is η_o for newtonian fluid while m is the flow index which defines the non-newtonion behaviour. It is observed that equation 5.5 provides a very poor fit if all data points are treated equally. Based on trial and error a shear rate boundary is identified at $\dot{\gamma} = 1$. This boundary can be used to classify two regimes. Consistency constant(C) and flow index (m) values are shown in figure 5.16 as a function of volume fraction. C values only change between 10-20 % for both regimes. For $\dot{\gamma} > 1$, flow index remains above 1.5 which shows higher dependence on the shear rate. This regime can be classified at total collisional regime analogous to grain inertia regime from Bagnold theory. For $\dot{\gamma} < 1$, shear rate dependence decreases with the volume fraction. This regime can be called a semi collisional regime.

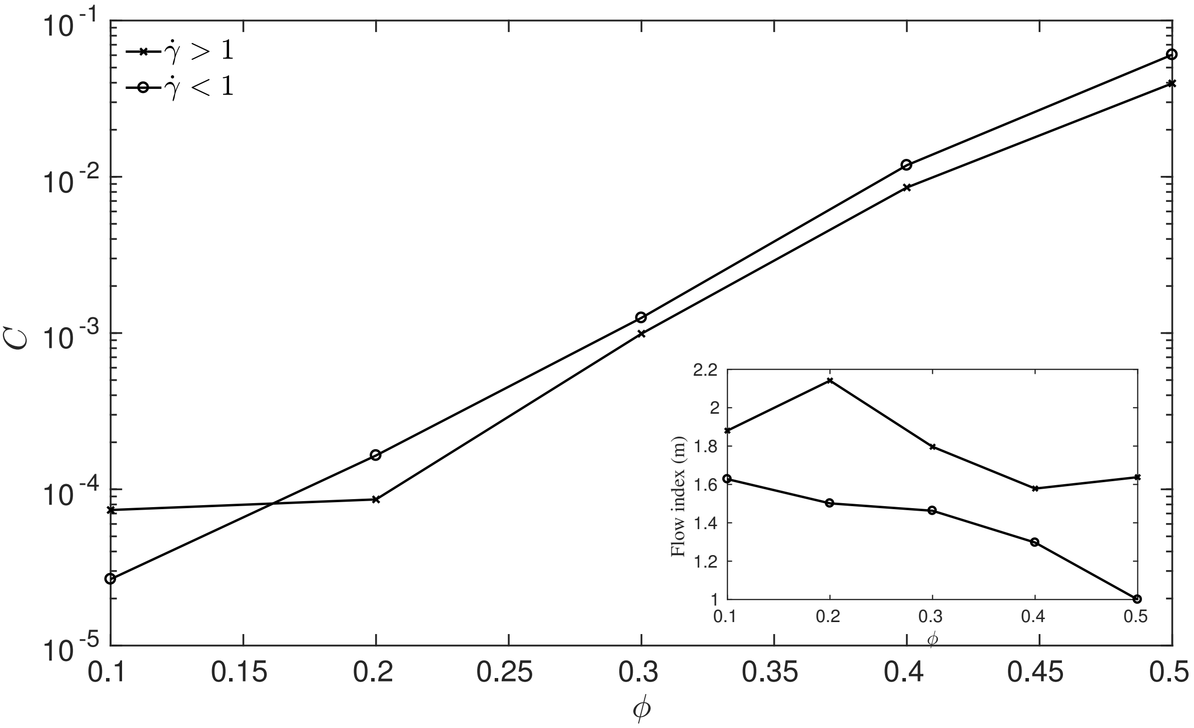

Figure 5.16: Consistency coefficient & flow index as a function of volume fraction.

Consistency coefficient is closely related to apparent viscosity of the suspension. By comparison a new constant, relative consistency $C_r = \frac{C}{\eta_f}$ can be defined. Krieger and Dougherty [64] two parameter model (equation 2.11) is fitted to the relative consistency for both regimes. Fitted parameters are listed in table 5.1. Maximum volume fraction (ϕ_m) value of 0.55 estimated from these fit is very close to the 0.54 reported by Lu et al. [111] for random packing of spherocylindrical particles.

Table 5.1: Best fit parameters for Krieger and Dougherty [64] relationship (equation 2.11) to the data presented in figure 5.16 (Minimum & maximum values are reported in brackets)

	$\dot{\gamma} < 1$	$\dot{\gamma} > 1$
ϕ_m	0.5511 (0.4419,0.6603)	
B	3.131 (3.055,3.208)	2.808 (2.715,2.901)
R^2	0.9929	0.9893

it can be seen from figure 5.16 flow index(m) trends are completely different for both regimes. This makes it really hard to fit the same model equation. A simple equation is proposed to predict the flow index (m) for both regimes:

$$m = \begin{cases} 1.6 - \frac{\phi}{\phi_m} & \text{for } \dot{\gamma} < 1 \\ 2.5 - \frac{\phi}{\phi_m} & \text{for } \dot{\gamma} > 1 \end{cases} \tag{5.6}$$

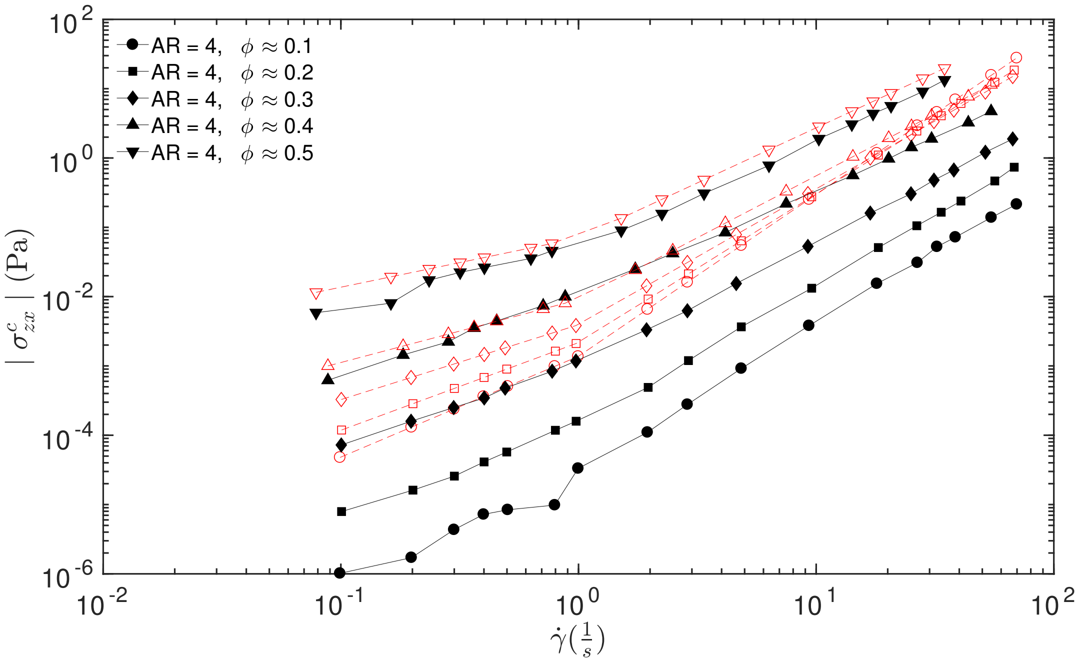

Figure 5.17: Collisional stress prediction from Krieger and Dougherty model. −− represent prediction for respective volume fractions.

Figure 5.17 shows the prediction from proposed Krieger and Dougherty model. This model only predicts the collisional stresses for higher volume fractions. This is due to the fact that for higher volume fractions C_r values are very high and non-least square fitting does not work better with this much variation in the data (Appendix F).

It is obvious from the figure 5.16 that viscosity increases exponentially with the volume fraction. Equation 2.13 can be used to capture this trend. Although C_r values are different for both regimes, Values of A and k do not vary significantly as shown in table 5.2. Instead of using two different set of A and k values for both regimes it is proposed to use average values to form a one constitutive equation of C_r.

Table 5.2: Best fit parameters for Broughton and Squires [2] relationship (equation 2.13) to the data presented in figure 5.16 (Minimum & maximum values are reported in brackets)

	$\dot{\gamma} < 1$	$\dot{\gamma} > 1$
A	-5.646 (-6.193, -5.1)	-5 (-7.241, -2.76)
k	10.88 (9.966, 11.78)	9.463 (5.74, 13.19)
R^2	0.9979	0.9562

$$ln(C_r) = -5.323 + 10.1715\frac{\phi}{\phi_m} \tag{5.7}$$

Equation 5.7 is a modified form of equation 2.13 to incorporate maximum volume fraction of the system. Figure 5.18 shows the prediction from modified Broughton and Squires [2] model. Equations 5.7, 5.6 and 5.5 are used to calculate consistency, flow index and collisional stresses respectively.

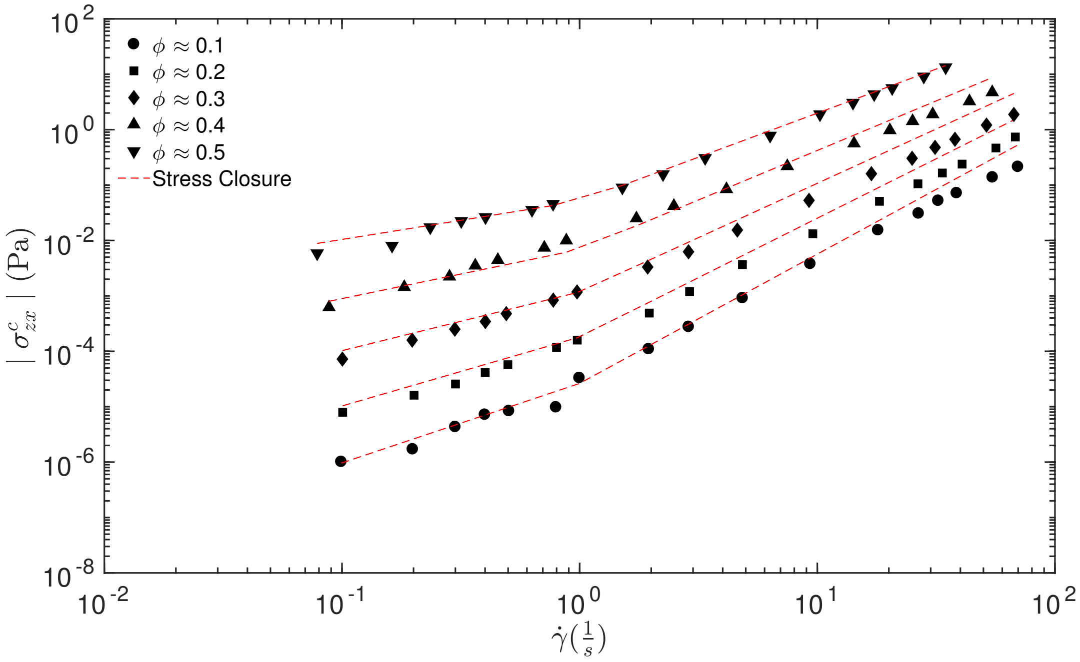

Figure 5.18: Collisional stress prediction from Broughton model. −− represent prediction for respective volume fractions.

Parameters A and k obtained from this data fitting are very close to B_1 and B_2 from equation 2.10. This is really interesting because this shows some relationship between spherical and non-spherical particle rheology.

Stress closure proposed in this study is a unique stress closure because it is only applicable to spherocylindrical particles of aspect ratio 4. Still, it is expected that it will be valid for all kind of suspensions whether it is low viscous system or high viscous. Granular temperature and particle alignment are not incorporated in this stress closure. May be equation 5.7 parameters A and k does have dependency on the granular temperature and particle alignment which needs to be determined separately.

6

Conclusions

In this study, rheological behaviour of spherocylindrical particles has been investigated via CFD-DEM coupled simulations. Plane shear flow without gravity has been considered for the simulations. Particles are subjected to different shear rates ranging from 0.1 to 100/s for different volume fractions.

A comparison has been made for spherical and spherocylindrical particles in terms of the stress tensor. It is shown that spherocylindrical particles experience less total shear stresses than spherical particles. This is due to the preferred particle alignment in the shear direction, especially at high volume fractions. At lower volume fractions surface area of the particles plays an important role. Higher surface area of spherocylindrical particles results in more collisions. This causes the particles to lose more energy than spherical particles which is the reason behind lower shear stresses at lower volume fractions.

For gas viscosity of $1 \cdot 10^{-3} (Pa.s)$ streaming shear stresses are very low and collisional stresses govern the behaviour of the spherocylindrical particle suspension because the fluid present in the system acts as a momentum sink. Particles lose their kinetic energy rapidly in this suspension which reduces the streaming stresses. Only collisional or concentrated regime exists for this highly viscous suspension. Following separate observations have also been made for the spherocylindrical particle suspension.

- It is observed that Stress tensor is symmetric for $\phi > 0.2$. At lower volume fractions asymmetric behaviour is attributed to the particle angular velocity in the z-direction. For higher volume fractions this angular moment is restricted due to the preferred alignment of the particles which results in symmetric stress tensor.
- Shear rate has little effect on the particle alignment. For lower volume fractions ($\phi < 0.3$) particles mostly remain at 45^o with the shear direction. This angle decreases to 25^o for $\phi = 0.5$. Preferred alignment at higher volume fractions is caused by systems tendency to lower its free energy. This alignment reduces the chances of collisions between particles and system reaches a state where it has the lowest energy dissipation rate.
- The granular temperature for higher volume fractions is lower than lower volume fraction at high shear rates. This is due to the fact that collision time between particles decreases rapidly for higher volume fractions. These particle collisions result in very low-velocity fluctuations.

Spherocylindrical particles of aspect ratio four show shear thickening behaviour. Viscosity of the particles depends highly on the volume fraction. Shear thickening behaviour can be caused by jamming of the particles due to very high equivalent diameter. More collisions will start to occur with increasing shear rate. These collisions will resist the particle movement in the suspension which will require more energy by the fluid to move these particles in the shear direction. Power law curve is fitted to capture this shear thickening behaviour. It is observed that one curve cannot define the behaviour of the particles. So, a shear rate boundary of 1/s is defined to classify the system in semi-collisional and total collisional regime. For the total collisional regime, the system shows higher dependence on the shear rate ($\dot{\gamma}^2$). For semi collisional regime this dependence is of the O(1.5). Broughton and Squires [2] model has been used to find out consistency coefficient. Combined with very simple flow index model, stress closure proposed in this study provides a very good fit for the simulation data.

7

Recommendations

For viscosity of $1 \cdot 10^{-5}$, there is a high chance that streaming contribution will come into play which is not the case for this study. It is advised to perform the same simulations for lower viscous suspensions. These simulations will also help to find out if stress closure proposed in this study is equally valid for all kind of suspensions of aspect ratio four.

It would be interesting to find out the stress tensor dependence on the aspect ratio of the particles. Such simulation could reveal exactly at what aspect ratio spherocylindrical particle behaviour starts to deviate from the spherical particles. Moreover, the result of these simulations can be extended to find out a generic stress closure in terms of particle aspect ratio.

In this study, the effect of granular temperature and particle orientation has not been explored. Granular temperature can be used to control the simulation behaviour by varying damping constant (ζ). Similarly, overall particle orientation can be controlled by applying Maier-Saupe potential [112]. Both of these parameters are expected to have strong influence on the system rheology. These controlled simulations will help to improve the stress closure in terms of particle alignment and granular temperature.

Nomenclature

Greek Symbols

Symbol	Description	Units
β	Di Felice exponent	-
ν	Kinematic viscosity	$\mathrm{m^2/s}$
ω	Angular velocity	deg/s
τ	Torque	Nm
ϑ	Angle between particle and shear direction	deg
ζ	Damping coefficient	Kg/s
$\dot{\gamma}$	Shear rate	1/s
μ	Friction Coefficient	-
ϕ	Volume fraction	-
ρ	density	$\mathrm{Kg/m^3}$
σ	Stress	Pa
t	time	s
η	Coefficient of viscosity	Pa s

Roman Symbols

Symbol	Description	Units
ΔP	Pressure difference	Pa
A	Area	m^2
a	Acceleration	$\mathrm{m/s^2}$
C_D	Drag coefficient	-
d	Diameter	m
F	Force	N
g_0	Radial distribution function	-
I	Inertial Number	-
I^m	Moment of inertia	$\mathrm{kg/m^2}$
k	Spring coefficient	N/m
n	Direction vector	-
P	Pressure	Pa

Q	Quaternion	-
R	Radius	m
RM	Rotational matrix	-
S	Momentum exchange	$\frac{kg}{m^2s^2}$
U	Rod unit vector	-
u	Gas velocity	m/s
$\dot{W}$	Work	J
e	Coefficient of restitution	-
L	Length	m
M	Mass	kg
N	Number of particles	-
V	Volume	m^3

Subscripts & Superscripts

$\perp$	Perpendicular
$\parallel$	Parallel
cb	Control Box
$cell$	CFD cell
ct	Contact
eff	Effective
ext	External
g	Gas
int	Interaction
p	Particle
r	Relative
$roll$	Rolling friction
s	Streaming
a	Apparent
c	Collisional
m	maximum
o	Newtonian fluid
f	Fluid
v	Viscous

Bibliography

[1] WH Herschel and R Bulkley. Measurement of consistency as applied to rubber-benzene solutions. In *Am. Soc. Test Proc*, volume 26, pages 621–633, 1926.

[2] Geoffrey Broughton and Lombard Squires. The viscosity of oil-water emulsions1. *The Journal of Physical Chemistry*, 42(2):253–263, 1938.

[3] Prabir Basu. *Combustion and gasification in fluidized beds*. CRC press, 2006.

[4] Clayton T Crowe. *Multiphase flow handbook*, volume 59. CRC press, 2005.

[5] Vineet Singh Sikarwar, Ming Zhao, Peter Clough, Joseph Yao, Xia Zhong, Mohammad Zaki Memon, Nilay Shah, Edward J Anthony, and Paul S Fennell. An overview of advances in biomass gasification. *Energy & Environmental Science*, 9(10):2939–2977, 2016.

[6] H Kruggel-Emden and K Vollmari. Flow-regime transitions in fluidized beds of non-spherical particles. *Particuology*, 29:1–15, 2016.

[7] Rory LC Flemmer, James Pickett, and Nigel N Clark. An experimental study on the effect of particle shape on fluidization behavior. *Powder Technology*, 77(2):123–133, 1993.

[8] Baiqian Liu, Xiaohui Zhang, Ligang Wang, and Hui Hong. Fluidization of non-spherical particles: sphericity, zingg factor and other fluidization parameters. *Particuology*, 6(2):125–129, 2008.

[9] MJ Andrews and PJ O'rourke. The multiphase particle-in-cell (mp-pic) method for dense particulate flows. *International Journal of Multiphase Flow*, 22(2):379–402, 1996.

[10] Madhava Syamlal, William Rogers, and Thomas J OBrien. Mfix documentation theory guide. Technical report, USDOE Morgantown Energy Technology Center, WV (United States), 1993.

[11] Andreas Hölzer and Martin Sommerfeld. New simple correlation formula for the drag coefficient of non-spherical particles. *Powder Technology*, 184(3):361–365, 2008.

[12] Albert Einstein. A new determination of molecular dimensions. *Ann. Phys*, 19(2):289–306, 1906.

[13] Eugene Cook Bingham. *The History of the Society of Rheology from 1924-1944*. 1944.

[14] Charles S Campbell. Rapid granular flows. *Annual Review of Fluid Mechanics*, 22(1):57–90, 1990.

[15] Charles S Campbell. The stress tensor for simple shear flows of a granular material. *Journal of Fluid Mechanics*, 203:449–473, 1989.

[16] ODL Stark and PA Cundall. A discrete numerical mode for granular assemblies. *Geotechnique*, 291:47–65, 1979.

[17] Charles S Campbell and Ailing Gong. The stress tensor in a two-dimensional granular shear flow. *Journal of Fluid Mechanics*, 164:107–125, 1986.

[18] NG Deen, M Van Sint Annaland, MA Van der Hoef, and JAM Kuipers. Review of discrete particle modeling of fluidized beds. *Chemical engineering science*, 62(1):28–44, 2007.

[19] AA Mahmood and M Elektorowicz. A review of discrete element method research on particulate systems. In *IOP Conference Series: Materials Science and Engineering*, volume 136, page 012034. IOP Publishing, 2016.

[20] S Ogawa. Multitemperature theory of granular materials. In *Proc. of the US-Japan Seminar on Continuum Mechanical and Statistical Approaches in the Mechanics of Granular Materials, 1978*, pages 208–217. Gakajutsu Bunken Fukyu-Kai, 1978.

[21] Sydney Chapman and Thomas George Cowling. *The mathematical theory of non-uniform gases: an account of the kinetic theory of viscosity, thermal conduction and diffusion in gases*. Cambridge university press, 1970.

[22] James T Jenkins and Stuart B Savage. A theory for the rapid flow of identical, smooth, nearly elastic, spherical particles. *Journal of fluid mechanics*, 130:187–202, 1983.

[23] CKK Lun, S Br Savage, DJ Jeffrey, and N Chepurniy. Kinetic theories for granular flow: inelastic particles in couette flow and slightly inelastic particles in a general flowfield. *Journal of fluid mechanics*, 140:223–256, 1984.

[24] Norman F Carnahan and Kenneth E Starling. Equation of state for nonattracting rigid spheres. *The Journal of Chemical Physics*, 51(2):635–636, 1969.

[25] i JT Jenkins and Mark W Richman. Plane simple shear of smooth inelastic circular disks: the anisotropy of the second moment in the dilute and dense limits. *Journal of Fluid Mechanics*, 192:313–328, 1988.

[26] Alexander Goldshtein and Michael Shapiro. Mechanics of collisional motion of granular materials. part 1. general hydrodynamic equations. *Journal of Fluid Mechanics*, 282:75–114, 1995.

[27] James T Jenkins and Chao Zhang. Kinetic theory for identical, frictional, nearly elastic spheres. *Physics of Fluids*, 14(3):1228–1235, 2002.

[28] Charles S Campbell. Granular shear flows at the elastic limit. *Journal of fluid mechanics*, 465: 261–291, 2002.

[29] James T Jenkins. Dense shearing flows of inelastic disks. *Physics of Fluids*, 18(10):103307, 2006.

[30] D Berzi, CG Di Prisco, and D Vescovi. Constitutive relations for steady, dense granular flows. *Physical Review E*, 84(3):031301, 2011.

[31] Charles S Campbell. Stress-controlled elastic granular shear flows. *Journal of Fluid Mechanics*, 539:273–297, 2005.

[32] Charles S Campbell. Granular material flows–an overview. *Powder Technology*, 162(3):208–229, 2006.

[33] GDR MiDi. On dense granular flows. *European Physical Journal E–Soft Matter*, 14(4), 2004.

[34] Yoël Forterre and Olivier Pouliquen. Flows of dense granular media. *Annu. Rev. Fluid Mech.*, 40: 1–24, 2008.

[35] Pierre Jop, Yoël Forterre, and Olivier Pouliquen. A constitutive law for dense granular flows. *Nature*, 441(7094):727–730, 2006.

[36] Frédéric Da Cruz, Sacha Emam, Michaël Prochnow, Jean-Noël Roux, and François Chevoir. Rheophysics of dense granular materials: Discrete simulation of plane shear flows. *Physical Review E*, 72(2):021309, 2005.

[37] Takahiro Hatano. Power-law friction in closely packed granular materials. *Physical Review E*, 75 (6):060301, 2007.

[38] Abdoulaye Fall, Guillaume Ovarlez, David Hautemayou, Cédric Mézière, J-N Roux, and François Chevoir. Dry granular flows: Rheological measurements of the μ (i)-rheology. *Journal of rheology*, 59(4):1065–1080, 2015.

[39] Pierre Jop, Yoël Forterre, and Olivier Pouliquen. Crucial role of sidewalls in granular surface flows: consequences for the rheology. *Journal of Fluid Mechanics*, 541:167–192, 2005.

[40] JIN Baosheng, TAO He, and Wenqi Zhong. Flow behaviors of non-spherical granules in rectangular hopper. *Chinese Journal of Chemical Engineering*, 18(6):931–939, 2010.

[41] Jintang Li, Paul A Langston, Colin Webb, and Tom Dyakowski. Flow of sphero-disc particles in rectangular hoppers—a dem and experimental comparison in 3d. *Chemical Engineering Science*, 59(24):5917–5929, 2004.

[42] AA Pena, R Garcia-Rojo, and Hans Jürgen Herrmann. Influence of particle shape on sheared dense granular media. *Granular matter*, 9(3-4):279–291, 2007.

[43] Paul W Cleary and Mark L Sawley. Dem modelling of industrial granular flows: 3d case studies and the effect of particle shape on hopper discharge. *Applied Mathematical Modelling*, 26(2): 89–111, 2002.

[44] K Anki Reddy, V Kumaran, and J Talbot. Orientational ordering in sheared inelastic dumbbells. *Physical Review E*, 80(3):031304, 2009.

[45] K Anki Reddy, J Talbot, and V Kumaran. Dynamics of sheared inelastic dumbbells. *Journal of Fluid Mechanics*, 660:475–498, 2010.

[46] Charles S Campbell. Elastic granular flows of ellipsoidal particles. *Physics of Fluids*, 23(1): 013306, 2011.

[47] Yu Guo, C Wassgren, W Ketterhagen, B Hancock, B James, and J Curtis. A numerical study of granular shear flows of rod-like particles using the discrete element method. *Journal of fluid Mechanics*, 713:1–26, 2012.

[48] Dániel B Nagy, Philippe Claudin, Tamás Börzsönyi, and Ellák Somfai. Rheology of dense granular flows for elongated particles. *Physical Review E*, 96(6):062903, 2017.

[49] Ralph A Bagnold. Experiments on a gravity-free dispersion of large solid spheres in a newtonian fluid under shear. In *Proceedings of the Royal Society of London A: Mathematical, Physical and Engineering Sciences*, volume 225, pages 49–63. The Royal Society, 1954.

[50] DF McTigue. A model for stresses in shear flow of granular material. *Proc. US-Japan Sem. on Cont.-Mech. and Stat. Approaches to Mech. Granular Mater*, pages 266–271, 1978.

[51] Ken-Ichi Kanatani. A micropolar continuum theory for the flow of granular materials. *International Journal of Engineering Science*, 17(4):419–432, 1979.

[52] SB Savage and DJ Jeffrey. The stress tensor in a granular flow at high shear rates. *Journal of Fluid Mechanics*, 110:255–272, 1981.

[53] ML Hunt, R Zenit, CS Campbell, and CE Brennen. Revisiting the 1954 suspension experiments of ra bagnold. *Journal of Fluid Mechanics*, 452:1–24, 2002.

[54] Ir R Rutgers. Relative viscosity of suspensions of rigid spheres in newtonian liquids. *Rheologica Acta*, 2(3):202–210, 1962.

[55] Ir R Rutgers. Relative viscosity and concentration. *Rheologica Acta*, 2(4):305–348, 1962.

[56] David G Thomas. Transport characteristics of suspension: Viii. a note on the viscosity of newtonian suspensions of uniform spherical particles. *Journal of Colloid Science*, 20(3):267–277, 1965.

[57] Albert Einstein. Eine neue bestimmung der moleküldimensionen. *Annalen der Physik*, 324(2): 289–306, 1906.

[58] John Happel. Viscosity of suspensions of uniform spheres. *Journal of Applied Physics*, 28(11): 1288–1292, 1957.

[59] Duncan James Jeffrey and Andreas Acrivos. The rheological properties of suspensions of rigid particles. *AIChE Journal*, 22(3):417–432, 1976.

[60] Willi Pabst, Eva Gregorová, and Christoph Berthold. Particle shape and suspension rheology of short-fiber systems. *Journal of the European Ceramic Society*, 26(1):149–160, 2006.

[61] Eugene Guth and O Gold. On the hydrodynamical theory of the viscosity of suspensions. *Phys. Rev*, 53(322):2–15, 1938.

[62] R St J Manley and SG Mason. Particle motions in sheared suspensions iii.: Further observations on collisions of spheres. *Canadian Journal of Chemistry*, 33(5):763–773, 1955.

[63] GK Batchelor. The effect of brownian motion on the bulk stress in a suspension of spherical particles. *Journal of fluid mechanics*, 83(1):97–117, 1977.

[64] Irvin M Krieger and Thomas J Dougherty. A mechanism for non-newtonian flow in suspensions of rigid spheres. *Transactions of the Society of Rheology*, 3(1):137–152, 1959.

[65] EG Richardson. Über die viskosität von emulsionen. *Kolloid-Zeitschrift*, 65(1):32–37, 1933.

[66] Jonathan J Stickel and Robert L Powell. Fluid mechanics and rheology of dense suspensions. *Annu. Rev. Fluid Mech.*, 37:129–149, 2005.

[67] George B Jeffery. The motion of ellipsoidal particles immersed in a viscous fluid. In *Proceedings of the royal society of London A: Mathematical, physical and engineering sciences*, volume 102, pages 161–179. The Royal Society, 1922.

[68] Josef Ježek, Stanislav Saic, Karel Segeth, and Karel Schulmann. Three-dimensional hydrodynamical modelling of viscous flow around a rotating ellipsoidal inclusion. *Computers & Geosciences*, 25(5):547–558, 1999.

[69] Dazhi Jiang. Numerical modeling of the motion of rigid ellipsoidal objects in slow viscous flows: a new approach. *Journal of Structural Geology*, 29(2):189–200, 2007.

[70] HL Goldsmith and SG Mason. Particle motions in sheared suspensions xiii. the spin and rotation of disks. *Journal of Fluid Mechanics*, 12(1):88–96, 1962.

[71] E. Anczurowski and S. G. Mason. Particle motions in sheared suspensions. xxiv. rotation of rigid spheroids and cylinders. *Transactions of the Society of Rheology*, 12(2):209–215, 1968.

[72] Howard Brenner. Rheology of a dilute suspension of axisymmetric brownian particles. *International Journal of Multiphase Flow*, 1(2):195–341, 1974.

[73] Mand Doi and SF Edwards. Dynamics of rod-like macromolecules in concentrated solution. part 1. *Journal of the Chemical Society, Faraday Transactions 2: Molecular and Chemical Physics*, 74: 560–570, 1978.

[74] Mason Anczurow. Kinetics of flowing dispersions. 3. equilibrium orientations of rods and discs (experimental). *JOURNAL OF COLLOID AND INTERFACE SCIENCE*, 23:533–546, 1967.

[75] Carl A Stover, Donald L Koch, and Claude Cohen. Observations of fibre orientation in simple shear flow of semi-dilute suspensions. *Journal of Fluid Mechanics*, 238:277–296, 1992.

[76] Robert L Powell. Rheology of suspensions of rodlike particles. *Journal of statistical physics*, 62 (5):1073–1094, 1991.

[77] Mina Djalili-Moghaddam and Staffan Toll. Fibre suspension rheology: effect of concentration, aspect ratio and fibre size. *Rheologica acta*, 45(3):315–320, 2006.

[78] S Mueller, EW Llewellin, and HM Mader. The rheology of suspensions of solid particles. In *Proceedings of the Royal Society of London A: Mathematical, Physical and Engineering Sciences*, page rspa20090445. The Royal Society, 2009.

[79] Christoph Kloss, Christoph Goniva, Alice Hager, Stefan Amberger, and Stefan $LIGGGHTS^{®}$ Pirker. Models, algorithms and validation for opensource dem and cfd–dem. *Progress in Computational Fluid Dynamics, an International Journal*, 12(2-3):140–152, 2012.

[80] openFoam. https://www.openfoam.com/, 2018.

[81] Christoph Goniva, Christoph Kloss, Niels G. Deen, Johannes A M Kuipers, and Stefan Pirker. Influence of rolling friction on single spout fluidized bed simulation. *Particuology*, 10(5):582–591, 2012. ISSN 16742001. doi: 10.1016/j.partic.2012.05.002.

[82] BJ Alder and TEf Wainwright. Phase transition for a hard sphere system. *The Journal of chemical physics*, 27(5):1208–1209, 1957.

[83] Charles S Campbell and Christopher E Brennen. Computer simulation of granular shear flows. *Journal of Fluid Mechanics*, 151:167–188, 1985.

[84] MJV Goldschmidt, JAM Kuipers, and WPM Van Swaaij. Hydrodynamic modelling of dense gas-fluidised beds using the kinetic theory of granular flow: effect of coefficient of restitution on bed dynamics. *Chemical Engineering Science*, 56(2):571–578, 2001.

[85] Haosheng Zhou, Gilles Flamant, and Daniel Gauthier. Dem-les of coal combustion in a bubbling fluidized bed. part i: gas-particle turbulent flow structure. *Chemical engineering science*, 59 (20):4193–4203, 2004.

[86] BH Xu and AB Yu. Numerical simulation of the gas-solid flow in a fluidized bed by combining discrete particle method with computational fluid dynamics. *Chemical Engineering Science*, 52 (16):2785–2809, 1997.

[87] Masayuki Horio, Yuki Iwadate, and Tomoki Sugaya. Particle normal stress distribution around a rising bubble in a fluidized bed. *Powder technology*, 96(2):148–157, 1998.

[88] H Zhou, G Flamant, D Gauthier, and Y Flitris. Simulation of coal combustion in a bubbling fluidized bed by distinct element method. *Chemical Engineering Research and Design*, 81(9):1144–1149, 2003.

[89] HP Zhu, ZY Zhou, RY Yang, and AB Yu. Discrete particle simulation of particulate systems: theoretical developments. *Chemical Engineering Science*, 62(13):3378–3396, 2007.

[90] Daan Frenkel, Berend Smit, Jan Tobochnik, Susan R McKay, Wolfgang Christian, et al. Understanding molecular simulation. *Computers in Physics*, 11(4):351–354, 1997.

[91] Wilfred F van Gunsteren and Herman JC Berendsen. Computer simulation of molecular dynamics: Methodology, applications, and perspectives in chemistry. *Angewandte Chemie International Edition*, 29(9):992–1023, 1990.

[92] Carlos Vega and Santiagg Lago. a Fast Algorithm To Evaluate the Shortest Distance Between Rods. *Cumputen Chem*, 18(1):55–59, 1994.

[93] L. Pournin, M. Weber, M. Tsukahara, J. A. Ferrez, M. Ramaioli, and Th M. Liebling. Three-dimensional distinct element simulation of spherocylinder crystallization. *Granular Matter*, 7 (2-3):119–126, 2005. ISSN 14345021. doi: 10.1007/s10035-004-0188-4.

[94] C M Wensrich and A Katterfeld. Rolling friction as a technique for modelling particle shape in DEM. *Powder Technology*, 217:409–417, 2012. ISSN 0032-5910. doi: 10.1016/j.powtec.2011.10.057.

[95] Doru Constatin. Mass moment of inertia of a spherocylinder, 2014.

[96] T.M.J. (Tim) Nijssen. Experiments and modelling of non-spherical particle fluidization: An experimental and numerical study on the behaviour of spherocylindrical particles in pseudo-2d uidized beds. Master's thesis, Eindhoven University of Technology, Netherlands, 2017.

[97] H.K: Versteeg and W. Malalasekera. An Introduction to Computational Fluid Dynamics - The Finite Volume Method, 1995. ISSN 02104806.

[98] Z. Y. Zhou, D. Pinson, R. P. Zou, and A. B. Yu. Discrete particle simulation of gas fluidization of ellipsoidal particles. *Chemical Engineering Science*, 66(23):6128–6145, 2011. ISSN 00092509.

[99] Marian Zastawny, George Mallouppas, Fan Zhao, and Berend van Wachem. Derivation of drag and lift force and torque coefficients for non-spherical particles in flows. *International Journal of Multiphase Flow*, 39:227–239, 2012.

[100] Ivan Mema, Vinay V. Mahajan, Barry W. Fitzgerald, Hans Kuipers, and Johan T. Padding. Effect of lift force on dense gas-fluidized beds of non-spherical particles. In *12th Internatial Conference on CFD in Oil & Gas, Metallurgical and Process Industries*, 2017.

[101] S.K. Pacha Sanjeevi. Internal communication. 2017.

[102] R. Di Felice. The voidage function for fluid-particle interaction systems. *International Journal of Multiphase Flow*, 20(I):153–159, 1994.

[103] Dimitri Gidaspow. *Multiphase flow and fluidization: continuum and kinetic theory descriptions*. Academic press, 1994.

[104] S. Ergun. Fluid flow through packed columns. *Chem. Eng. Prog.*, 48:89–94, 1952.

[105] S Luding, M Lätzel, W Volk, S Diebels, and HJ Herrmann. From discrete element simulations to a continuum model. *Computer methods in applied mechanics and engineering*, 191(1):21–28, 2001.

[106] AW Lees and SF Edwards. The computer study of transport processes under extreme conditions. *Journal of Physics C: Solid State Physics*, 5(15):1921, 1972.

[107] Abraham Savitzky and Marcel JE Golay. Smoothing and differentiation of data by simplified least squares procedures. *Analytical chemistry*, 36(8):1627–1639, 1964.

[108] Gordon Kindlmann. Superquadric tensor glyphs. In *Proceedings of the Sixth Joint Eurographics-IEEE TCVG conference on Visualization*, pages 147–154. Eurographics Association, 2004.

[109] Heng-Kwong Tsao and Donald L Koch. Simple shear flows of dilute gas–solid suspensions. *Journal of Fluid Mechanics*, 296:211–245, 1995.

[110] Ellák Somfai, Dániel B Nagy, Philippe Claudin, Adeline Favier, Dávid Kálmán, and Tamás Börzsönyi. Effective friction of granular flows made of non-spherical particles. In *EPJ Web of Conferences*, volume 140, page 03062. EDP Sciences, 2017.

[111] Peng Lu, ShuiXiang Li, Jian Zhao, and LingYi Meng. A computational investigation on random packings of sphere-spherocylinder mixtures. *Science China Physics, Mechanics and Astronomy*, 53(12):2284–2292, 2010.

[112] Lena M Lopatina and Jonathan V Selinger. Maier-saupe-type theory of ferroelectric nanoparticles in nematic liquid crystals. *Physical Review E*, 84(4):041703, 2011.

Appendices

A

Domain independence analysis

Height of the domain is selected based on the particle size. The system is periodic in x and y direction. A domain independence analysis is performed for spherocylindrical particles for different shear rate and volume fractions. Domain sizes used in this analysis are [0.2, 0.2, 0.096] and [0.1 0.1 0.096]. A comparison of results of one of the simulations are shown in figure A.1 in terms of shear stresses.

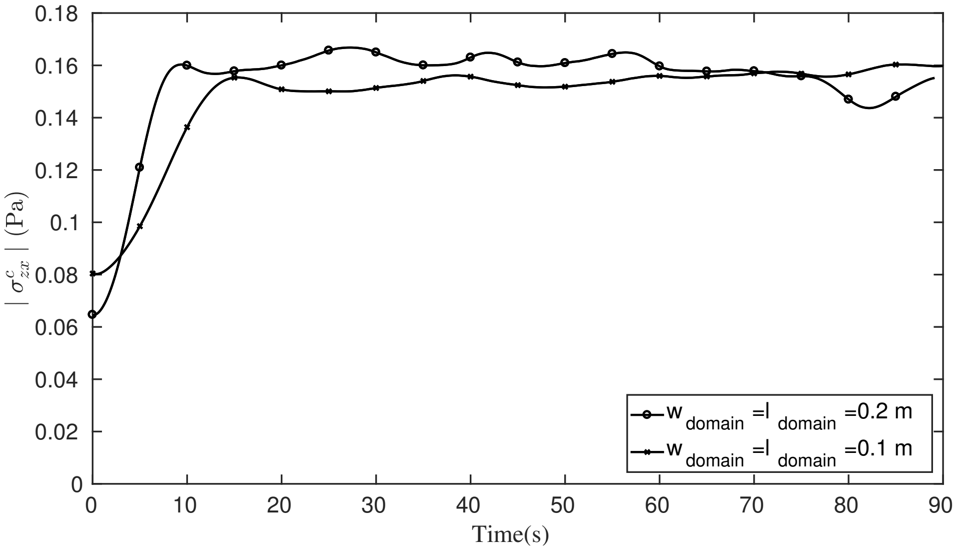

Figure A.1: Collisional shear stress for $\phi = 0.3$, $\dot{\gamma} = 15/s$.

For domain size of 0.2 m average collisional stress value is 0.1589 while for domain size of 0.1 m this value is 0.1547. Number of particles required to simulate larger domain for $\phi = 0.3$ are 14816. Which is 4 times the particles required for the smaller domain. Time to complete the simulation increase tremendously with larger domain considering more interactions are happening per unit time. It is evident from figure A.1 smaller domain produces almost similar result as larger domain thus smaller domain size is chosen to perform all the simulations.

B

Effect of fluid viscosity on shear stresses

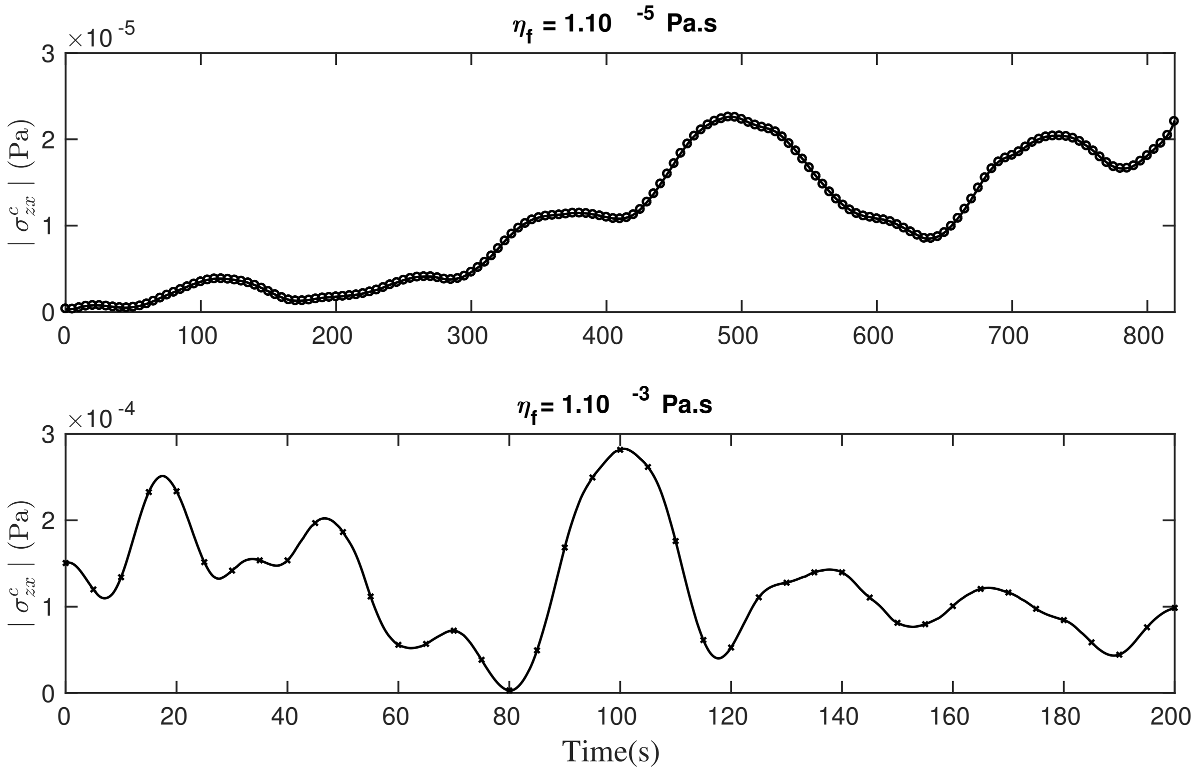

Figure B.1: Collisional shear stresses as a function of time for different fluid viscosities for $\phi = 0.1$ & $\dot{\gamma} = 2/s$

Number of simulations were performed for different volume fractions and shear rates to find out the effect of viscosity on the collisional shear stresses. Purpose of these simulations was to identify the fluid viscosity for which simulation time is not really long. Few other conclusions can also be made from these simulations results.

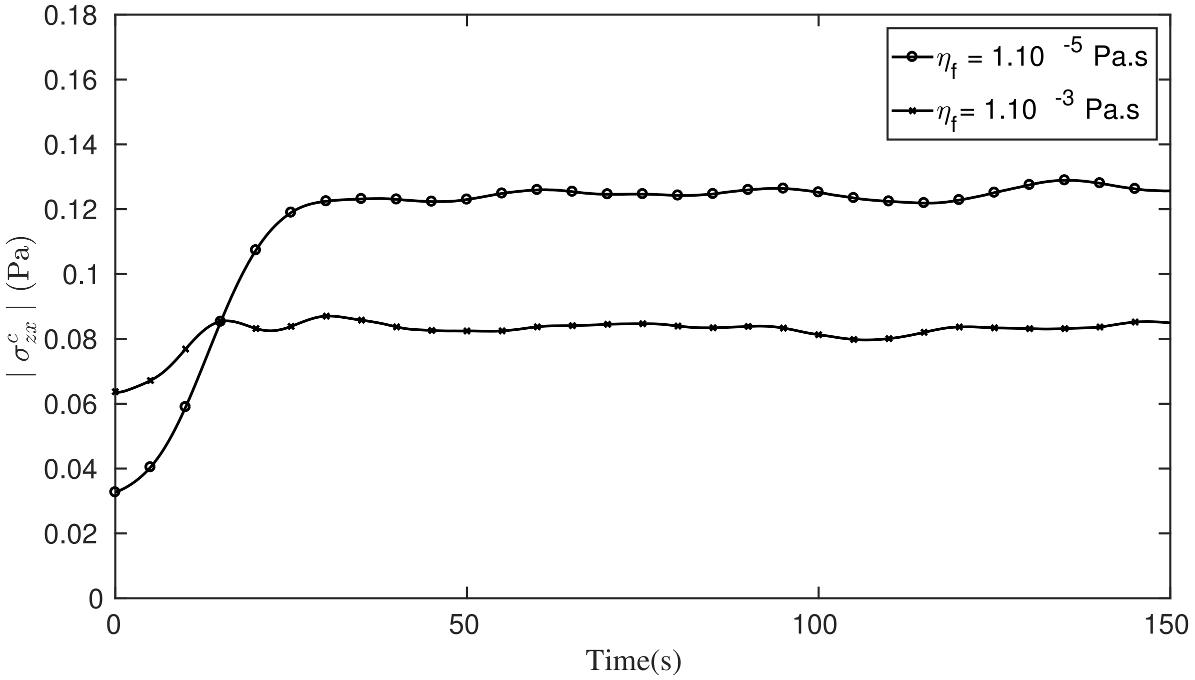

Figure B.2: Collisional shear stresses as a function of time for different fluid viscosities for $\phi = 0.4$ & $\dot{\gamma} = 4.5/s$.

Figure B.1 shows the collisional shear stresses for $\phi = 0.1$. Volume fraction plot of these simulations are shown in figure 4.9. For such a low volume fraction shear stresses differ a lot. One of the reason that both curves are not in the same plot. Also system reaches at quasi steady state after very long time in terms of shear stresses. For $\phi = 0.4$ difference between stresses is not that high as shown in figure B.2. This is exactly the same behaviour as observed by Bagnold [49]. For lower volume fraction system may be in micro-viscous regime where fluid properties have very high influence on the particle stresses. Higher volume fraction results in more particle interactions and system may be in the grain-inertia regime where particle stresses are not governed by fluid properties.

C

Time averaging

Quasi steady state time is calculated for each simulation from the domain volume fraction plot as explained in section 4.4.1. Following figures show time variation of all the measured quantities for $\phi = 0.3$ & $\dot{\gamma} = 1/s$.

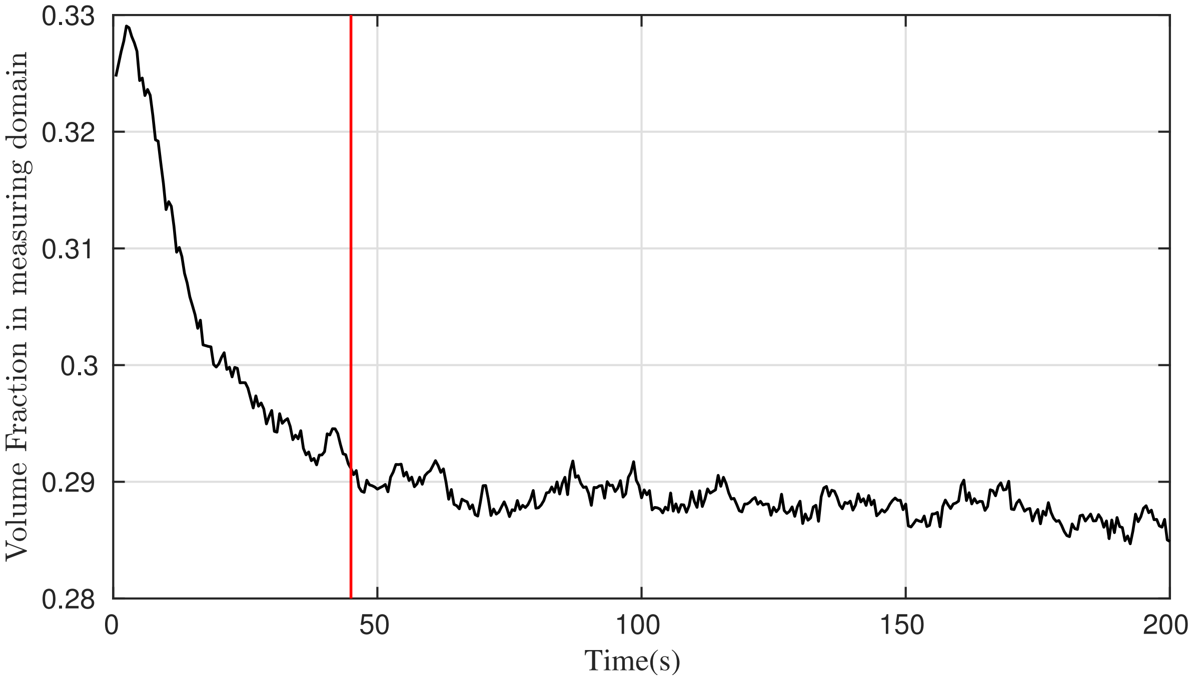

Figure C.1: Volume fraction variation in the measuring domain as a function of time.

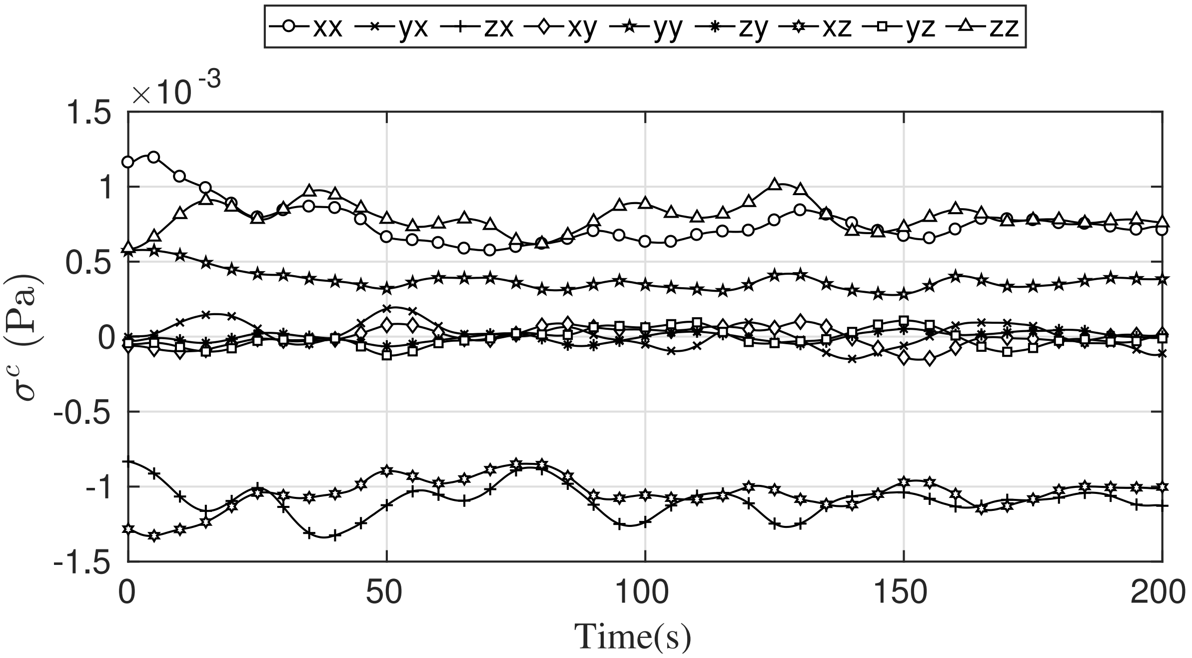

Figure C.2: Collisional Stress tensor as a function of time.

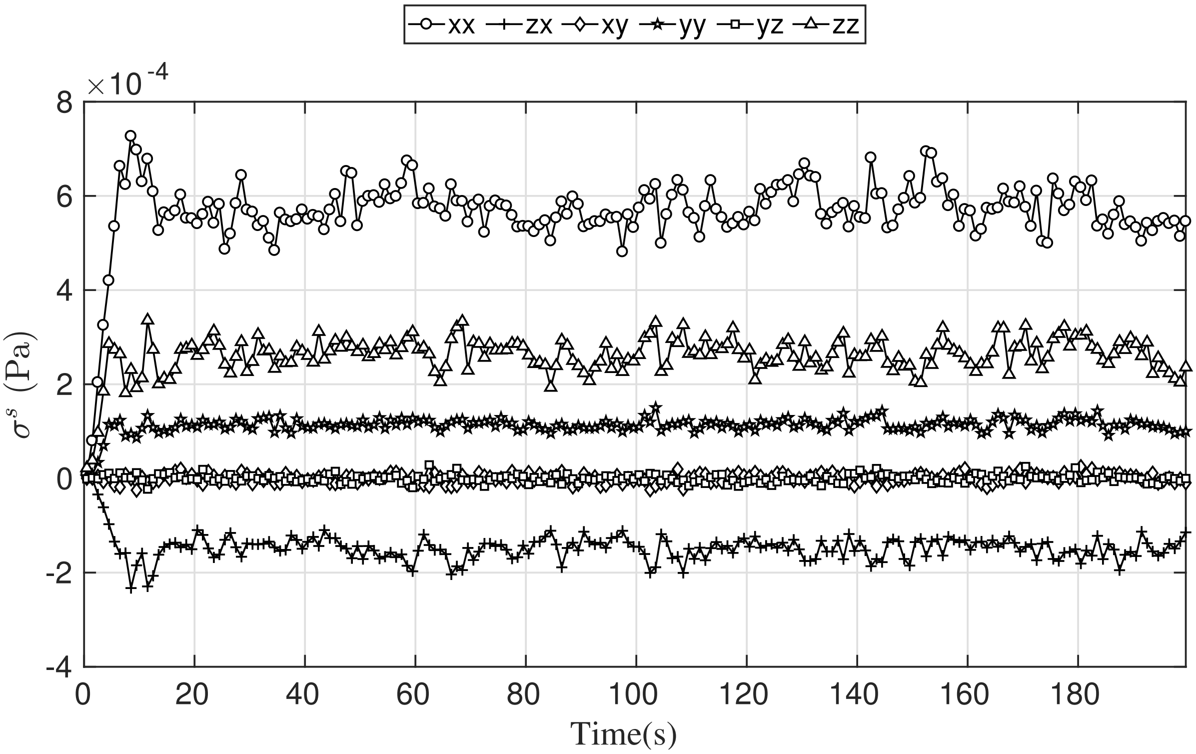

Figure C.3: Streaming Stress tensor as a function of time.

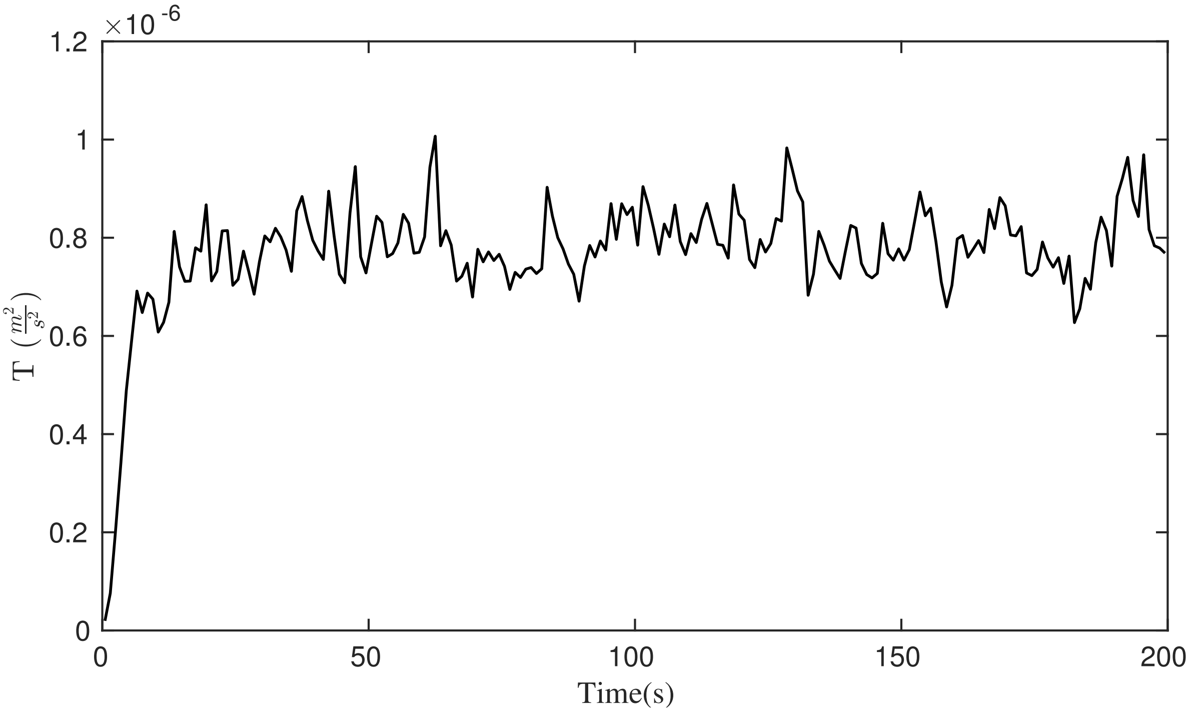

Figure C.4: Granular temperature as a function of time.

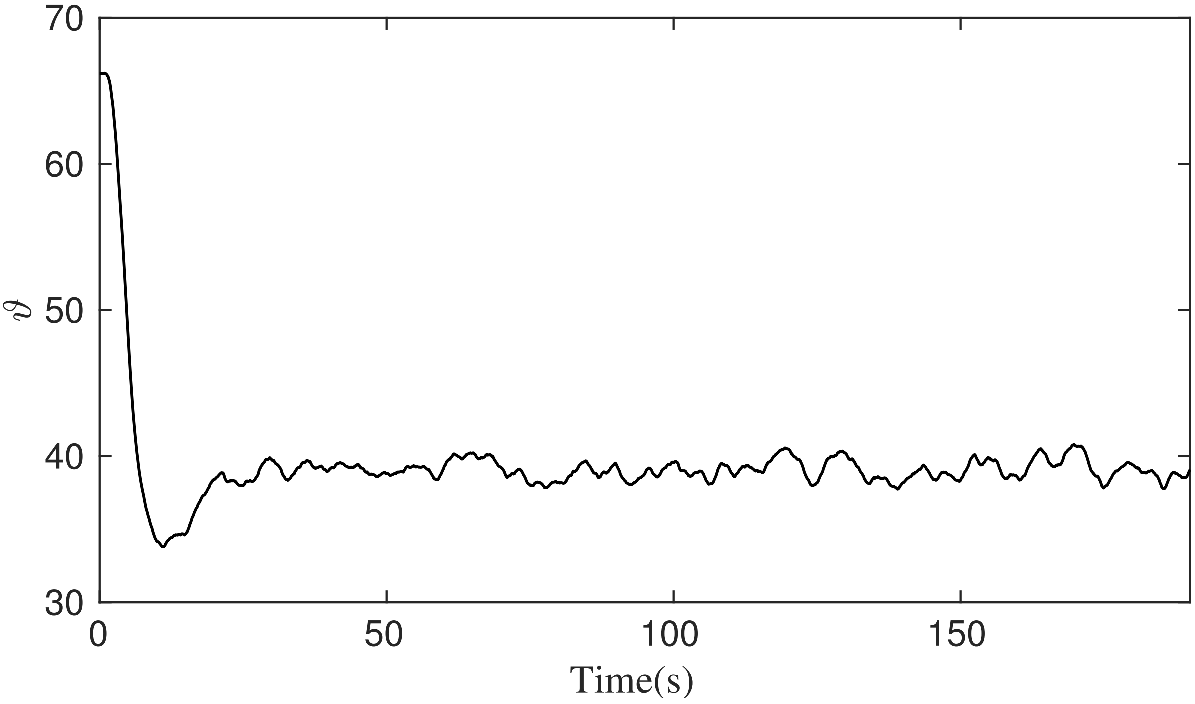

Figure C.5: Particle alignemnt with the shear flow as a function of time.

It is evident from figure C.1 that system reaches quasi steady state around 45 sec in terms of volume fraction. Rest of the measurements have already reached their constant values at this time. Averaging is performed for this data set from 45 sec to 200 sec to get an averaged value for all the measurements.

D

MATLAB code for superquadratic glyph

```
function normal_glyph(time_plot,ave_unitvec)
       % time_plot is the time array for which glyph needs to be plotted
       % average_unitvec is 3x3xlength(time_plot) 3D array obtained from the ↩
           simulation

        for file=time_plot
                ave_unitvec= average_unitvec(:,:,file)  ;
                % ave_unitvec is the unitvec obtained from simulation data
 %              average_unitvec=[0.33 0 0 ; 0 0.33 0 ;0 0 0.34]
                % Eigen Value and Eigen Vectors
                [eigvec , eigvel]=eig(ave_unitvec) ;
                eigVel=diag(eigvel) ;
                % Sorting the eigen values from maximum to minimum
                [lambda ,index]= sort(eigVel,'descend') ;
                eigenVector = [eigvec(:,index(1)) eigvec(:,index(2)) eigvec(:,↩
                    index(3))] ;
                lambdaM=diag(lambda) ;

                % Based on the equation 1 from the paper to change fig 6 to fig 7
                Normalization=eigenVector*lambdaM ;

                % Setting for the qudric Glyph
                n=50;
                [a,b] = meshgrid(1:n+1,1:n+1);
                % phi =  0 to pi
                phi_max=pi;
                phi_min=0;
                d_phi=(phi_max-phi_min)/n;
                phi = (phi_min + (a-1) * d_phi);
                % theta = 0 to 2*pi
                theta_max=2*pi;
                theta_min=0;
                d_theta=(theta_max-theta_min)/n;
                theta    = (theta_min + (b-1) * d_theta);

                % Cl ,Cp , Cs are the constants to determine quadric shape

                cL=(lambda(1)-lambda(2))/(lambda(1)+lambda(2)+lambda(3)) ;
                cP=2*(lambda(2)-lambda(3))/(lambda(1)+lambda(2)+lambda(3))  ;
                cS=3*(lambda(3))/(lambda(1)+lambda(2)+lambda(3));
```

```
          deltaF=diag([cL cP cS]);


          % Effect the sharpness of the edges , gamma = 0 gives ellipsoid

          gamma=6 ;

          % Loop to determine the glyph points

          for k=1:length(theta)
                  for l=1:length(theta)
                      if cL>=cP
                          alpha=(1-cP)^gamma ;
                          beta=(1-cL)^gamma ;
                          x= (((abs(cos(theta(k,l))).^alpha).*sign(cos(↩
                              theta(k,l)))  .* ((abs(sin(phi(k,l))).^beta).*↩
                              sign(sin(phi(k,l))))));
                          y=(((abs(sin(theta(k,l))).^alpha).*sign(sin(theta↩
                              (k,l)))  .* ((abs(sin(phi(k,l))).^beta).*sign(↩
                              sin(phi(k,l))))));
                          z=(((abs(cos(phi(k,l))).^beta).*sign(cos(phi(k,l)↩
                              ))) );
                      else
                          beta=(1-cP)^gamma ;
                          alpha=(1-cL)^gamma ;

                          z=((abs(cos(theta(k,l))).^alpha).*sign(cos(theta(↩
                              k,l)))  .* ((abs(sin(phi(k,l))).^beta).*sign(↩
                              sin(phi(k,l)))));
                          y=-((((abs(sin(theta(k,l))).^alpha).*sign(sin(↩
                              theta(k,l)))  .* ((abs(sin(phi(k,l))).^beta).*↩
                              sign(sin(phi(k,l)))))));
                          x=(((abs(cos(phi(k,l))).^beta).*sign(cos(phi(k,l)↩
                              )))) ;

                      end
                  X(k,l) = ( Normalization(1,:)*[x;y;z]) ;
                  Y(k,l)= ( Normalization(2,:)*[x;y;z]) ;
                  Z(k,l) = ( Normalization(3,:)*[x;y;z]) ;
          end
    end

    % Figure setting

    f_1=figure(8) ;
    f_1.Name = 'Rod Glyph';
    f_1.Units= 'inches';
    f_1.Position=[0 0 23 16];
    f_1.PaperPositionMode='auto';
    f_1.Color='w';

    s=surf(X,Y,Z);
    s.XData = X;    % replace surface x values
    s.YData = Y;    % replace surface y values
    s.ZData = Z;    % replace surface z values
    set(gca,'GridLineStyle','none')
    set(gca,'XTick',[]);
    set(gca,'YTick',[]);
    set(gca,'ZTick',[]);
    set(gca,'XColor','w','YColor','w','ZColor','w');
    axis equal
```

```

          xlim([-1 1]);
          ylim([-1 1]);
          zlim([-1 1]);
          xl=xlim();
          yl=ylim();
          zl=zlim();
          title([’time = ’, num2str(file/100),’s’],’interpreter’,’latex’,’↩
              FontSize’,25,’FontName’,’Tahoma’) ;
          shading interp
          colormap([0 0 0])
          lighting flat
          light(’Position’,[0 1 0],’Style’,’infinite’,’Color’,’w’);
          light(’Position’,[0 -1 0],’Style’,’infinite’,’Color’,’w’);
          light(’Position’,[-1 0 0],’Style’,’infinite’,’Color’,’w’);
          light(’Position’,[0 0 -1],’Style’,’infinite’,’Color’,’w’);
          light(’Position’,[0 0 1],’Style’,’infinite’,’Color’,’w’);
          light(’Position’,[1 0 0],’Style’,’infinite’,’Color’,’w’);
          view(24,22)
          pause(0.5)


        end
end
```

E

Collisional stress tensor symmetry

In relation to the figure 5.5 all components of collisional stress tensor are shown in the following figures for $\dot{\gamma} = 0.5/s$. For $\phi = 0.1$ & 0.2 stress tensor is asymmetric.

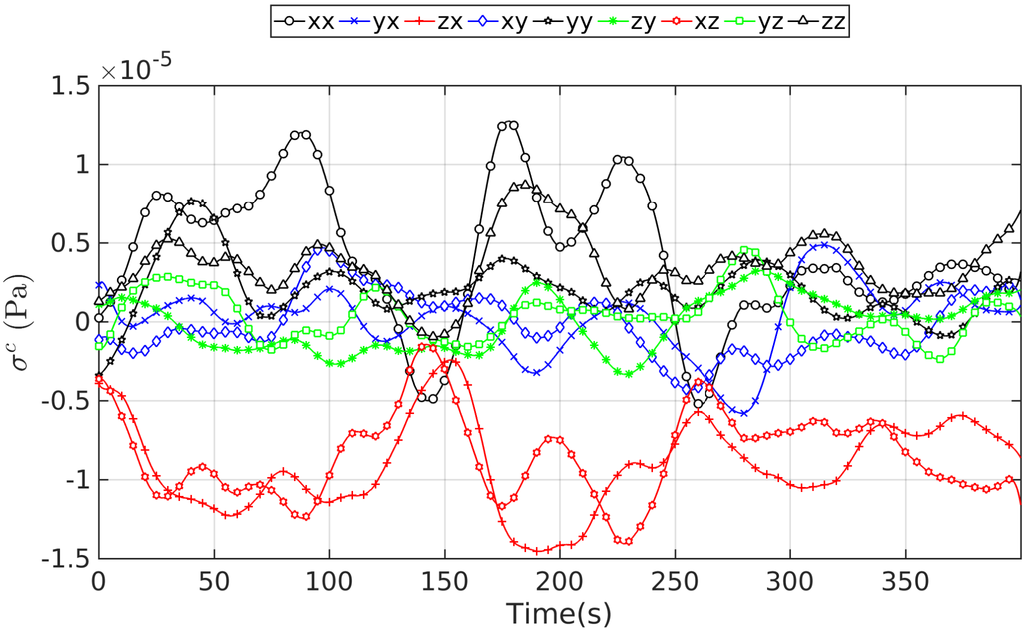

Figure E.1: Collisional stress tensor for $\phi = 0.1$.

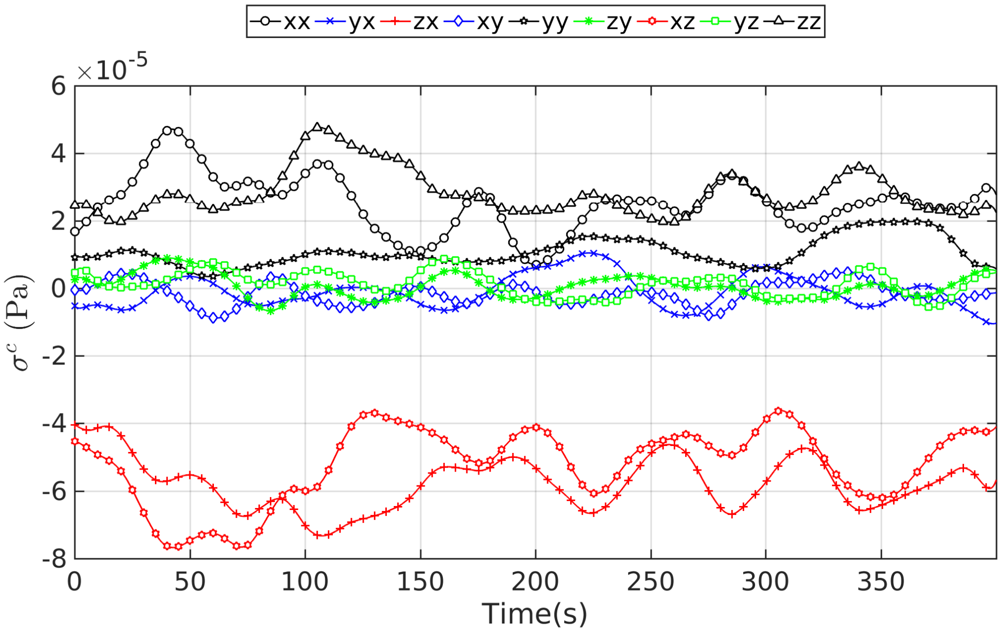

Figure E.2: Collisional stress tensor for $\phi = 0.2$.

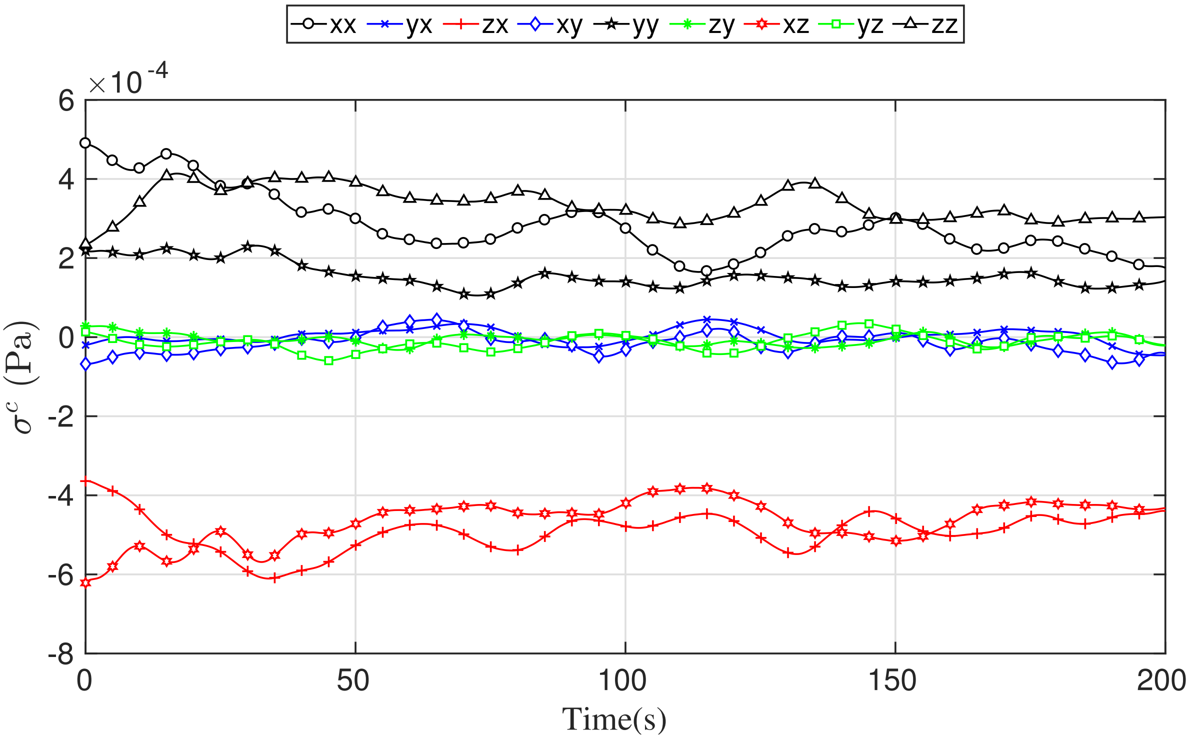

Figure E.3: Collisional stress tensor for $\phi = 0.3$.

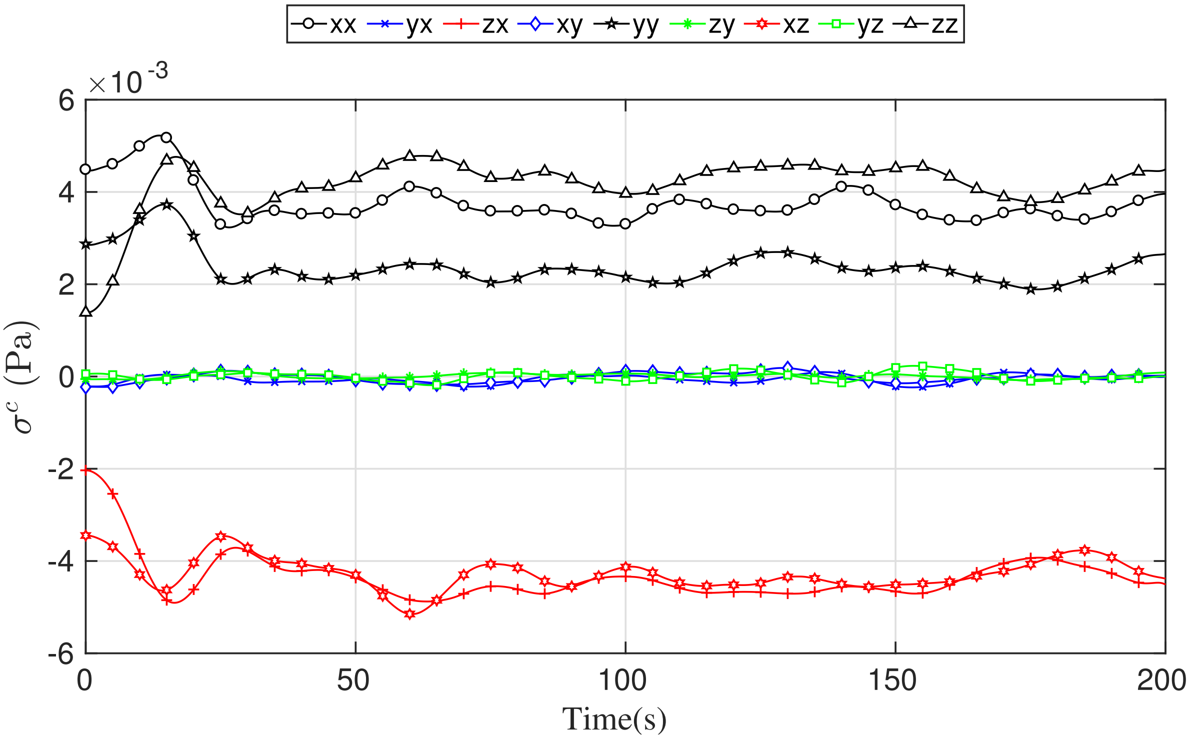

Figure E.4: Collisional stress tensor for $\phi = 0.4$.

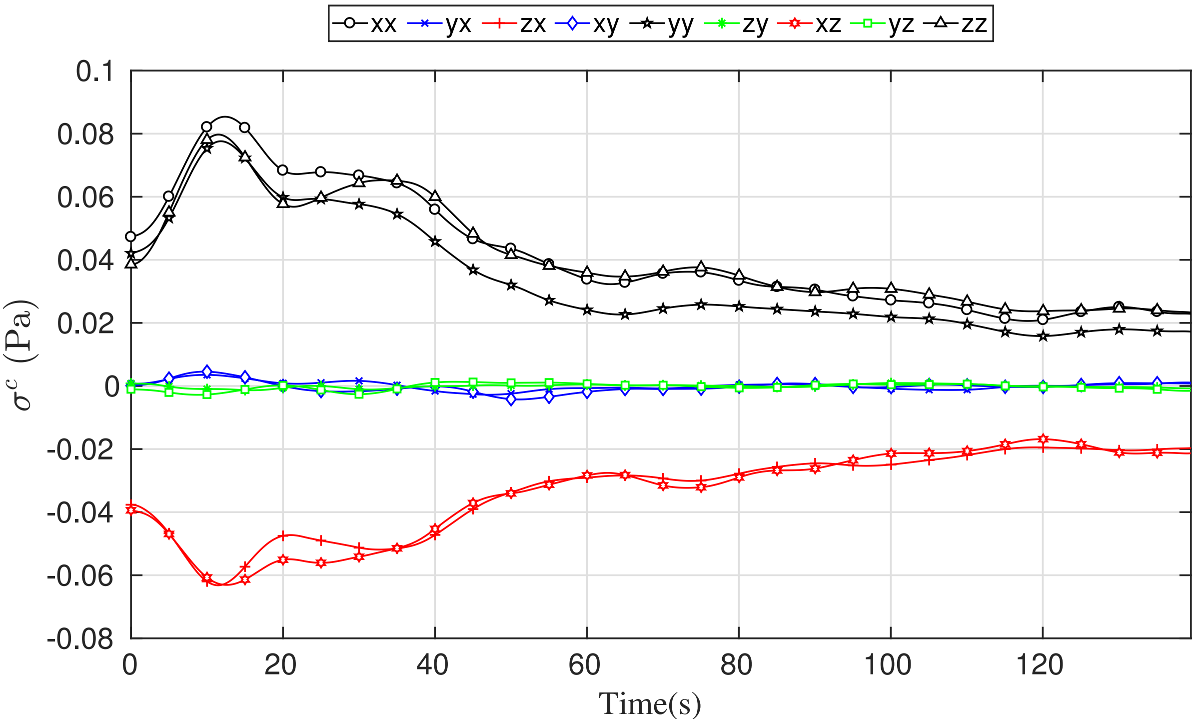

Figure E.5: Collisional stress tensor for $\phi = 0.5$.

F

Data Fitting

In order to determine the consistency$C$ and flow index(m) raw simulation data is fitted to equation 5.5. Figure F.1 shows Nonlinear least Square fitting.

F.1. Nonlinear least square fitting

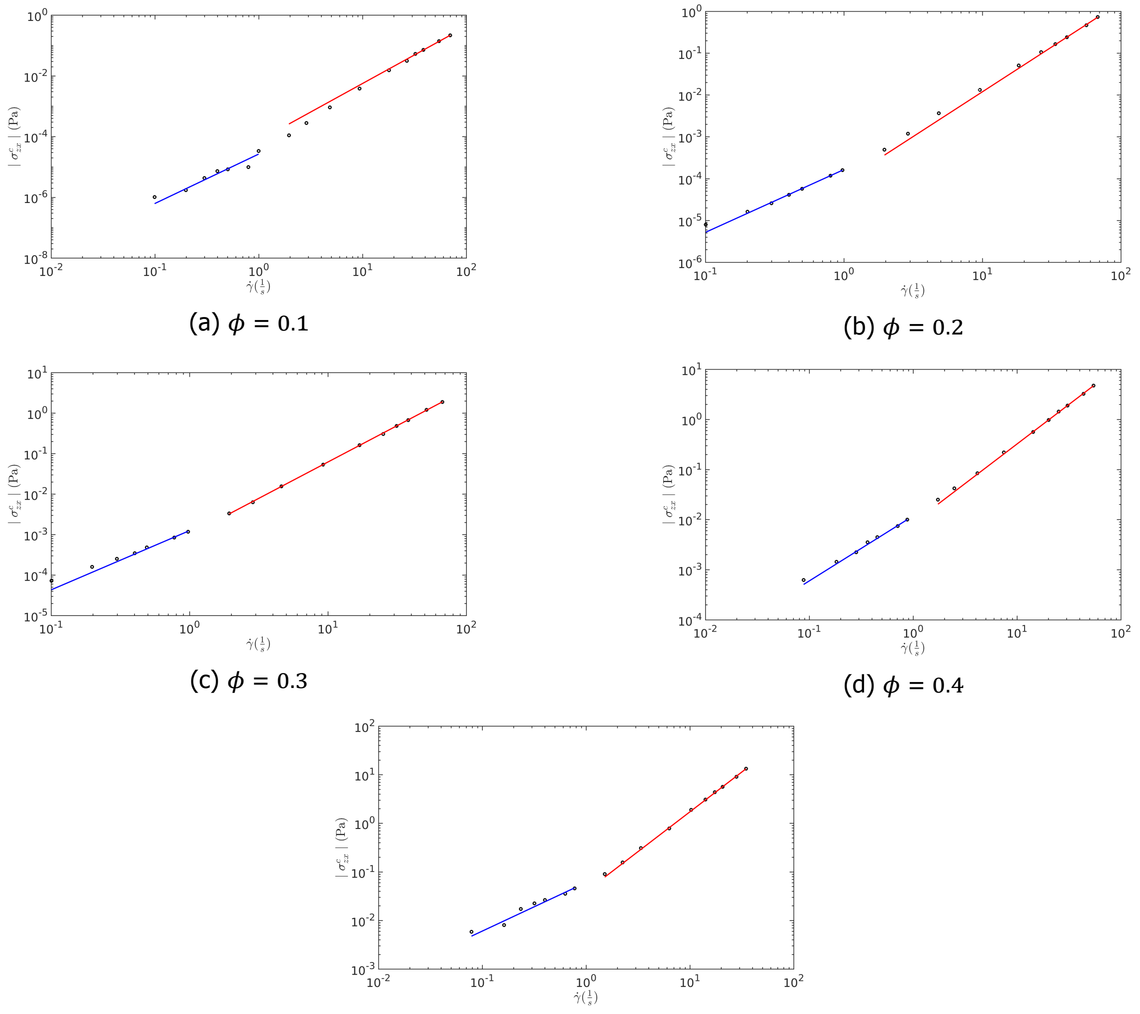

(a) $\phi = 0.1$

(b) $\phi = 0.2$

(c) $\phi = 0.3$

(d) $\phi = 0.4$

(e) $\phi = 0.5$

Figure F.1: Non Least square fitting for collisional stresses, o represent raw simulation data,— represent fitted curve for $\dot{\gamma} < 1$,— represent fitted curve for $\dot{\gamma} > 1$.

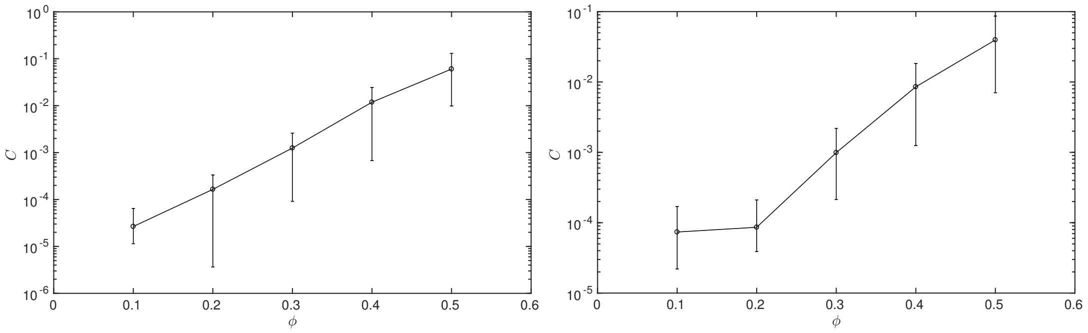

(a) $\dot{\gamma} < 1$

(b) $\dot{\gamma} > 1$

Figure F.2: Relative consistency as a function of volume fractions

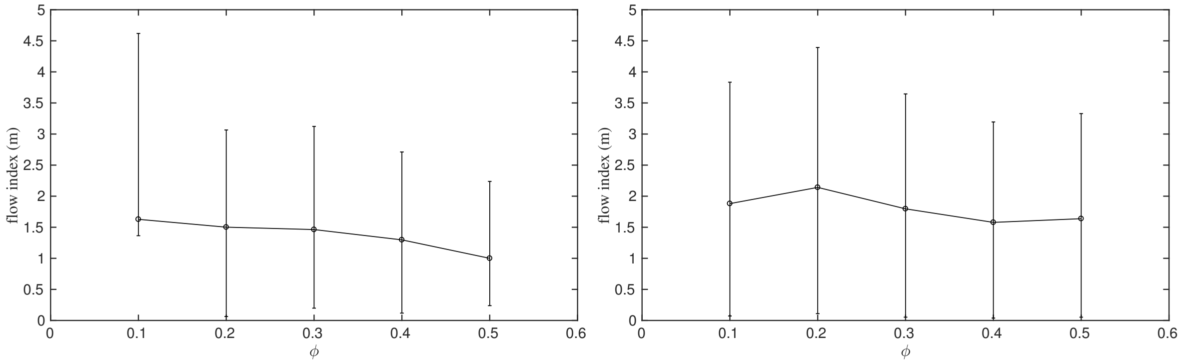

(a) $\dot{\gamma} < 1$ (b) $\dot{\gamma} > 1$

Figure F.3: Flow index as a function of volume fractions

F.2. Krieger and Dougherty model

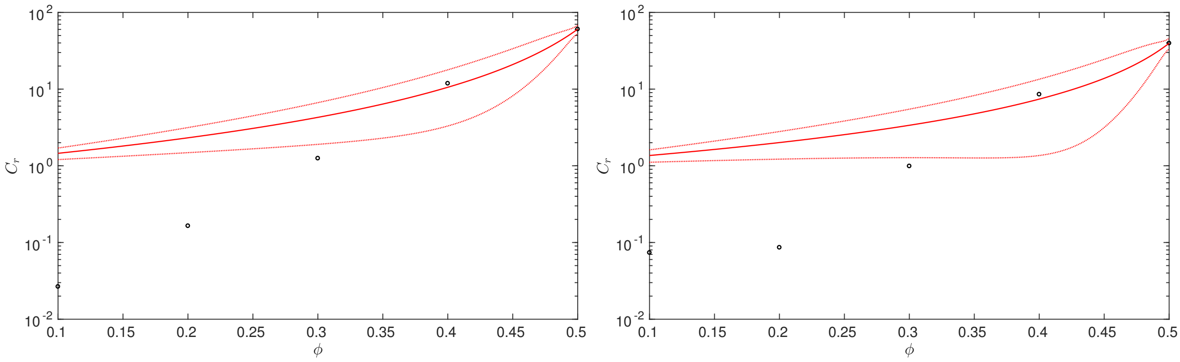

(a) $\dot{\gamma} < 1$ (b) $\dot{\gamma} > 1$

Figure F.4: Relative Consistency as a function of volume fraction,o represent relative consistency values,— represent fitted curve,– – – represent prediction bounds

F.3. Broughton-Geoffrey model

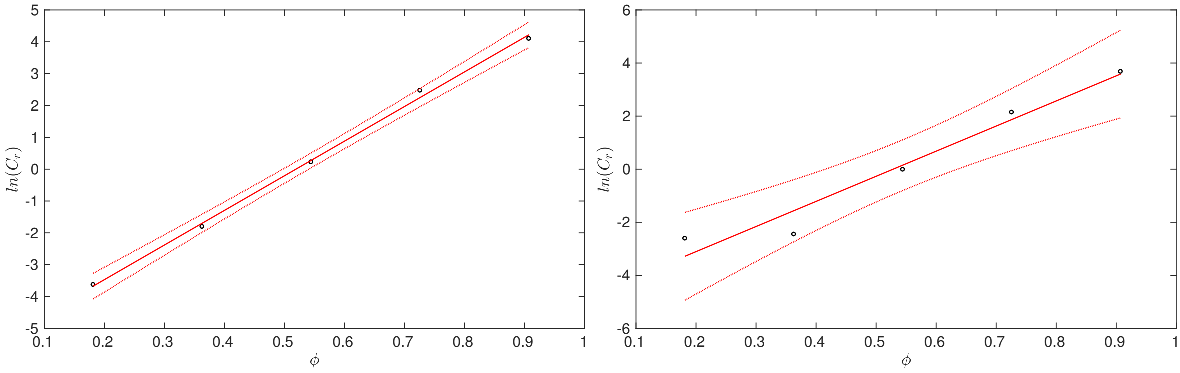

(a) $\dot{\gamma} < 1$ (b) $\dot{\gamma} > 1$

Figure F.5: Relative Consistency as a function of volume fraction, o represent relative consistency values,— represent fitted curve,– – – represent prediction bounds